[UCI]I804:24011-200000266504

February 2018

Doctor's Degree Thesis

Implementation of Beamforming Antenna for UWB Radar using Butler Matrix

Graduate School of Chosun University

Department of Information and Communication Engineering

Sun-Woong Kim

Implementation of Beamforming Antenna for UWB Radar using Butler Matrix

버틀러 매트릭스를 이용한
UWB 레이더용 빔 포밍 안테나 구현

February 23, 2018

Graduate School of Chosun University

Department of Information and Communication Engineering

Sun-Woong Kim

Implementation of Beamforming Antenna for UWB Radar using Butler Matrix

Advisor: Prof. Dong-You Choi

This thesis is submitted to the Graduate School of Chosun University in partial fulfillment of the requirements for the Doctor's degree engineering.

October 2017

Graduate School of Chosun University

Department of Information and Communication Engineering

Sun-Woong Kim

This is to certify that the Doctor's thesis of Sun-Woong Kim

has been approved by the examining committee for the thesis requirement for the Doctor's degree in engineering

Committee Chairperson
Prof. Seung-Jo Han ______________________ **(Sign)**

Committee Member
Prof. Jae-Young Pyun ______________________ **(Sign)**

Committee Member
Dr. Il-Jung Kim ______________________ **(Sign)**

Committee Member
Prof. Sun-Kuk Noh ______________________ **(Sign)**

Committee Member
Prof. Dong-You Choi ______________________ **(Sign)**

December 2017

Graduate School of Chosun University

Table of Contents

List of Tables

List of Figures

Abstract

Implementation of Beamforming Antenna for UWB Radar using Butler Matrix

Sun Woong Kim
Advisor: Prof. Dong-You Choi, Ph.D.
Depart. of Info. and Comm. Engg.,
Graduate School of Chosun University

The single antenna of conventional ultra-wideband radars has difficulty tracking objects over a wide range because of the relatively narrow beamwidth. This thesis is to prposed a beamforming antenna that can track objects over a wide range by electronically controlling the beam of the antenna.

The proposed beamforming antenna was fabricated by connecting a 1 × 4 linear array antenna and a 4 × 4 Butler matrix. The 4 × 4 Butler matrix was fabricated in a laminated substrate using two TRF-45 substrates, which have a relative permittivity of 4.5, loss tangent of 0.0035, and thickness of 0.61 ㎜; the overall size is 70.65 × 62.6 × 1.22 ㎣. The phase difference results of the 4 × 4 Butler matrix had an error of ± 10° at -45°, 135°, −135°, and 45°. Therefore, the fabricated 4 × 4 Butler matrix has the characteristic of constant phase difference, and the output phase was fed into the input ports of the 1 × 4 array antenna. The distance between each antenna in the fabricated 1 × 4 array is 30 ㎜. The proposed tapered-slot antenna was fabricated on a Taconic TLY

substrate, which has a relative permittivity of 2.2, loss tangent of 0.0009, and thickness of 1.52 ㎜; the overall size is 140 × 90 × 1.52 ㎣. The impedance bandwidth of the antenna was achieved in the wide bandwidth of 4.32 ㎓ by satisfying -10 dB S_{11} and VSWR ≤ 2 in the 1.45 ~ 5.78 ㎓ band. Furthermore, the fabricated antenna has directional radiation patterns, which was found to be a suitable characteristic for location tracking in a certain direction.

Therefore, the signal generated by the 4 × 4 Butler matrix was fed into the input ports of the 1 × 4 array antenna, and the fabricated beamforming antenna has four beamforming angles. The beamforming range of the fabricated antenna has maximum values of 115°, 90°, and 80° in the 3 ㎓, 4 ㎓, and 5 ㎓band, respectively.

요 약

버틀러 매트릭스를 이용한 UWB 레이더용 빔 포밍 안테나 구현

김 선 웅

지도교수: 최 동 유

조선대학교 대학원 정보통신공학과

기존의 UWB 레이더의 단일 안테나는 비교적 좁은 빔폭으로 인해 넓은 공간에 위치한 사물을 추적하는데 어려움이 있었다. 본 논문에서는 안테나의 빔을 전자적으로 제어함으로써 넓은 공간에 위치한 사물의 정보를 추적할 수 있는 빔 포밍 안테나를 제안하였다.

제안한 빔 포밍 안테나는 선형으로 배열된 1 × 4 배열 안테나와 4 × 4 버틀러 매트릭스를 연결하여 제작하였다. 4 × 4 버틀러 매트릭스에 사용된 기판은 유전율 4.5, 손실 탄젠트 0.0035, 두께 0.61 ㎜를 갖는 2개의 TRF-45 기판에 적층으로 제작되었으며, 전체 크기는 70.65 × 62.6 × 1.22 ㎣이다. 4 × 4 버틀러 매트릭스의 위상차 측정 결과는 각각 -45°, 135°, -135°, 45°에서 ±10°의 오차가 관찰되었다. 따라서, 제작된 4 × 4 버틀러 매트릭스는 각 포트마다 적절한 위상차의 특성을 갖으며, 출력된 위상은 선형으로 배열된 1 × 4 배열안테나의 입력포트에 인가된다.

제작된 1 × 4 배열 안테나의 이격 거리는 30 ㎜이다. 테이퍼드 슬롯 안테나는 유전율 2.2, 손실 탄젠트 0.0009, 두께 1.52 ㎜를 갖는 Taconic TLY 기판에 제작되었으며, 전체 크기는 140 × 90 × 1.52 ㎣이다. 안테나의 임피던스 대역폭은 1.46 ~ 5.78 ㎓ 대역에서 -10 dB S_{11} 및 VSWR≤2를 만족하여 4.32 ㎓의 넓은 대역폭을 형성하였다. 또한, 안테나의 방사패턴은 특정 방향에 대한 감도가 높아지는 지향성의 방사패턴이 관찰되었다.

이를 통해, 4 × 4 버틀러 매트릭스에 출력된 급전신호는 1 × 4 배열 안테나의 입력 포트에 인가되며, 4개의 빔 조향 각을 갖는다. 제작된 빔 포밍 안테나의 빔 조향 범위는 3 ㎓ 대역에서 115°, 4 ㎓ 대역에서 최대 90°, 5 ㎓ 대역에서 최대 80°를 갖는다.

Ⅰ Introduction

Recently, the range of location tracking targets has been reduced to small sizes such as vehicles, persons, small articles goods at large objects such as aircraft, buildings, marine vessels, etc[1]. The location tracking fields in outdoor environments use precise global navigation satellite systems, such as the global positioning system of the United States and the global orbiting navigation satellite system of Russia. However, there are no obvious solutions to the problems of indoor location tracking technologies[2].

Ultra-wideband (UWB) radar technology is expected to improve conventional indoor monitoring systems by enabling precise location tracking in the ㎝ range within a room at low cost and reduced power consumption[3]. In particular, the U.S. Federal Communications Commission (FCC) has been using systems such as near-field communication, location tracking, penetrating radar, and distance measurement systems by revoking civil use regulations in February 2002[4～7].

The antenna in an UWB radar system must have a wide bandwidth to transmit and receive the impulse signals of ㎱ units in a specific direction, as well as high gain and directional radiation patterns to track the location of objects. Conventional UWB antennas have been studied for various antennas, such as the Vivaldi antenna[8][9], patch antenna[10], Yagi-type antenna[11][12], and tapered-slot antenna[13][14]. These antennas have difficulty tracking objects that are located over a wide range owing to the relatively narrow beamwidth of approximately. In order to solve this problem, thesis proposed a beamforming antenna that can track the information on objects over a wide range.

The proposed beamforming antenna was fabricated by combining beamforming networks that generate a constant phase and a tapered-slot antenna array. Conventional beamforming networks include the Butler matrix[15], Blass matrix[16], Nolen matrix[17], Rotman lens[18], etc.; these beamforming networks have different phase delays between the input and output ports. The beamforming antenna structure is shown in Fig. 1-1.

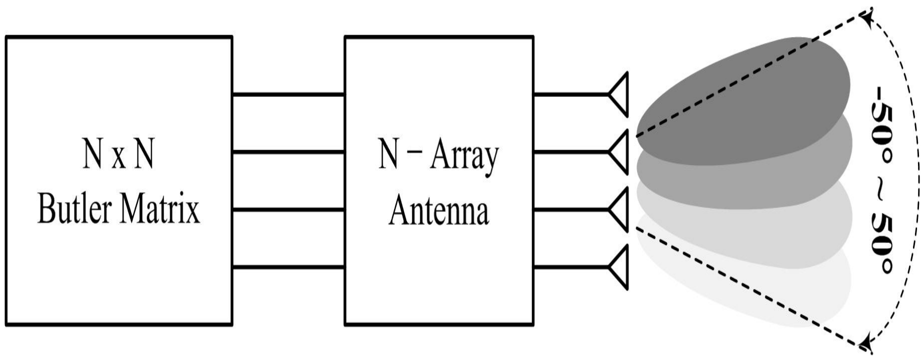

Fig. 1-1. System structure of N × N beamforming antenna

As shown in Fig. 1-1, the structure of the beamforming antenna requires a beamforming network (N × N Butler matrix) capable of giving different constant phase and for the N-array antenna to radiate toward the desired direction. The proposed technology was implemented using the Butler matrix, which is easy to manufacture and is low cost. The Butler matrix consists of 3 dB/90° slot-directional hybrid couplers and 45° phase shifters. When the input and output ports of the Butler matrix increase, the controlled phase beam increases, but the circuit size is large, and the design becomes complicated. Therefore, this thesis proposes a 4 × 4 Butler matrix which has four input and four output ports, where the output phase is fed into the input ports of the linear array antenna (1 × 4 array antenna). The beams of the proposed beamforming antenna can be controlled in four directions, and can provide solutions to track the location of objects placed from approximately -50° to +50°.

This thesis is organized as follows. In chapter 1, the proposed technology and the necessity and purpose of the UWB beamforming antenna are described. In chapter 2, the understanding of UWB radar systems and operating characteristics of the UWB antenna are examined, and the design theory of the Butler matrix for the phase array is described. In chapter 3 describes the simulation of tapered-slot antenna (TSA) and 4 × 4 Butler matrix using HFSS (Ansys Co.), a commercial electromagnetic simulator to implement the UWB beamforming antenna. In chapter 4, the UWB beamforming antenna is fabricated based on the simulation results, and the antenna performance is measured and verified using various measuring equipment. Finally, chapter 5 draws conclusion regarding the proposed beamforming antenna.

Ⅱ Theoretical Background

2.1 UWB Radar System

2.1.1 Overview of UWB Technology

UWB is a wireless communications technology developed by the U.S. department of defense for military purposes, which has a bandwidth of several ㎓ for short-range wireless communications, and it define as ultra wide band system with 100 Mbps to 1 Gbps of high speed transmission rate. In order to distinguish it from existing systems, the UWB signal is defined as radio transmission technology with an occupied bandwidth of more than 1.5 ㎓ or over 25% of the center frequency.

The UWB permissive specification specified by the U.S. FCC satisfies the noise intensity of -41.3 ㏈m/㎒ and bandwidth of more than 20% factional bandwidth in frequency band of 3.1 to 10.6 ㎓[19]. The definitions of other band and the UWB band shown in Fig. 2-1.

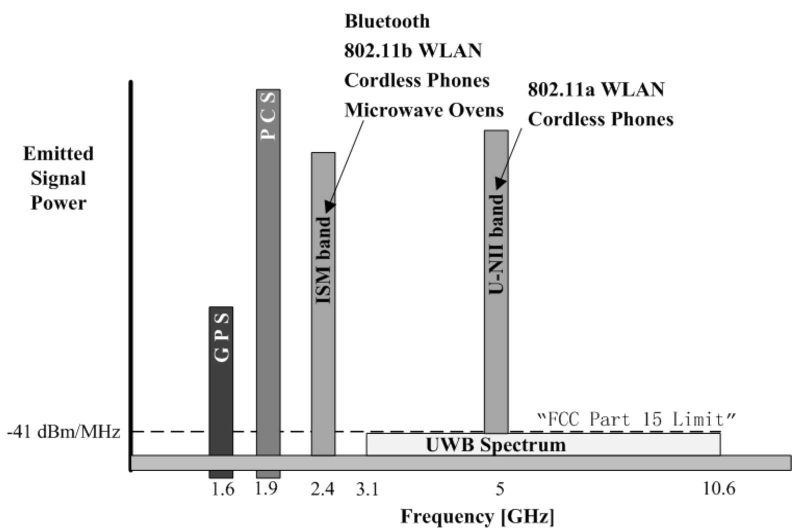

Fig. 2-1. Definition of UWB bandwidth

Applications of UWB radar systems include ground-penetrating radar systems, through-wall radar systems, medical imaging radar systems, search and rescue radar systems, and nondestructive radar systems[7]. The bandwidth for the signal spectrum of the UWB radar system is shown in Fig. 2-2.

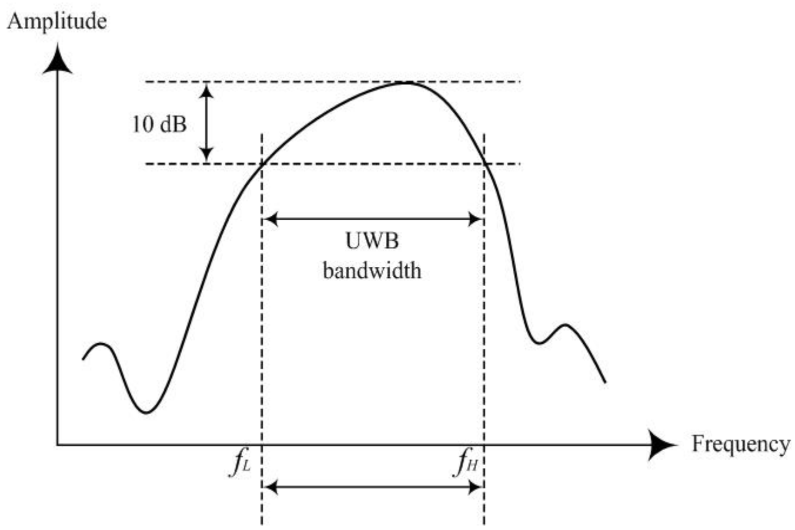

Fig. 2-2. Bandwidth definition for the signal spectrum of UWB radar system

The fractional bandwidth of the UWB radar system is given by

$$FBW = \frac{f_H - f_L}{\left(\frac{f_H + f_L}{2}\right)} \times 100\%, \tag{2-1}$$

where f_H and f_L are the upper and lower frequency, respectively, based on -10 dB point-of-signal spectrum.

2.1.2 Configuration of UWB Radar System

Recently, UWB radar systems have been studied for high-resolution radar systems. UWB radar technology radiates an impulse signal of ns units and analyzes information on the target through signals reflected by object. The distance measurement process of the UWB radar system is shown in Fig. 2-3.

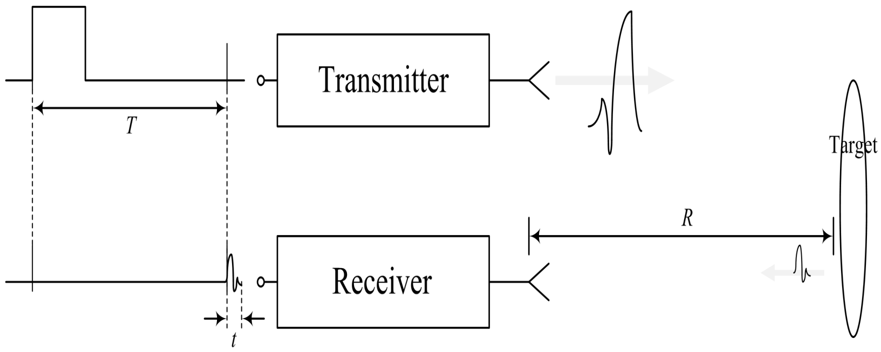

Fig. 2-3. Distance measurement method of UWB radar system

The basic UWB radar system consists of a transmitter and receiver. The distance measurement of the object is given by

$$R = \frac{ct}{2}, \tag{2-2}$$

where R is the distance of the object, c is the velocity of light, and t is the time difference between the received signal and transmitted signal[20][21].

The UWB radar system includes transmission and receiving antennas, radio frequency (RF) filter, power amplifier (PA), and low-noise amplifier (LNA). The signal processing structure of the UWB radar system is shown in Fig. 2-4.

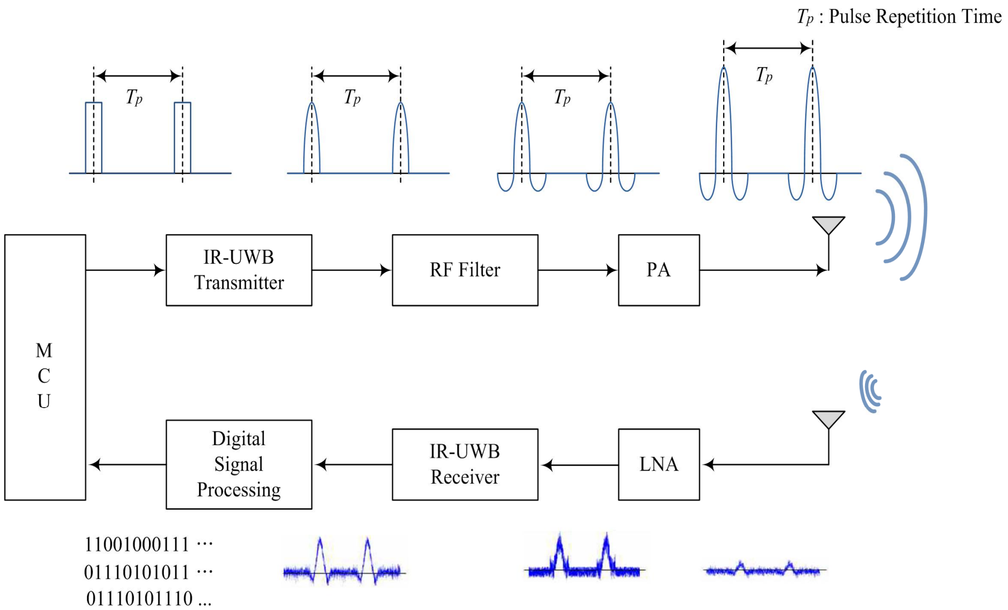

Fig. 2-4. Structure and signal processing process of UWB radar system

The pulse signal is generated by the microcontroller unit (MCU) which is converted by the UWB transmitter. The RF filter passes only the necessary signal, and the PA amplifies the intensity of the signal and transmits it to the antenna. The signal that radiates into free space passes through the receiving antenna, and the signal is amplified at the LNA stage. Finally, digital signal processing converts the received analog signal into a digital signal[22].

2.2 Investigation of UWB Antenna

2.2.1 Types of Wideband Antennas

Wideband antennas are used in various applications such as fractal antennas[23][24], bow-tie antennas[25], spiral antennas[26], and log-periodic antennas[27][28]. The fractional bandwidth of the wideband antenna is over 25%. The wideband antenna can be implemented to increase bandwidth by more than 100% when constructing an antenna with a complementary structure and self-similar structure[29][30].

As shown in Fig. 2-5, the log-periodic antenna has a constant period between several antenna elements, and it achieves a wide frequency band by forming multiresonance through different lengths of elements[31].

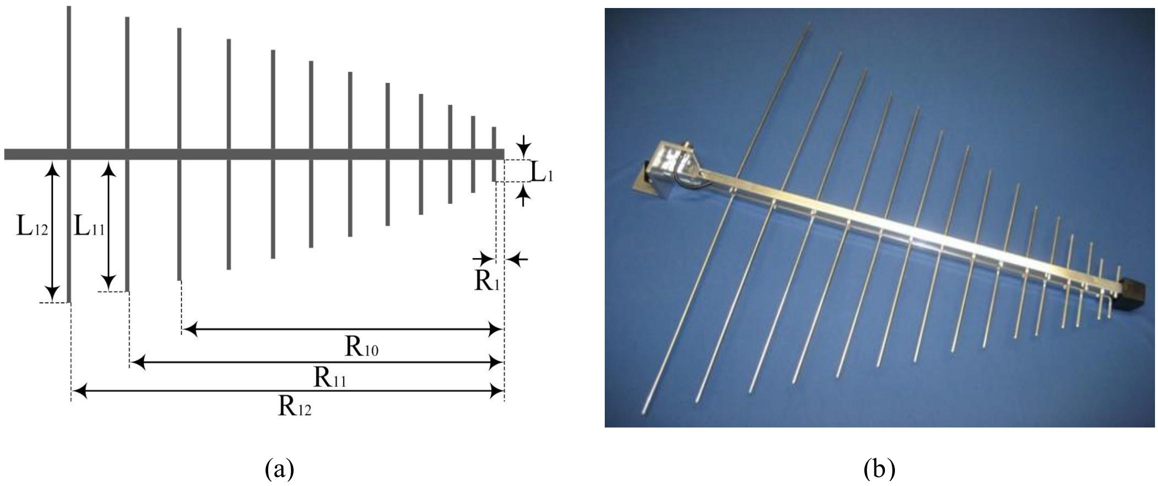

Fig. 2-5. Examples of log-periodic antenna, (a) Structure of log-periodic antenna[31], (b) Actual log-periodic antenna[32]

The fractal structure is similar to the structure that is repeatedly created in the natural world, and the overall structure is characterized by similar self-similarity. The fractal structure is shown Fig. 2-6.

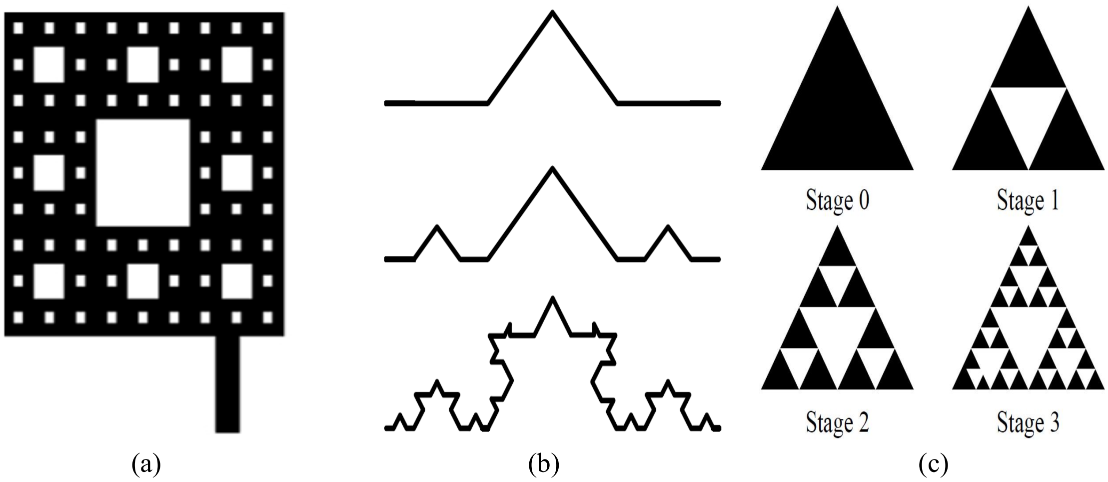

Fig. 2-6. Examples of various fractal structures, (a) Sierpinski carpet structure, (b) Kuch curve structure, (c) Sierpinski gasket structure

The fractal antenna has multiple resonance owing to its repeating similar structures, which include a Sierpinski carpet structure, Koch curve structure, and Sierpinski gasket structure[33].

The bow-tie antenna has a radiation pattern similar to the linear dipole antenna. The structure of the bow-tie antenna is shown in Fig. 2-7.

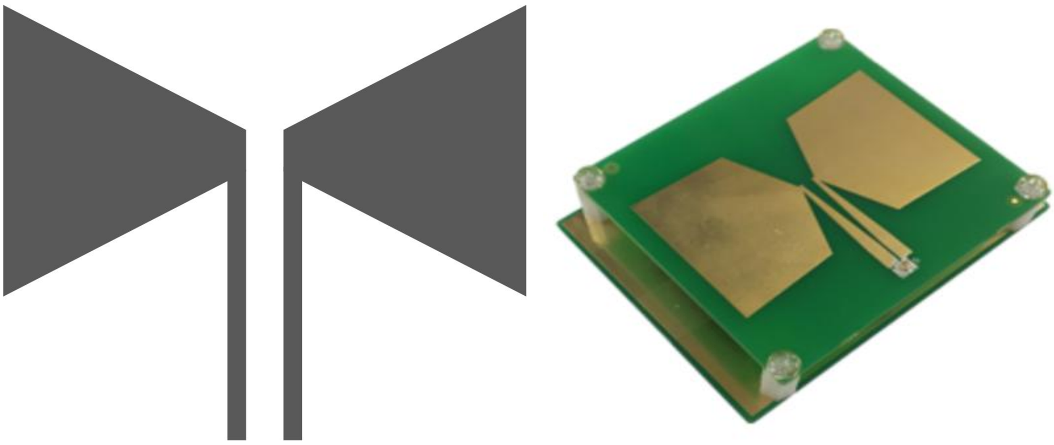

(a) (b)

Fig. 2-7. Examples of bow-tie antenna, (a) Structure of bow-tie antenna, (b) Actual bow-tie antenna[34]

The bow-tie antenna is used in wide-band systems because of its wide operating frequency[31].

2.2.2 Types of Travelling Wave Antennas

Travelling wave antennas include TSAs, dielectric rod antennas, and horn antennas. These antennas provide the good characteristics for the UWB system and there is less distortion between transmitted and received pulses in the propagation path.

The horn antenna is commonly used for measuring patterns or ground-penetrating radar applications, and has a wide bandwidth of 50～180%.

As shown in Fig. 2-8, the structure of the horn antenna is either a pyramid or conical.

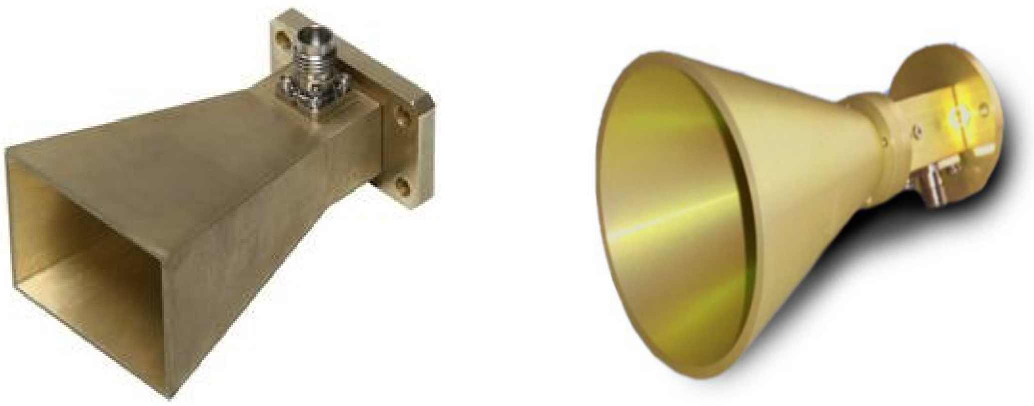

(a) (b)

Fig. 2-8. Examples of horn antennas, (a) Structure of pyramid horn antenna[35], (b) Structure of conical horn antenna[36]

The TSA is mainly used in UWB radar systems. A typical TSA antenna is fabricated by etching the tapered shape on the substrate with a copper plate[37].

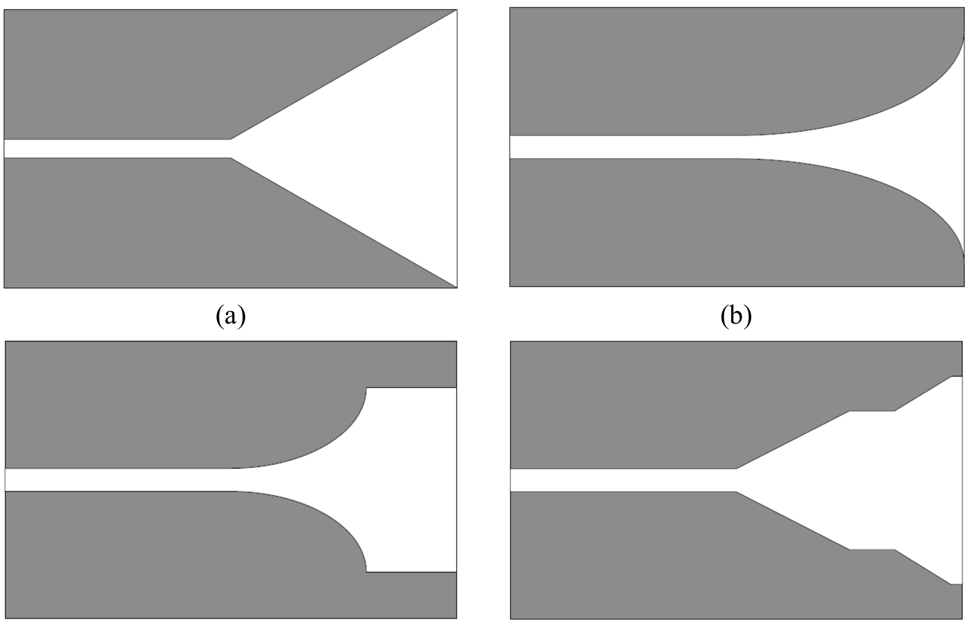

(a) (b) (c) (d)

Fig. 2-9. Examples of TSAs, (a) LTSA, (b) Vivaldi, (c) CWSA, (d) BLTSA

As shown in Fig. 2-9, examples of TSAs include a linear TSA (LTSA), constant-width slot antenna (CWSA), broken linearly TSA (BLTSA), and Vivaldi-type antenna. These TSAs have a wide bandwidth of 125～170%[37].

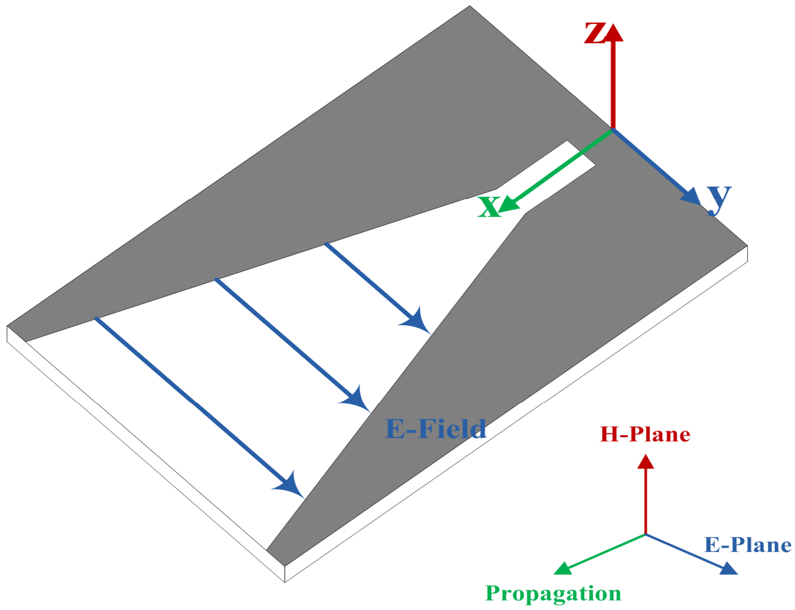

Fig. 2-10. Electromagnetic wave configuration of the tapered-slot antenna

In the TSA, a surface wave propagates along the antenna substrate and shows a travelling wave characteristic of end-fire[38]. As shown in Fig. 2-10, the electronic field moves along the tapered aperture structure and radiates from the substrate edge. Therefore, the E-plane of the TSA is radiated horizontally (x-y) parallel to the substrate while the H-plane is radiated vertically[39].

The 3D radiation simulation results of the proposed TSA are shown in Fig. 2-11.

As shown in Fig. 2-11, the main beam of the proposed TSA is directed toward the z direction, the E-plane is radiated horizontally (y-z), and the H-plane is radiated vertically (x-z).

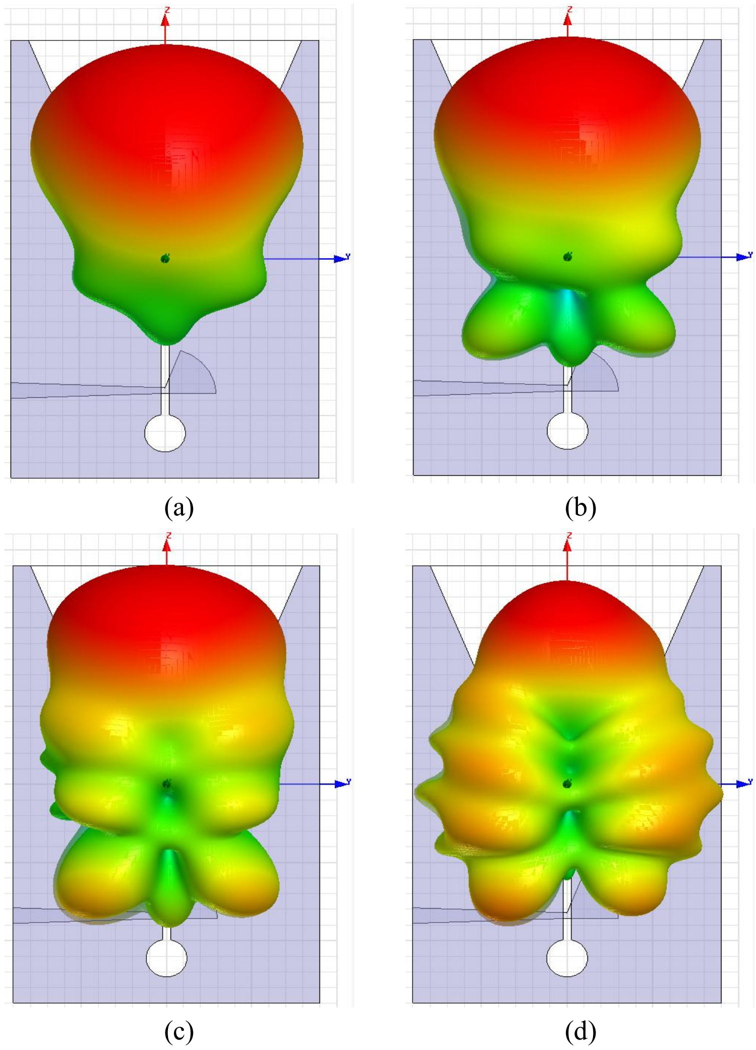

(a) (b) (c) (d)

Fig. 2-11. 3D radiation pattern simulation results of the proposed antenna, (a) 2 ㎓ band, (b) 3 ㎓ band, (c) 4 ㎓ band, (d) 5 ㎓ band

2.3 Antenna Analysis Parameters

2.3.1 Impedance Bandwidth

The reflection coefficient Γ of a single scattering parameter S_{11} is the amount of signal reflection by impedance mismatch that occurs between the source and antenna during the operation of an antenna in one port. The input voltage standing wave ratio (VSWR) and return loss are given by[40]

$$VSWR = \frac{1 + |\Gamma|}{1 - |\Gamma|}, \tag{2-3}$$

$$RL\,[dB] = 20\log|\Gamma|. \tag{2-4}$$

The optimal $VSWR$ is $|\Gamma|$ = 0, or $VSWR$ = 1. This means that all the power is transmitted to the antenna and there is no reflection. The defined impedance bandwidth of the antenna is shown in Fig. 2-12.

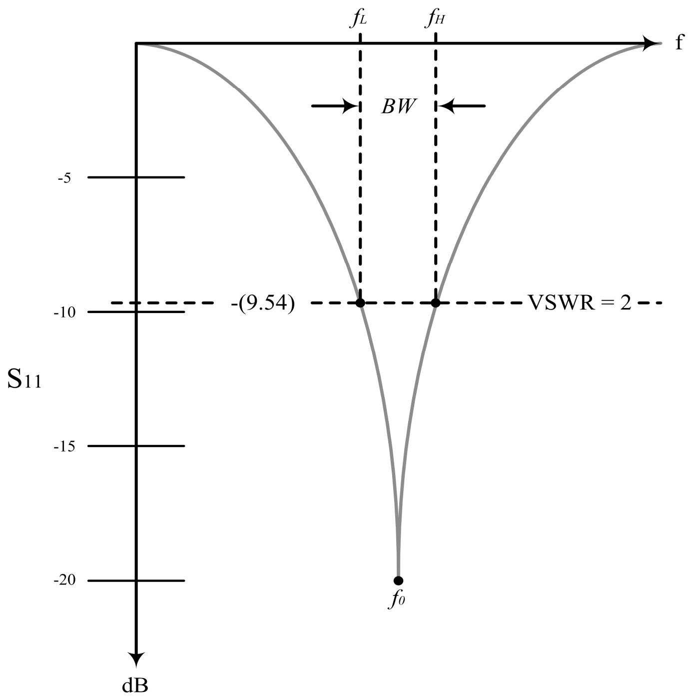

Fig. 2-12. Impedance bandwidth define of the antenna[41][42]

Therefore, the impedance bandwidth of the antenna is defined a VSWR $\leq$ 2, and its point reflects approximately 11% of input power[41].

2.3.2 Half-Power Beamwidth and Sidelobe Level

The half-power beamwidth (HPBW) is defined as the point in which the magnitude of the maximum radiation drops to half or 3 dB below, while the sidelobes are power radiation peaks in addition to the main lobe. The sidelobe levels (SLLs) are normally given as the number of decibels below the main-lobe peak. The HPBW and SLL are shown in Fig. 2-13[41].

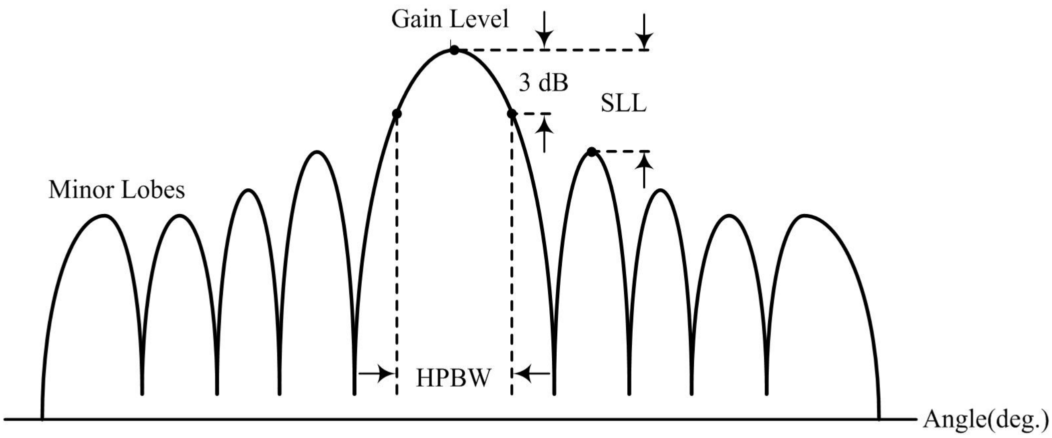

Fig. 2-13. Antenna pattern characteristics[41][42]

2.4 Review of the Beamforming Antenna

2.4.1 Theory of the Phased Array Antenna

The beamforming antenna theory for steering the main beam in the desired direction is achieved by adjusting the parameters of each antenna. The main beam is affected by four factors.

The first factor is the arrangement of array antennas, consisting of the linear structure, circular structure, planar structure, and spherical structure. The linear and circular structures are a one-dimensional array structure, while the planar and spherical structures are two-dimensional and three-dimensional array structures, respectively. The second factor is the distance between each antenna. The appropriate distance between antennas is an important parameter that can reduce grating lobes. The third factor is the phase of the signal input into each antenna. The phase of the input signal can determine the direction of the main beam that is radiated into the space. The fourth factor is the pattern of the single antenna. The pattern of the single antenna is the fundamental factor that determines the beam direction by combining the array antenna[43]. These factors can steer the main beam of the beamforming antenna in the desired direction.

As shown in Fig. 2-14, the basic one-dimensional linear array antenna should be the same size as the array antenna, and the phase should constantly increase in order.

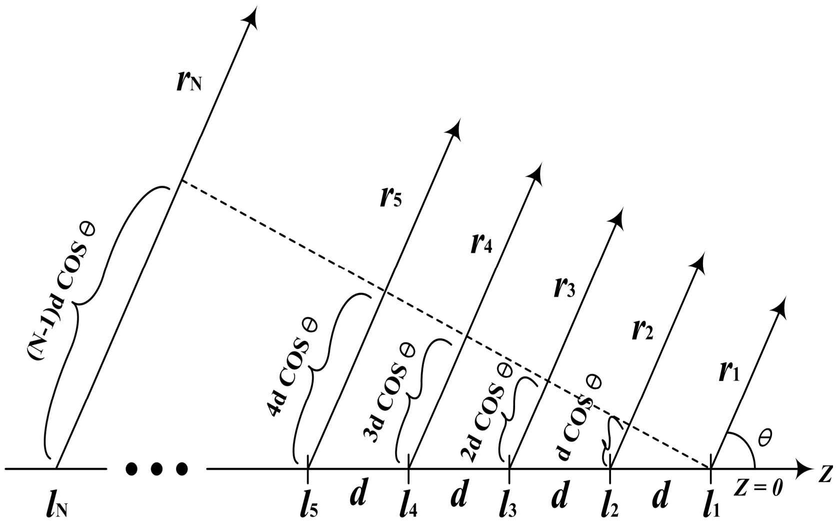

Fig. 2-14. Configuration of linear array

The radiated field of the one-dimensional linear array antenna is given by

$$E_{total} = I_1 f_1(\theta,\phi)\rho_1 \frac{e^{-j(k_0 r_1 - \phi_1)}}{4\pi r_1} + I_2 f_2(\theta,\phi)\rho_2 \frac{e^{-j(k_0 r_2 - \phi_2)}}{4\pi r_2} + \cdot\cdot\cdot \qquad (2\text{-}5)$$
$$+ I_i f_i(\theta,\phi)\rho_i \frac{e^{-j(k_0 r_i - \phi_i)}}{4\pi r_i} + \cdot\cdot\cdot,$$

where I_i, ρ_i, and ϕ_i are the size, polarization, and phase of the i-th single antenna, respectively, $f(\theta, \phi)$ is the radiation pattern, k_o is the propagation constant ($2\pi/\lambda_0$), and r_i is the distance from the i-th element to an arbitrary point in space.

Typically, the polarization of each antenna has co-polarization (i.e., $\rho i \approx \rho = 1$). The array has N antennas with uniform spacing d, and is oriented along the z-axis with phase progression ϕ. The first antenna is placed at the origin with distance r_i The phase is approximated using the following equation:

$$\begin{aligned} r_1 &\cong r \\ r_2 &\cong r + d\cos\theta \\ &\vdots \\ r_N &\cong r + (N-1)d\cos\theta. \end{aligned} \tag{2-6}$$

Therefore, the total field is given by

$$E_{total} = f(\theta, \phi)\frac{e^{-jk_0 r}}{4\pi r}\sum_{i=1}^{N} I_i e^{-j(i-1)(k_0 d\cos\theta - \phi)}. \tag{2-7}$$

The total field of the array antenna is composed of each antenna pattern $f(\theta, \phi)(e^{-jk_o r}/4\pi r)$ and the array factor, which is known as pattern multiplication. Thus, the radiation pattern of the linear array antenna is given by the array factor equation

$$AF = 1 + e^{-j(k_0 d\cos\theta - \phi)} + e^{-j2(k_0 d\cos\theta - \phi)} + \cdots + e^{-j(N-1)(k_0 d\cos\theta - \phi)}, \tag{2-8}$$

or the following equation

$$AF = \sum_{n=0}^{N-1} e^{-jn\psi}, \tag{2-9}$$

where $\psi = k_0 d\cos(\theta - \phi)$.

The parameter ϕ is the progressive phase shift of the array antenna, which means that there is a phase difference between array antennas. The beamforming process of the linear phased array antenna is shown in Fig. 2-15.

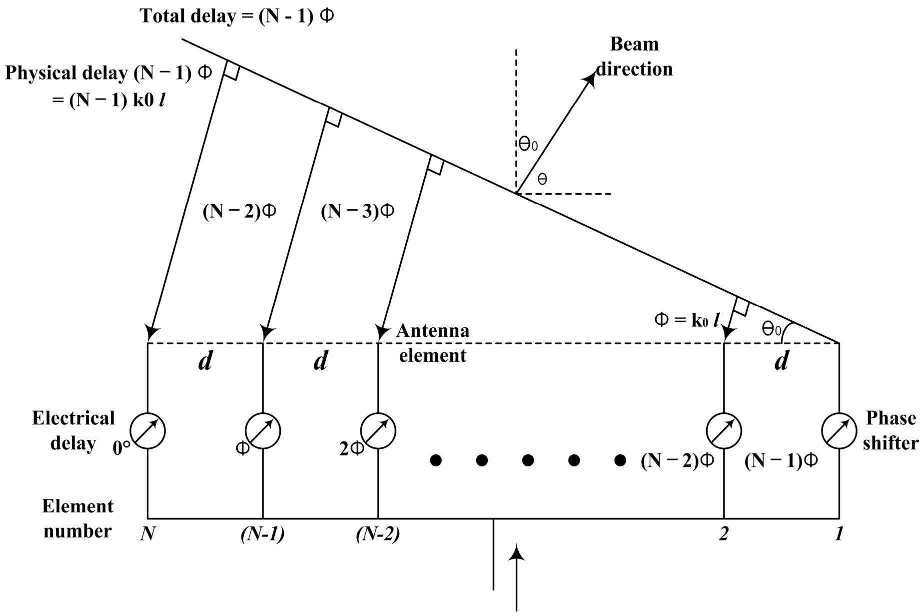

Fig. 2-15. Beamforming process of the linear phased array antenna with N antennas

As shown in Fig. 2-15, the main beam of the linear phased array antenna is oriented in the direction Θ_0, and the scanning angle is given by equations (2-10) and (2-11).

$$\phi = k_0 d \sin(\theta_0), \tag{2-10}$$

$$\theta_0 = \sin^{-1}\left(\frac{\phi}{k_0 d}\right). \tag{2-11}$$

The change of progressive phase shift, ϕ result in the change of scanning angle Θ_0, which is the basic concept used in the phased array antenna[44].

2.4.2 Structure of the Butler Matrix

The phase input into the beamforming antenna is supplied by the Butler matrix, which has N input and N output. Typically, N input/output ports in the Butler matrix are configured at values of 4, 8, and 16; as N increases, the direction of the beam increases, but the design is complicated. Hence the thesis proposed the 4 × 4 Butler matrix which has four inputs and four outputs. The configuration of the proposed 4 × 4 Butler matrix is shown in Fig. 2-16[43].

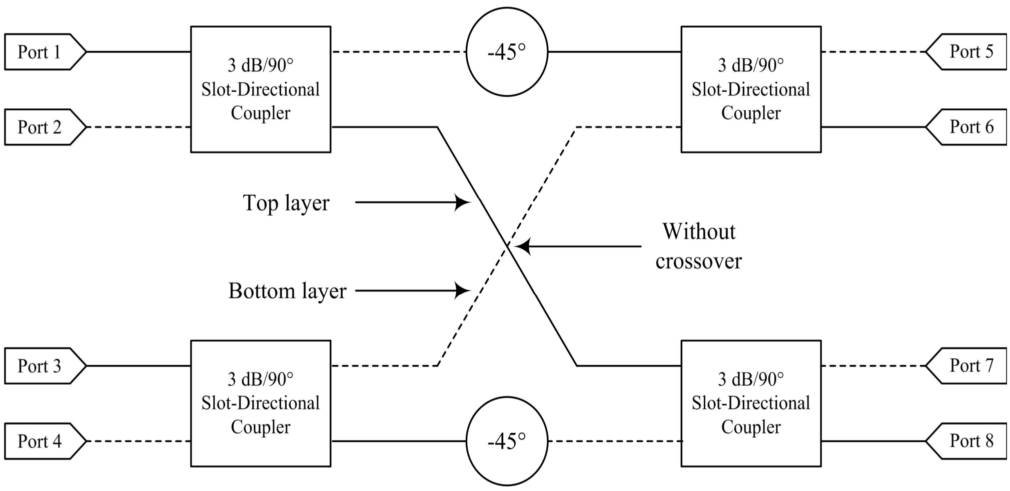

Fig. 2-16. Configuration of the 4 × 4 Butler matrix[43]

The existing Butler matrix was designed on a single-layer substrate, but this increased the size of the circuit owing to the two crossovers. To address this problem, the proposed 4 × 4 Butler matrix was fabricated by integrating the two substrates, which removed the crossover. The proposed 4 × 4 Butler matrix consists of four 3 dB/90° hybrid couplers and two −45° phase shifters. The slot-coupled characteristics of the two-layer substrates improved the impedance bandwidth and circuit size.

The ideal output (output ports 5～8) for input port 1 of the proposed 4 × 4 Butler matrix is shown in Fig. 2-17.

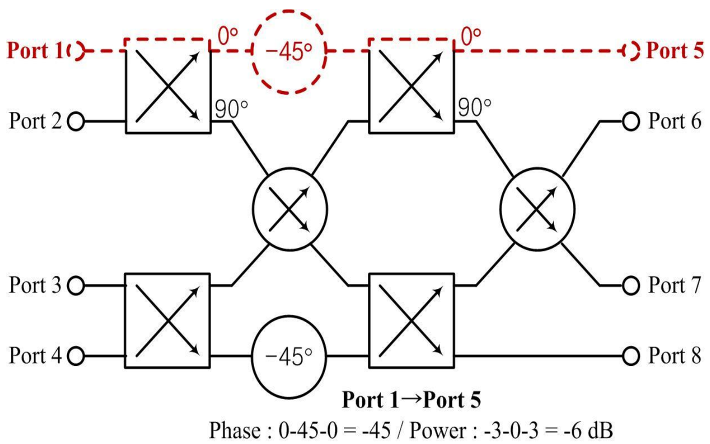

(a)

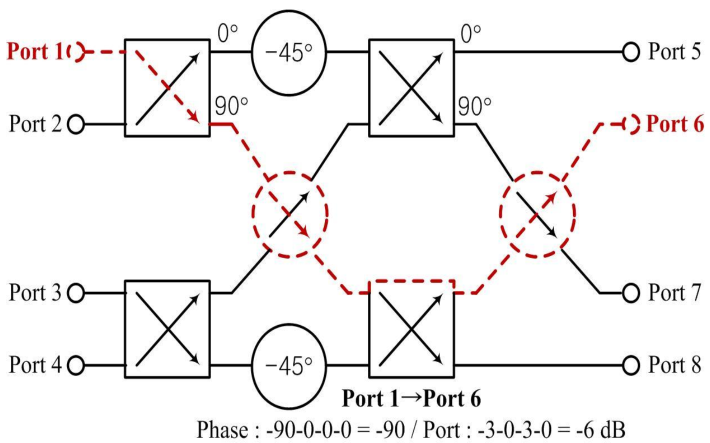

(b)

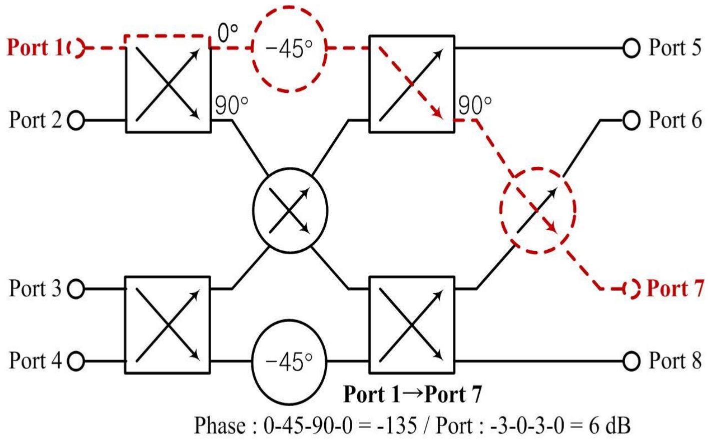

(c)

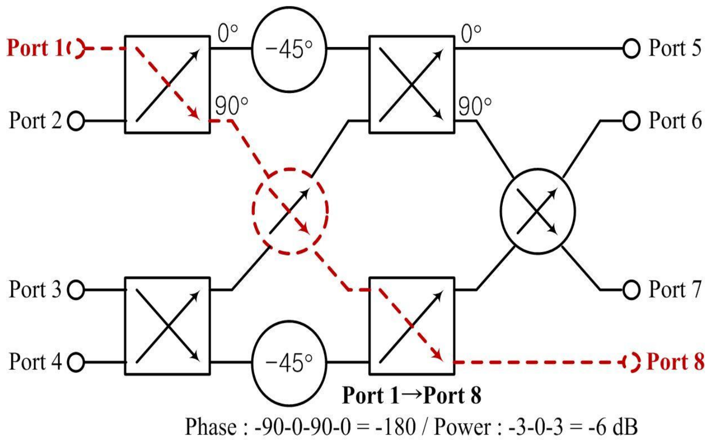

(d)

Fig. 2-17. Phase and power output results of output ports (5～8) from input port 1, (a) output port 5, (b) output port 6, (c) output port 7, (d) output port 8

As shown in Fig. 2-17, the 3 dB/90° hybrid couplers generated a phase difference of 90° between each output port, and showed attenuation characteristic of －3 dB. The phase and signal attenuation in Fig. 2-16 (a) produce a 45° phase and attenuation characteristic of －6 dB through two 3 dB/90° hybrid couplers and one －45° phase shifter. The remaining ports (6 to 8) are output in the same method, and the ideal phase output is shown in Table 2-1[45][46].

Table 2-1. Ideal output phase for each input port

Output port / Input port	Port 5	Port 6	Port 7	Port 8	Output between phase difference
	Phase	Phase	Phase	Phase	
Port 1	-45°	-90°	-135°	-180°	-45°
Port 2	-135°	0°	-225°	-90°	135°
Port 3	-90°	-225°	0°	-135°	-135°
Port 4	-180°	-135°	-90°	-45°	45°

As shown in Table 2-1, the 4 × 4 Butler matrix has a -45° phase difference when port 1 is fed, and each output port generated the phase of －45°, -90°, -135°, and -180°. Therefore, in order to control the direction of the main beam, the output phases must be sequentially supplied to the input ports of the antennas. Since each output port has a phase delay of -45°, 135°, -135°, and 45°, the main beam of the beamforming antenna can be controlled in four directions.

a. 3 dB/90° Slot-Directional Hybrid Coupler

Generally, directional hybrid couplers are used in systems to combine or divide signals, and these should have low insertion loss, good voltage standing wave ratio (VSWR), good isolation, directivity, and constant coupling over a wide bandwidth. The structure of the general directional hybrid coupler is shown in Fig. 2-18.

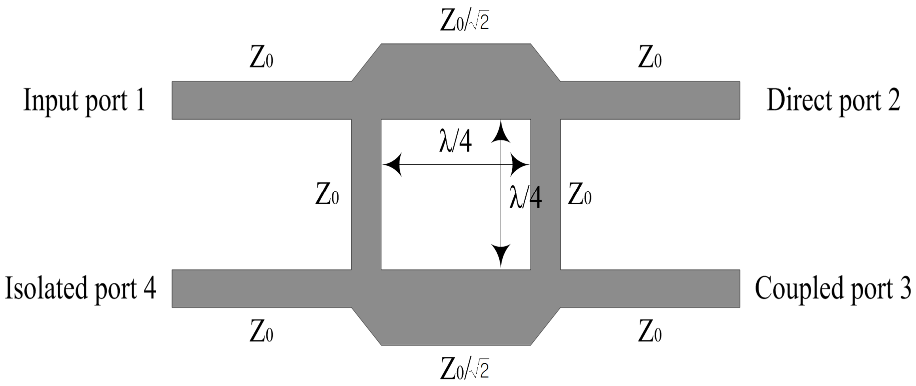

Fig. 2-18. Structure of general directional hybrid coupler

An applied signal in input port 1 of the directional hybrid coupler is coupled to ports 2 and 3, and port 4 is isolated. The structure of the directional hybrid coupler has four ports: input, through, coupled, and isolated ports. The important parameters of the directional coupler are directivity, isolation, and coupling factor. Therefore, the 3 dB/90 hybrid coupler is split equally into two signals at ports 2 and 3, and the two signals have a phase difference of 90°.

The frequency characteristics of the S-parameters of the basic 3 dB/90 hybrid coupler are shown in Fig. 2-19[47].

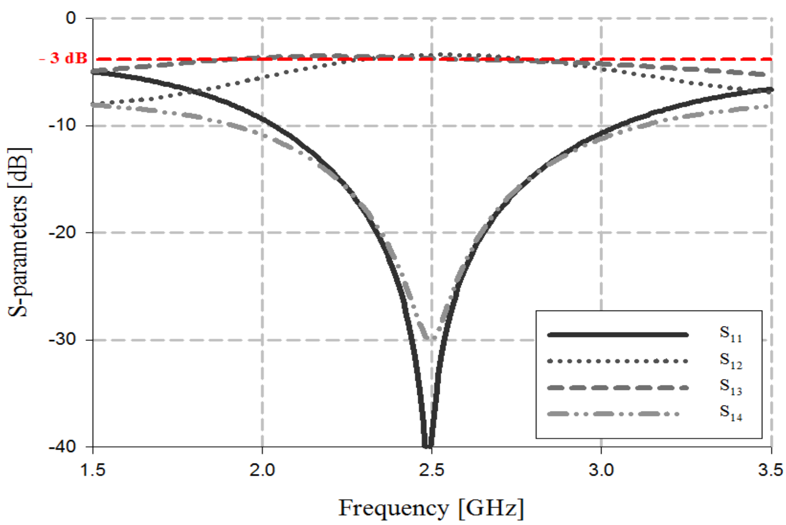

Fig. 2-19. Frequency characteristics of S-parameters

As shown in Fig 2-19, the 3 dB/90 hybrid coupler obtains a perfect 3 dB power division at ports 2 and 3, and perfect isolation and return loss at ports 4 and 1, respectively[48].

The proposed 3 dB/90° slot-directional hybrid couplers were fabricated on a laminated substrate to solve the structural problem in which a circuit increases. The structure of the proposed 3 dB/90° slot-directional hybrid couplers is shown in Fig. 2-20.

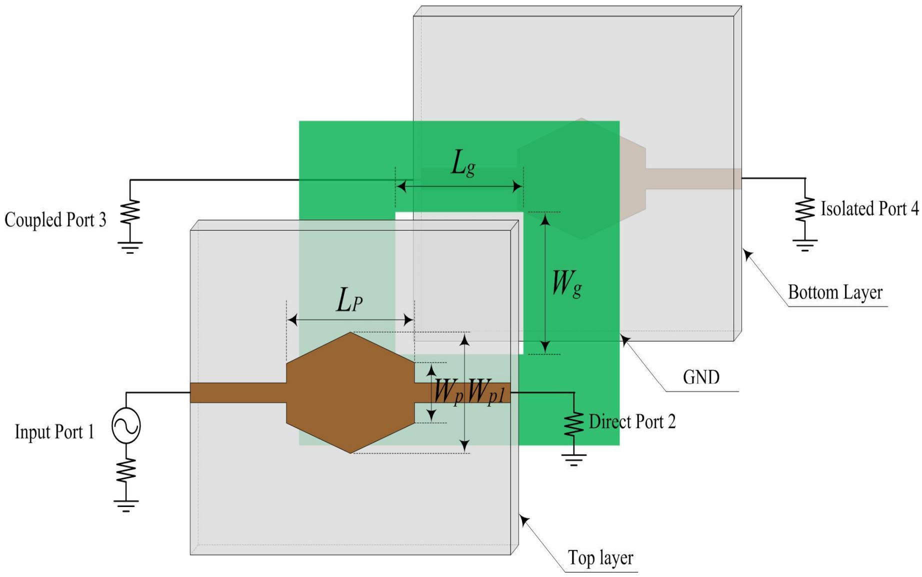

Fig. 2-20. Structure of the proposed 3 dB/90° slot-directional hybrid coupler

As shown in Fig. 2-20, the circuit that transmits the signal is placed on the top and bottom layer of the dielectric substrate, and the rectangular slot is inserted into the ground plane located between two substrates. The even/odd-mode electric field distribution of the proposed 3 dB/90° slot-directional hybrid coupler is shown in Fig. 2-21.

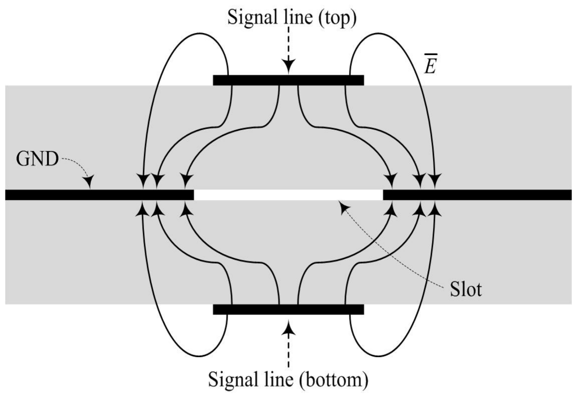

(a)

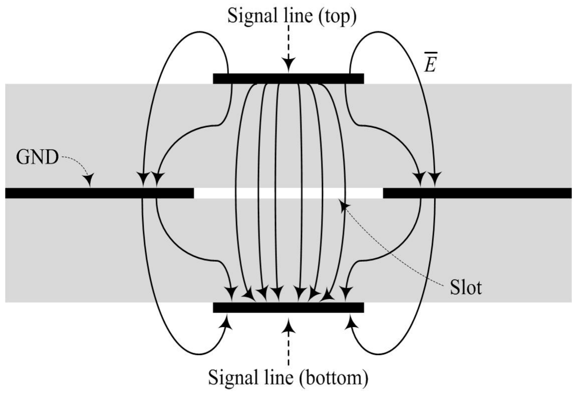

(b)

Fig. 2-21. The electric field distribution of a 3 dB/90° slot-directional hybrid coupler, (a) Even-mode, (b) Odd-mode

As shown in Fig. 2-21 (a), the electric field distribution of the even-mode is not coupled because the potential difference between the two lines is the same. On the other hand, the odd-mode electric field distribution in Fig. 2-21 (b) is coupled because of the potential difference between the two lines. Therefore, the characteristic impedance of the even-mode Z_{0e} and odd-mode Z_{0o} for the desired coupling value C_{dB} given by[43][49]

$$Z_{0e} = Z_0 \sqrt{\frac{1 + 10^{-C_{dB}/20}}{1 - 10^{-C_{dB}/20}}} \text{ and } Z_{0o} = Z_0 \sqrt{\frac{1 - 10^{-C_{dB}/20}}{1 + 10^{-C_{dB}/20}}}, \tag{2-12}$$

where the multiplication of the even/odd-mode characteristic impedance is $Z_{0e}Z_{0o}=Z_0^2$. When the coupling coefficient C_{dB} is 3 dB, the even/odd-mode characteristic impedance is 120.9 Ω and 20.6 Ω, respectively, according to equation (2-12).

From the even/odd mode analysis for the broadside coupled structure and conformal mapping method, the relationship between the even/odd mode characteristic impedances and the coupler dimensions is given by[49]

$$Z_{0e} = \frac{60\pi K(k_1)}{\sqrt{\varepsilon_r}K'(k_1)} \text{ and } Z_{0o} = \frac{60\pi K'(k_2)}{\sqrt{\varepsilon_r}K(k_2)}, \tag{2-13}$$

where $K'(k)$ and $K(k')$ are given by

$$K'(k) = K(k') = K(\sqrt{1-k^2});\ k' = \sqrt{1-k^2}. \tag{2-14}$$

In (2-14), $K(k)$ denotes the first kind elliptical integral. The parameters k_1 and k_2 are related to the coupling structure dimensions, and are given by

$$k_1 = \sqrt{\frac{\sinh^2(\pi^2 W_g/(4h))}{\sinh^2(\pi^2 W_g/(4h)) + \cosh^2(\pi^2 W_p/(4h))}}, \tag{2-15}$$

$$k_2 = \tanh^2(\pi^2 W_p/(4h)), \tag{2-16}$$

where h is the substrate thickness, and W_p and W_g are the widths of the microstrip patch placed on the top and bottom layers, and the rectangular slot inserted into the ground plane between the two substrates, respectively. An approximate equation for $K(k)/K'(k)$ is given by[50]

$$\frac{K(k)}{K'(k)} = \frac{K(k)}{K(k')} = \frac{2}{\pi}\ln\left(2\sqrt{\frac{1+k}{1-k}}\right),\ 0.5 \le k^2 \le 1 \tag{2-17}$$

$$= \frac{\pi}{2\ln\left(2\sqrt{\frac{1+\sqrt{1-k^2}}{1-\sqrt{1+k^2}}}\right)},\ 0 \le k^2 \le 0.5\,.$$

The length of the microstrip patch l_p and rectangular slot l_g can be calculated as a function of the effective wavelength λ_c and widths W_p and W_s of the microstrip patch[49][51].

$$l_p = \frac{\lambda_c}{4}\left[1-\left(\frac{\pi(W_p+W_g)}{4\lambda_c}\right)^2\right]^{-1} \tag{2-18}$$

b. 45° Phase Shifter

The 45° phase shifter consists of the phase coupler and microstrip line, and the structure is shown in Fig. 2-22. The design of the phase shifter is similar to that of the 3 dB/90° slot-directional hybrid coupler, and the microstrip line is placed on the top layer of the dielectric substrate.

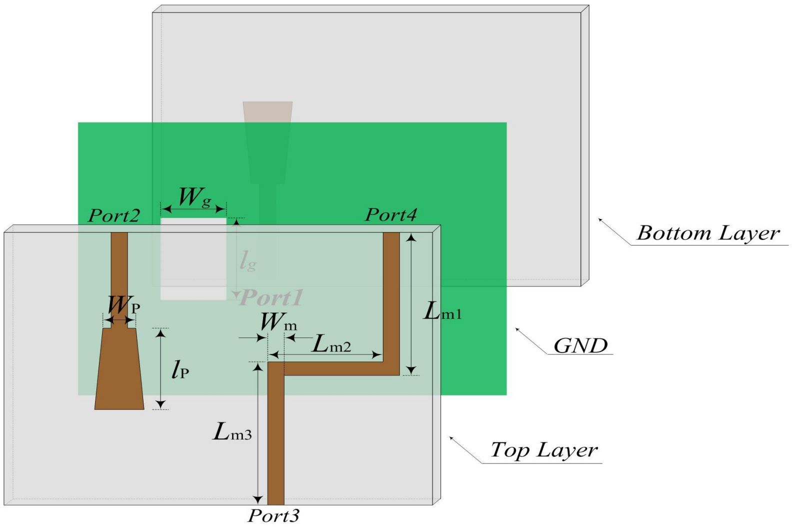

Fig. 2-22. Structure of the proposed 45° phase shifter

The microstrip line is printed on the dielectric substrate, which has the width W of the transmission line, thickness h of the dielectric substrate, and relative dielectric constant ε_r. The structure of the microstrip line is shown in Fig. 2-23.

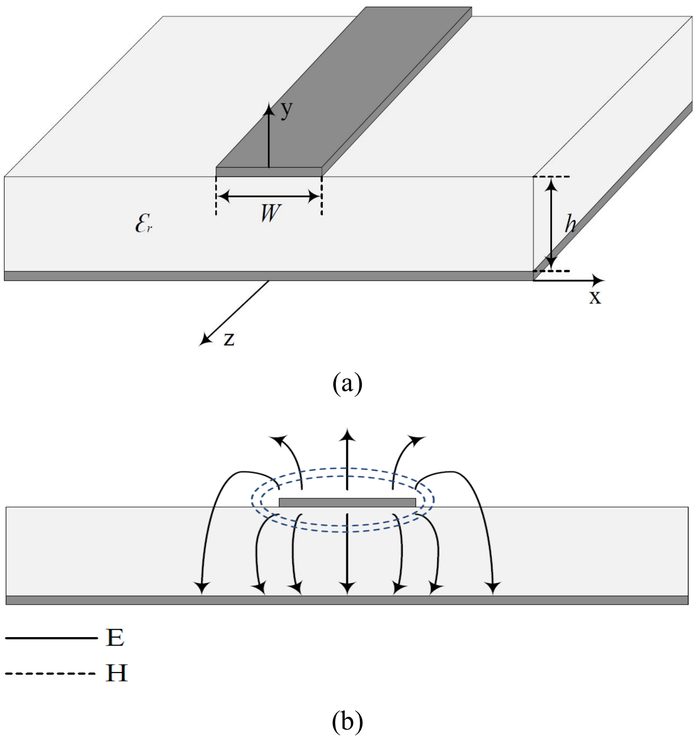

Fig. 2-23. Microstrip line, (a) Structure, (b) Electromagnetic line

As shown in Fig. 2-23 (b), because some of the field lines are in the dielectric substrate while some are in the air, the effective dielectric constant must satisfy the relation $1<\varepsilon_e<\varepsilon_r$. The effective dielectric constant ε_e is given by

$$\varepsilon_e = \frac{\varepsilon_r+1}{2}+\frac{\varepsilon_r-1}{2}\frac{1}{\sqrt{1+12h/W}} \quad . \tag{2-19}$$

The effective dielectric constant ε_e is determined by the relative dielectric constant ε_r, width W of the microstrip line, and thickness h of the dielectric substrate.

The width of the microstrip line determines the impedance Z_0, and the wider the microstrip line, the smaller the impedance; the narrower the microstrip line, the larger the impedance.

$$Z_0 = \begin{cases} \dfrac{60}{\sqrt{\varepsilon_e}}\ln\left(\dfrac{8h}{W}+\dfrac{W}{4h}\right) & [\Omega]\,(W/h \le 1) \\ \dfrac{120\pi}{\sqrt{\varepsilon_e\left[W/h+1.393+0.667\ln(W/h+1.444)\right]}} & [\Omega]\,(W/h > 1). \end{cases} \tag{2-20}$$

From characteristic impedance Z_0 and the relative dielectric constant ε_r, the ratio W/h of the dielectric substrate thickness and the width of microstrip is given by:

$$\frac{W}{h} = \begin{cases} 8e^{A}/(e^{2A}-2) & (W/h \le 2) \\ \dfrac{2}{\pi}\left[B-1-\ln(2B-1)+\dfrac{\varepsilon_r-1}{2\varepsilon_r}\left\{\ln(B-1)+0.39-\dfrac{0.61}{\varepsilon_r}\right\}\right] & (W/h > 2), \end{cases} \tag{2-21}$$

where A and B are calculated by equations (2-22) and (2-23), respectively.

$$A = \frac{Z_0}{60}\sqrt{\frac{\varepsilon_r + 1}{2}} + \frac{\varepsilon_r - 1}{\varepsilon_r + 1}(0.23 + \frac{0.11}{\varepsilon_r}). \quad (2\text{-}22)$$

$$B = 377\pi / (2Z_0\sqrt{\varepsilon_r}). \quad (2\text{-}23)$$

The design of the microstrip line is determined by the dielectric constant of the substrate, thickness of the dielectric substrate, thickness of the metal, line width, etc[52].

Ⅲ Design and Analysis of Beamforming Antenna

3.1 Implementation of UWB Antenna

3.1.1 Design and Simulation Analysis of Tapered-Slot Antenna

TSAs are simple to manufacture owing to their low profile and they have infinite bandwidth. The desired bandwidth can be derived through the physical size of the radiator and various design techniques[53-55].

The important parameters of the TSA are the antenna length L_T, aperture width W_T, and substrate thickness h. The directivity of the antenna length is given by

$$D = 10\frac{L_T}{\lambda_0}. \tag{3-1}$$

The directivity (D) of the TSA must satisfy the lengths 3 λ_g to 4 λ_g. Generally, the TSA operates as a surface wave antenna by separating electromagnetic waves along the tapered aperture. In order to operate as a stable surface-wave antenna, the following substrate requirement must be satisfied:

$$0.005 < \frac{t_{eff}}{\lambda_0} = \left(\sqrt{\varepsilon_r} - 1\right)\frac{t}{\lambda_0} < 0.03, \tag{3-2}$$

where t_{eff} is the effective thickness, ε_r is the relative permittivity, and t is the thickness of the dielectric substrate[39][56].

The aperture size of the TSA is determined by the minimum frequency of the operating frequency. Since wavelength is inversely proportional to frequency, the antenna at minimum frequency should be able to transmit a signal with the longest wavelength. In order to transmit the signal with the longest wavelength on a dielectric substrate, the following equation must be satisfied:

$$W_t = \frac{\lambda_g}{2} = \frac{c}{2f_{\min}\sqrt{\varepsilon_e}}. \tag{3-3}$$

The TSA operates as a resonance antenna at low-frequency $f_{\min}$, where ε_e is the effective dielectric constant and c is the velocity of light[57]. The structure of the proposed TSA is shown in Fig. 3-1.

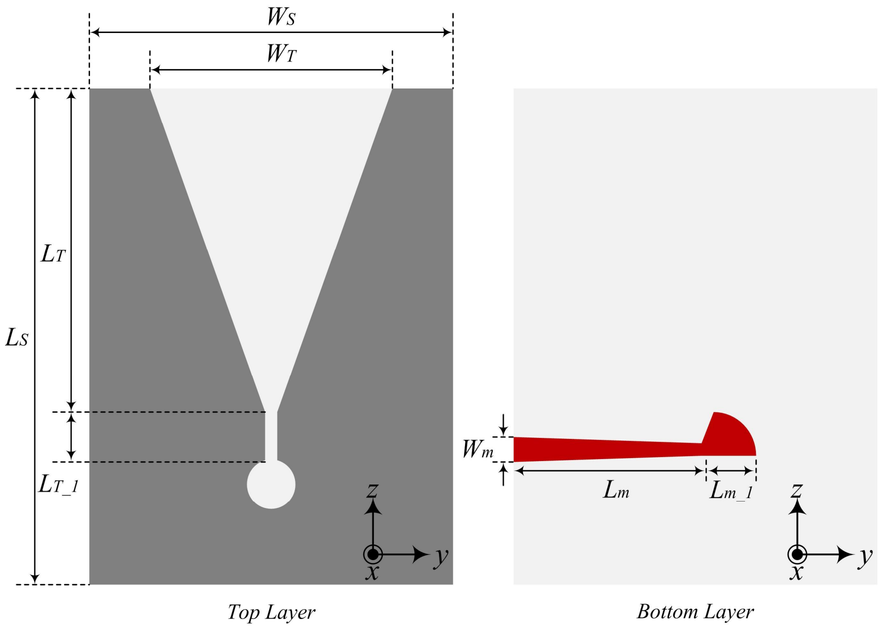

Fig. 3-1. Structure of the proposed tapered-slot antenna

As shown in Fig 3-1, the radiation element is placed on the top layer of the proposed TSA, while the transition feed is placed on the bottom layer. The overall parameters of the proposed TSA are listed in Table 3-1.

Table 3-1. Overall parameters of the proposed tapered-slot antenna

(Unit: ㎜)

Parameters	L_S	W_S	L_T	L_{T_1}	W_T	L_m	L_{m_1}	W_m
Overall size	140	90	96.8	23	80	45	15	5

The proposed TSA was analyzed using HFSS ver. 12 (Ansys Co.), a 3D high-frequency analysis simulation design tool. The TSA structure designed using HFSS is shown in Fig. 3-2.

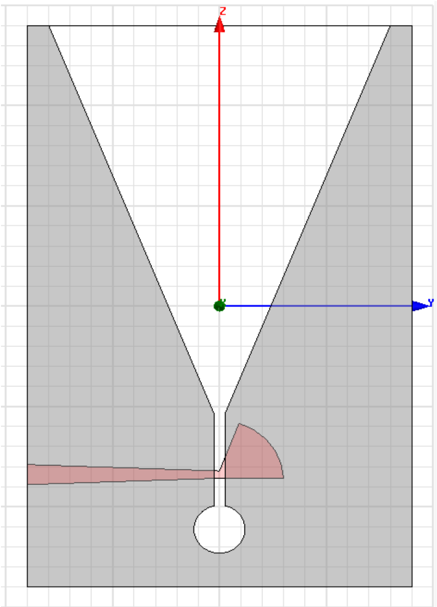

Fig. 3-2. The antenna structure implemented using HFSS

The proposed TSA was designed using a Taconic TLY substrate, which has a relative permittivity of 2.2, loss tangent of 0.0009, and thickness of 1.52 ㎜. The impedance bandwidth simulation analysis of the antenna was conducted through the return loss S_{11} and VSWR, as shown in Fig. 3-3.

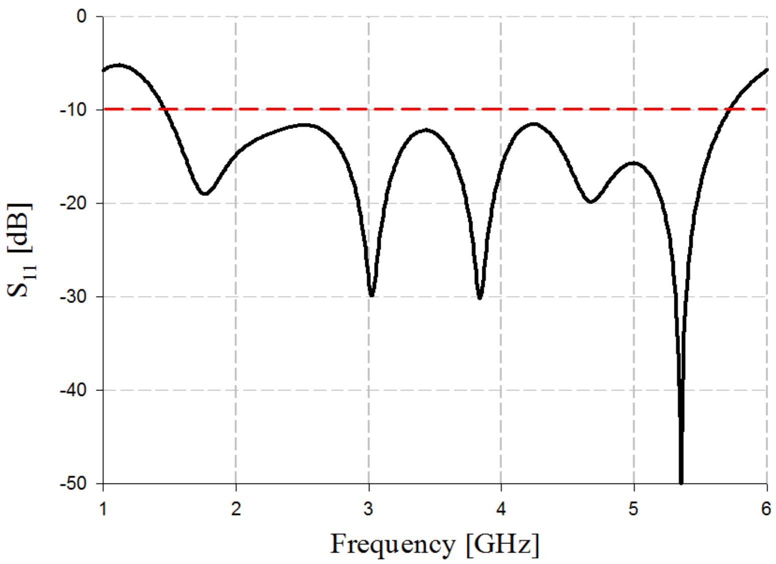

(a)

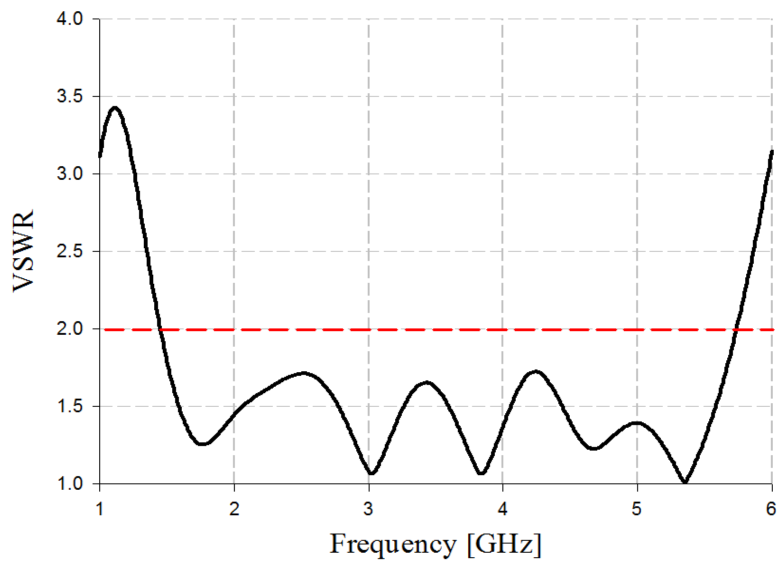

(b)

Fig. 3-3. The impedance bandwidth simulation analysis of the proposed tapered-slot antenna, (a) S_{11}, (b) VSWR

The simulation results in Fig. 3-3 show that the antenna achieved a wide bandwidth of 4.29 ㎓, which was satisfied by -10 ㏈ S_{11} and VSWR≤2 at in the 1.45～5.74 ㎓ band.

The current distribution simulation analysis of the proposed tapered slot antenna is shown in Fig. 3-4.

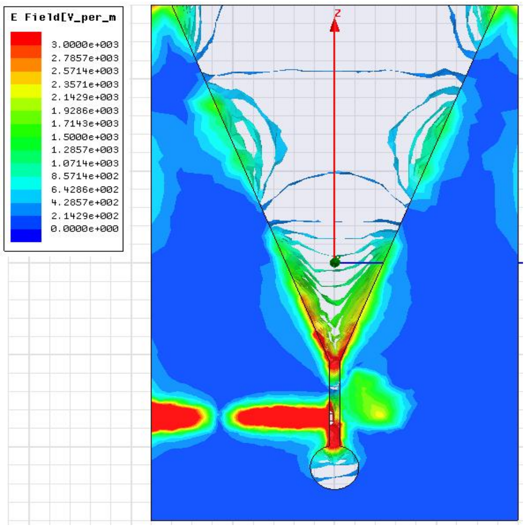

(a)

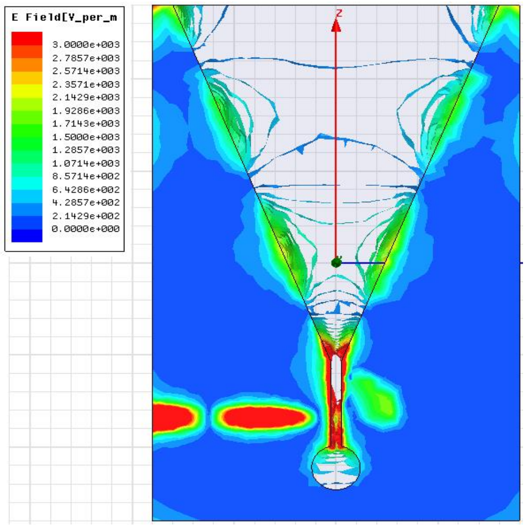

(b)

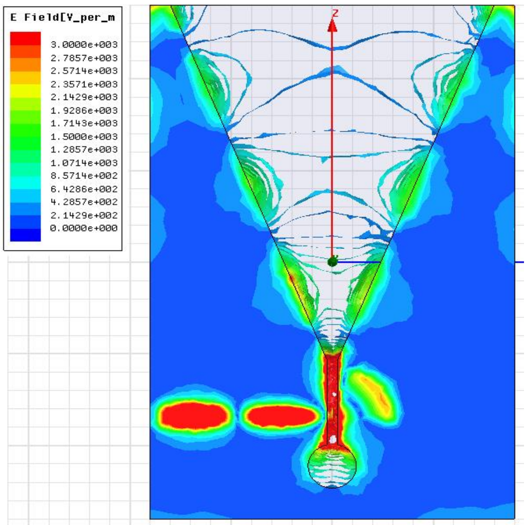

(c)

Fig. 3-4. Simulation analysis of the current distribution for the proposed antenna, (a) 3 ㎓ band, (b) 4 ㎓ band, (c) 5 ㎓ band

The simulation results in Fig. 3-4 show that the current distribution of the proposed TSA radiated along the tapered aperture in the 3～5 ㎓ band. Therefore, the proposed TSA operates as a surface wave antenna.

The radiation patterns of the proposed TSA were analyzed in the E-plane (y-z) and H-plane (x-z), as shown in Fig. 3-5.

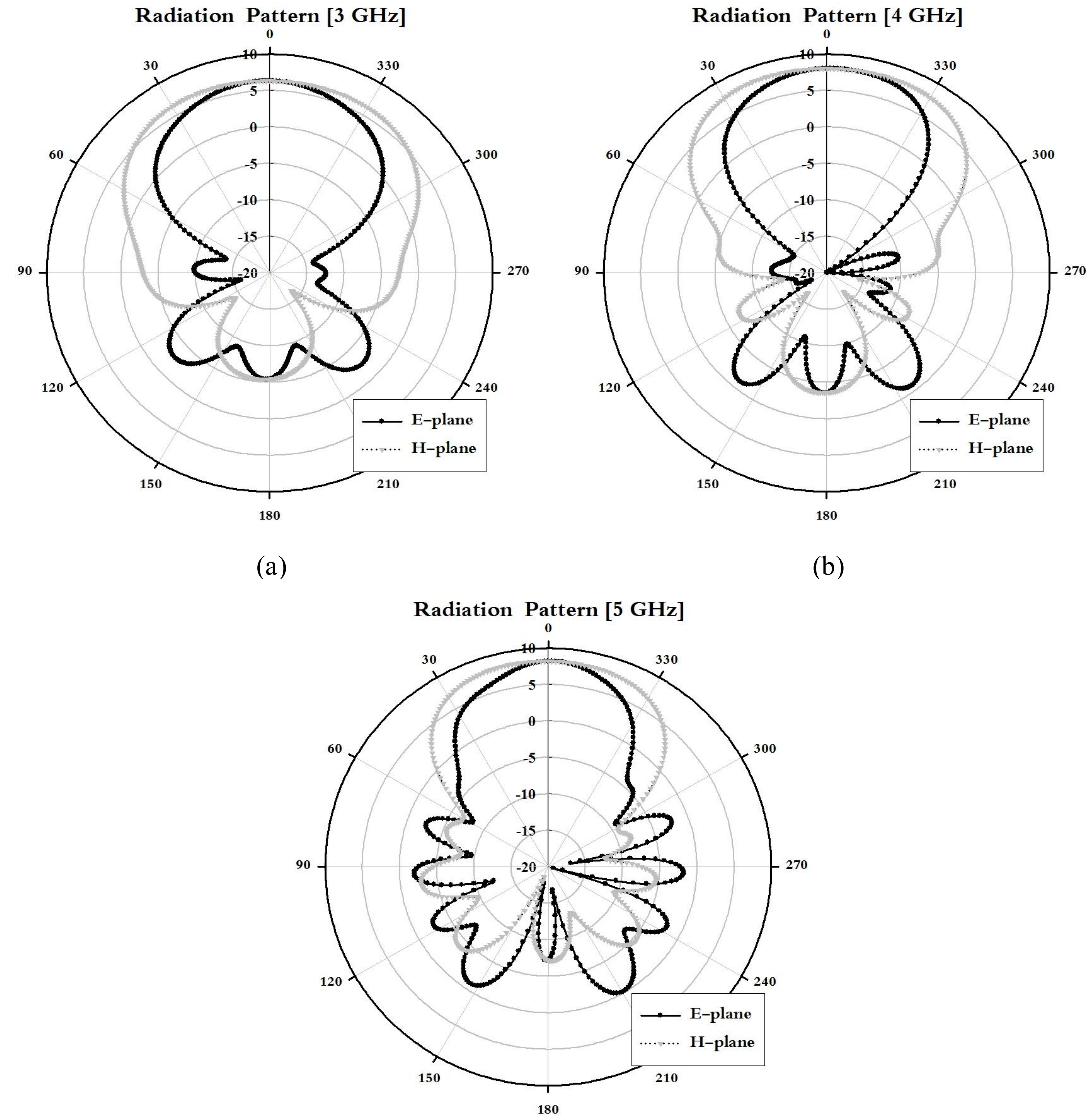

(a) (b)

(c)

Fig. 3-5. Simulation analysis of the radiation patterns for the proposed antenna, (a) 3 ㎓ band, (b) 4 ㎓ band, (c) 5 ㎓ band

The simulation results in Fig. 3-5 show that the E-plane and H-plane radiation patterns of the proposed TSA exhibited directivity of an end-fire that increased the sensitivity for a certain direction. The results of the gain and 3 ㏈ beamwidth simulation analysis of the proposed antenna are shown in Fig. 3-6 and Table 3-2.

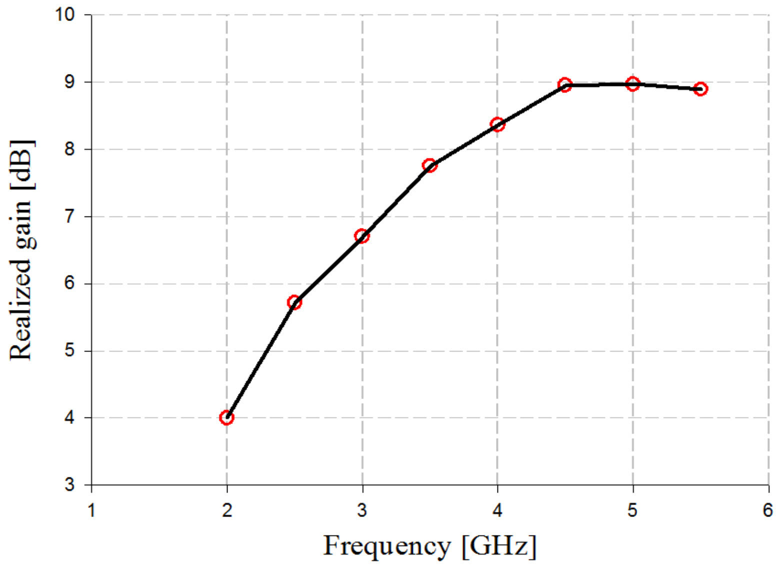

Fig. 3-6. Simulation analysis of the gain of the proposed antenna

Table 3-2. The simulation results of gain and 3 dB beamwidth of the proposed tapered-slot antenna

Frequency [㎓]	**Gain [dBi]**	**3-dB beamwidth**	
		E-plane	**H-plane**
3	6.70	70.45°	117.00°
4	8.36	58.03°	96.38°
5	8.97	36.48°	72.25°

The simulation results in Fig. 3-6 and Table 3-2 show that the gain of the proposed TSA was 6.70 dBi, 8.36 dBi, and 8.97 dBi in the 3 ㎓, 4 ㎓, and 5 ㎓ band, respectively. Furthermore, the 3 dB beamwidth results of the E-plane and H-plane were 70.45° and 117.00° in the 3 ㎓ band, 58.03° and 96.38° in the 4 ㎓ band, and 36.48° and 72.25° in the 5 ㎓ band, respectively.

3.2 Implementation of 4 × 4 Butler Matrix

This chapter discusses the implementation of the proposed 4 × 4 Butler matrix. The proposed 4 × 4 Butler matrix consists of the 3 ㏈/90° slot-directional hybrid couplers and 45° phase shifters, and it has four input/output ports.

The 4 × 4 Butler matrix was analyzed using HFSS (Ansys Co.), and was designed as a laminated substrate structure using two Taconic TRF-45 substrates. The structure of the proposed 4 × 4 Butler matrix is shown in Fig. 3-7.

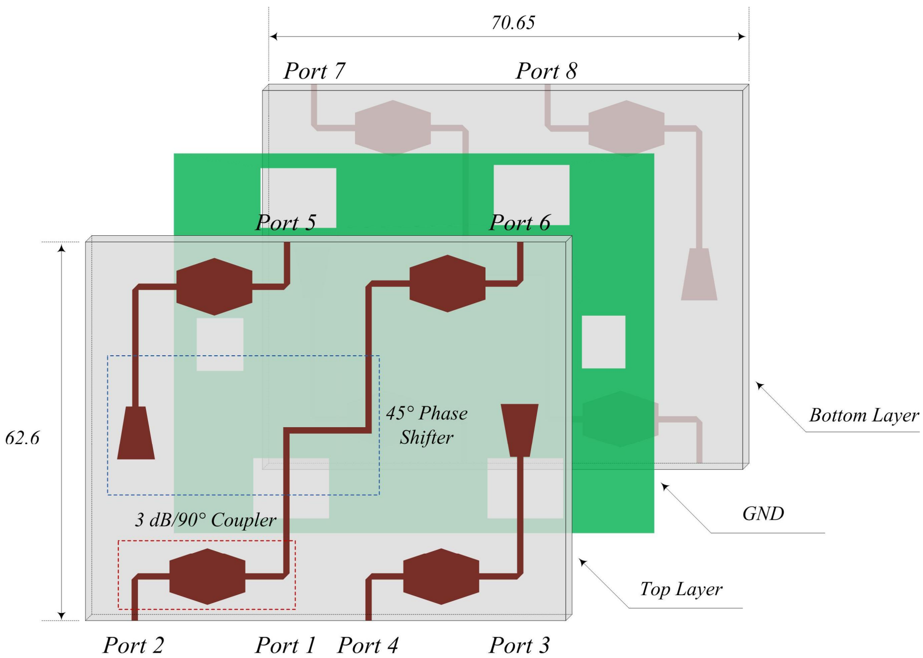

Fig. 3-7. Structure of the proposed 4 × 4 Butler matrix

3.2.1 Analysis of the 3 ㏈/90° Slot-Directional Hybrid Coupler

The proposed 3 ㏈/90° slot-directional hybrid coupler was designed as a laminated substrate using two TRF-45 substrates, which have relative permittivity of 4.5, loss tangent of 0.0035, and thickness of 0.61 ㎜. Details on the structure and overall size are shown in Fig. 3-8 and Table 3-3.

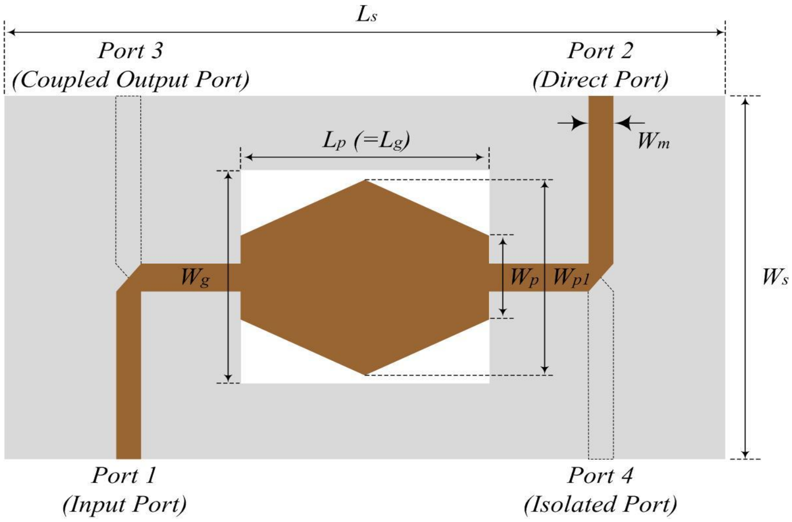

(a)

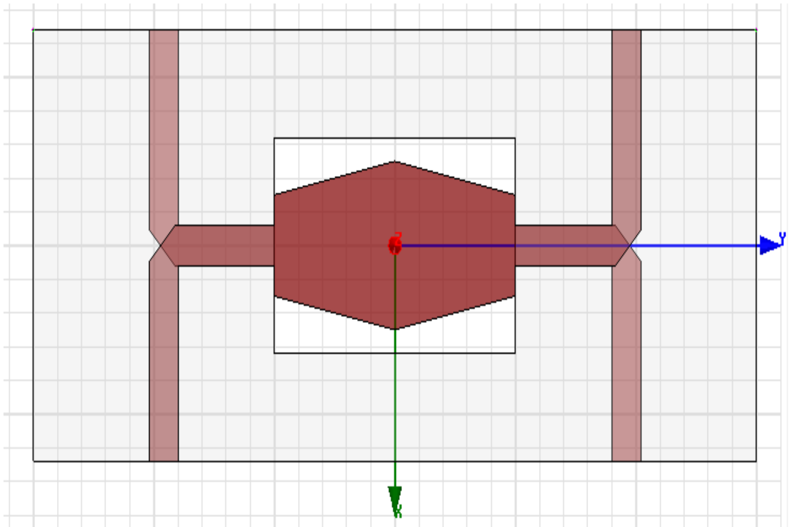

(b)

Fig. 3-8. Configuration of the proposed 3 dB/90° slot-directional hybrid coupler, (a) Structure, (b) The designed structure using HFSS

Table 3-3. Overall size of the proposed 3 dB/90° slot-directional hybrid coupler

(Unit: ㎜)

Parameters	L_S	W_S	L_p	W_p	W_{p1}	L_g	W_g	W_m
Overall size	30	12.8	10	3	5	10	6.4	1.2

The proposed 3 dB/90° slot-directional hybrid coupler consists of four ports: input port, direct port, coupled port, and isolated port. It is placed on the two signal lines on the top layer and bottom layer. The ground plane of the intermediate layer is inserted into a rectangular slot, and its structure is mutually coupled. The amount of the transmitted signal was determined by the length of the coupling patch l_p, width of the coupling patch W_p, W_{p1} and width of the rectangular coupling slot W_g. Therefore, the characteristics of the proposed 3 dB/90° slot-directional hybrid coupler was achieved by adjusting the parameters l_p, W_p, W_{p1} and W_g.

The S-parameters of the proposed 3 dB/90° slot-directional hybrid coupler were analyzed in terms of return loss S_{11}, isolation S_{41}, and insertion loss S_{21}, S_{31}, which are shown in Fig. 3-9.

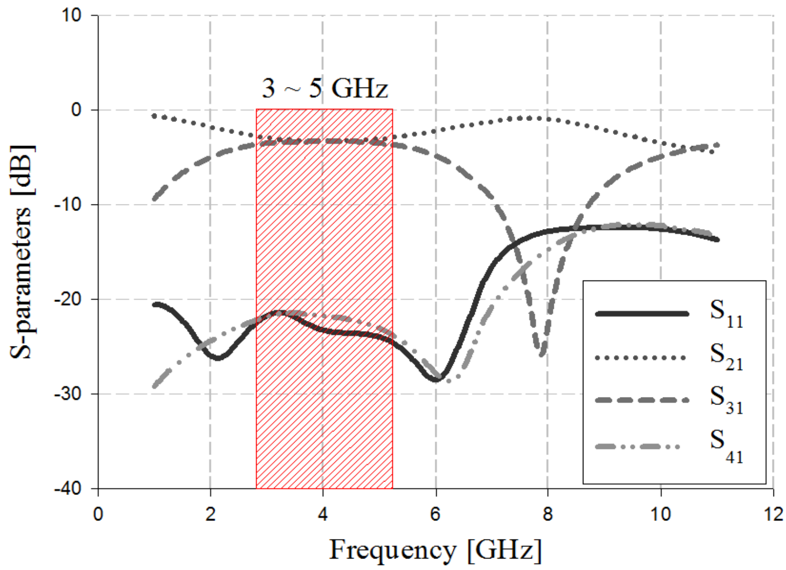

Fig. 3-9. S-parameters simulation analysis of the proposed coupler

The simulation results in Fig. 3-9 show that the return loss S_{11} and isolation S_{41} are observed the good results, which is the lower results than －20 dB in the 3－5 ㎓ band. The insertion loss S_{21} and S_{31} was 3 dB in the 3 ～ 5 ㎓ band; overall, the observed the error was ±0.4 dB.

The results of the phase and phase difference simulation analysis of the proposed 3 ㏈/90° slot-directional hybrid coupler are shown in Fig. 3-10.

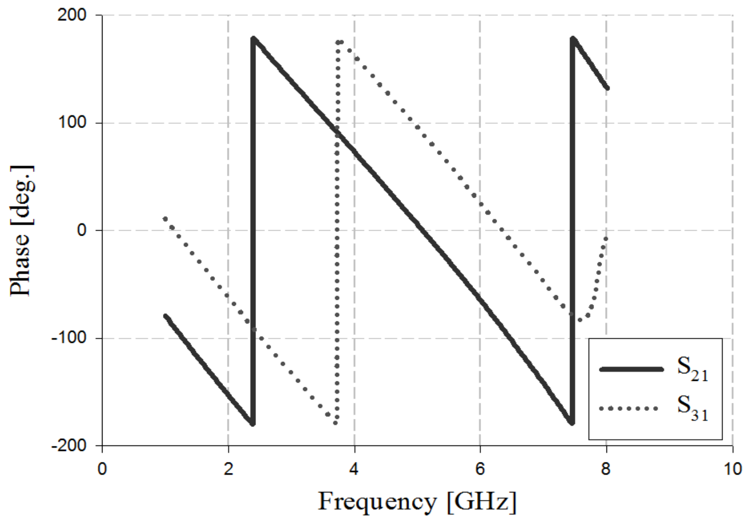

(a)

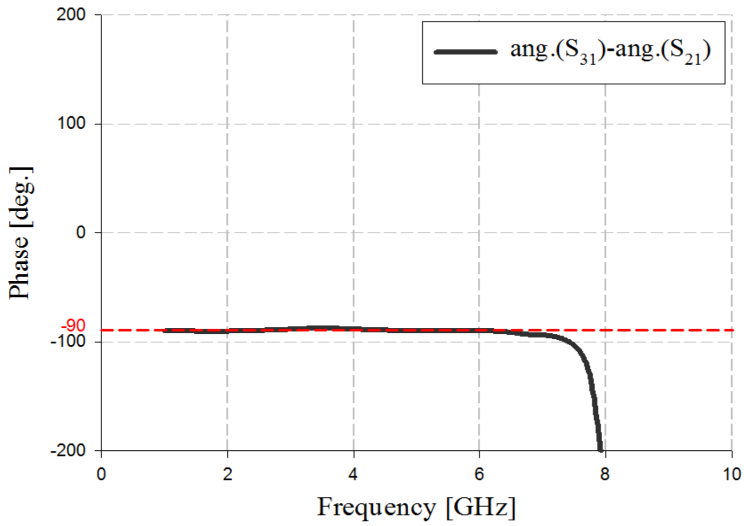

(b)

Fig. 3-10. Phase and phase difference simulation analysis of the proposed coupler, (a) Phase, (b) Phase difference

The simulation results in Fig. 3-10 show that the S_{31} and S_{21} phases of the proposed 3 ㏈/90° slot-directional hybrid coupler are 227° and 138° in 3 ㎓ band, 161° and 72° in 4 ㎓ band, and 95° and 5° in 5 ㎓ band, respectively. The simulation analysis of the phase difference has an error of ±2° at 90°.

3.2.2 Analysis of the 45° Phase Shifter

The proposed 45° phase shifter was designed as a laminated substrate using two TRF-45 substrates, which have a relative permittivity of 4.5, loss tangent of 0.0035, and thickness of 0.61 ㎜. Details on the structure and overall size are shown in Fig. 3-11 and Table 3-4.

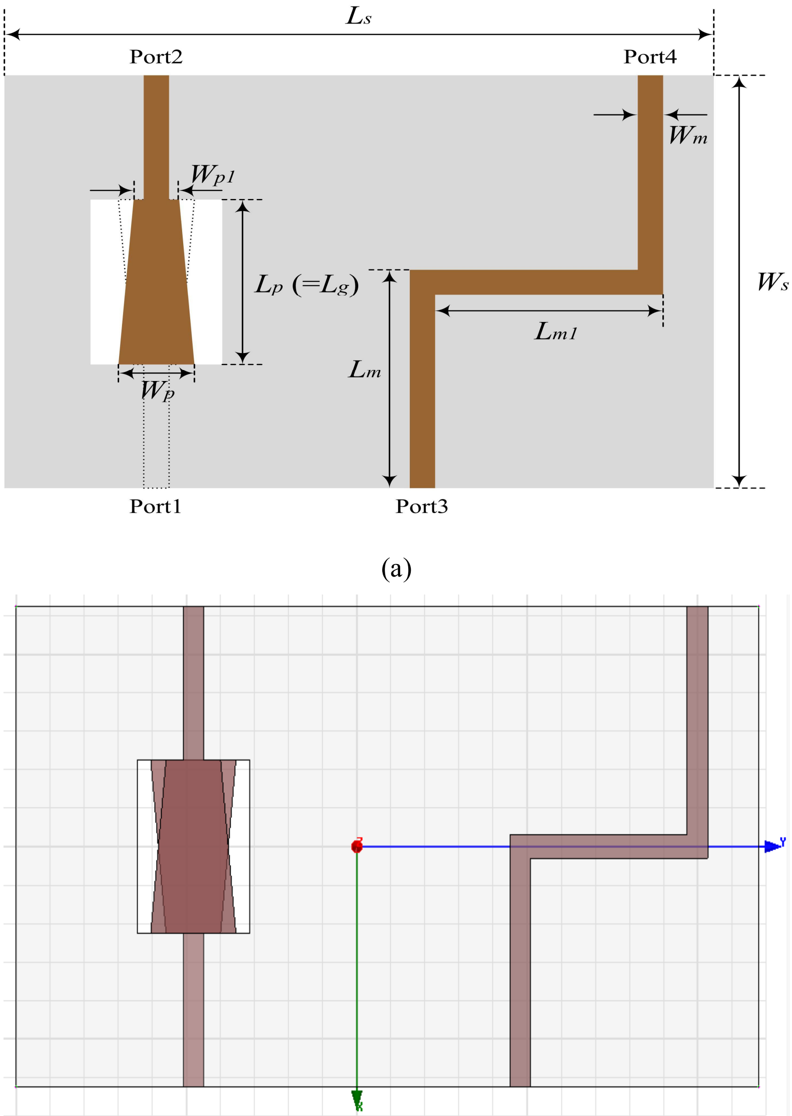

(a)

(b)

Fig. 3-11. Configuration of the proposed 45° phase shifter, (a) Structure, (b) The designed structure using HFSS

Table 3-4. Overall size of the proposed 45° phase shifter

(Unit: ㎜)

Parameters	L_S	W_S	L_p	W_p	W_{p1}	L_m	L_{m1}	W_m
Overall size	43.6	25	9	5	3.2	13.1	10.4	1.2

The proposed 45° phase shifter was placed on the top layer and bottom layer. The ground plane of the intermediate layer was inserted into a rectangular slot, and its structure was mutually coupled. The amount of the transmitted signal was determined by the length of the coupling patch l_p, width of the coupling patch W_p, W_{p1} and width of the rectangular coupling slot W_g. Therefore, the characteristics of the proposed 45° phase shifter was achieved by adjusting the parameters l_p, W_p, W_{p1} and W_g.

The S-parameter simulation results of the proposed 45° phase shifter was analyzed in terms of return loss S_{11} and insertion loss S_{21}, which are shown in Fig. 3-12.

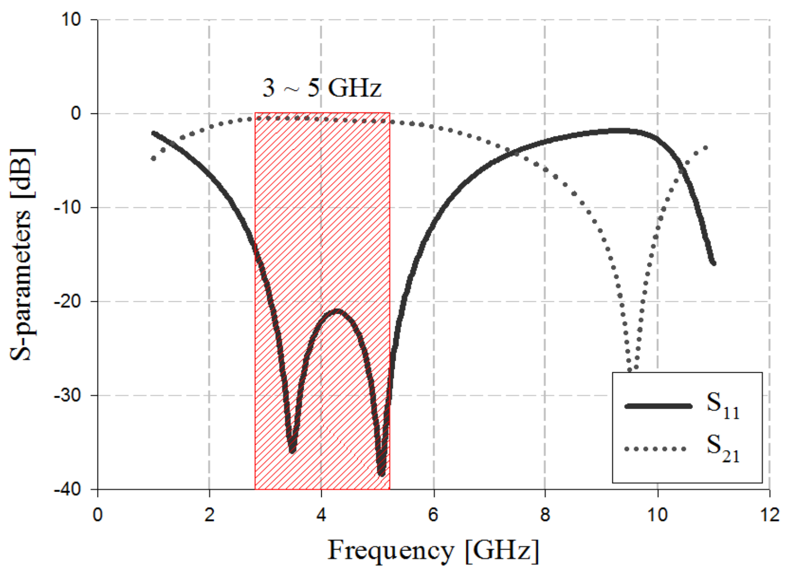

Fig. 3-12. S-parameters simulation analysis of the proposed shifter

The simulation results in Fig. 3-12 show that the return loss S_{11} are observed the good results which is less than -20 ㏈ in the 3 ~ 5 ㎓ band. The insertion loss S_{21} was between -0.4 and -0.7 ㏈ in the 3 ~ 5 ㎓ band.

The results of the phase and phase difference simulation analysis of the proposed 45° phase shifter are shown in Fig. 3-13.

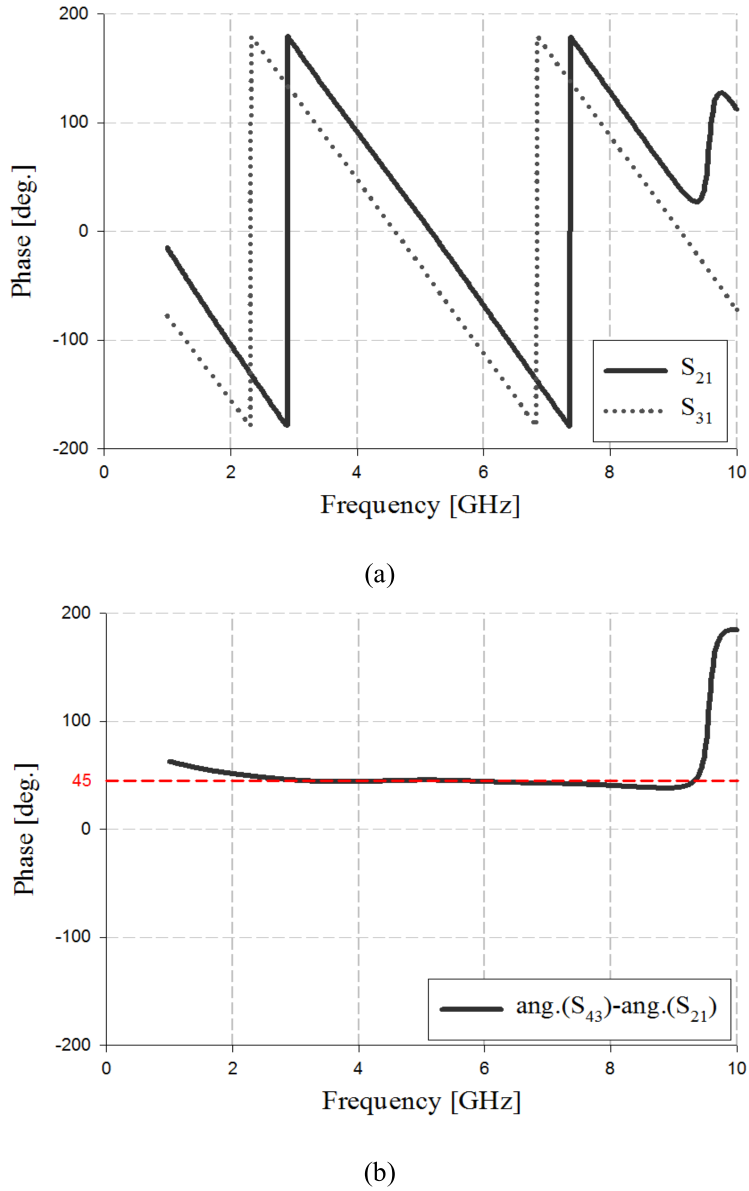

Fig. 3-13. Phase and phase difference simulation analysis of the proposed 45° phase shifter, (a) Phase, (b) Phase difference

The simulation results in Fig. 3-13 show that the S_{21} and S_{43} phases of the proposed 45° phase shifter are 171° and 125° in 3 ㎓ band, 91° and 46° in 4 ㎓ band, and 12° and -32° in 5 ㎓ band, respectively. The phase difference simulation analysis had an error of ±2° at 45°.

The simulation results for the overall analysis of the proposed coupler and shifter are listed in Table 3-5 and Table 3-6.

Table 3-5. Overall analysis of the proposed coupler

Parameters / Frequency	Phase		Phase difference	Return loss S_{11}	Insertion loss S_{21}	Isolation S_{31}, S_{41}
3 ㎓	S_{21}	138°	89°	S_{11} ≤ -20 dB	3 dB ± 0.4 dB	S_{31}, S_{41} ≤ -20 dB
	S_{31}	227°				
4 ㎓	S_{21}	72°	89°			
	S_{31}	161°				
5 ㎓	S_{21}	5°	90°			
	S_{31}	95°				

Table 3-6. Overall analysis of the proposed shifter

Parameters / Frequency	Phase		Phase difference	Return loss S_{11}	Insertion loss S_{21}	Isolation S_{31}, S_{41}
3 ㎓	S_{21}	171°	46°	S_{11} ≤ -20 dB	-0.4 dB ~ -0.7 dB	-
	S_{43}	125°				
4 ㎓	S_{21}	91°	45°			
	S_{43}	46°				
5 ㎓	S_{21}	12°	44°			
	S_{43}	-32°				

The results in Table 3-5 and 3-6 show that the return loss of the proposed coupler and shifter is very low, and has good insertion loss and isolation characteristics. Furthermore, the phase difference of the coupler and shifter was approximately 90° and 45° within the proposed bandwidth, respectively.

3.2.3 Analysis of the 4 × 4 Butler Matrix

The overall size of the proposed 4 × 4 Butler matrix is 70.65 × 62.6 × 1.22 ㎣. The structure of the proposed 4 × 4 Butler matrix is shown in Fig. 3-14.

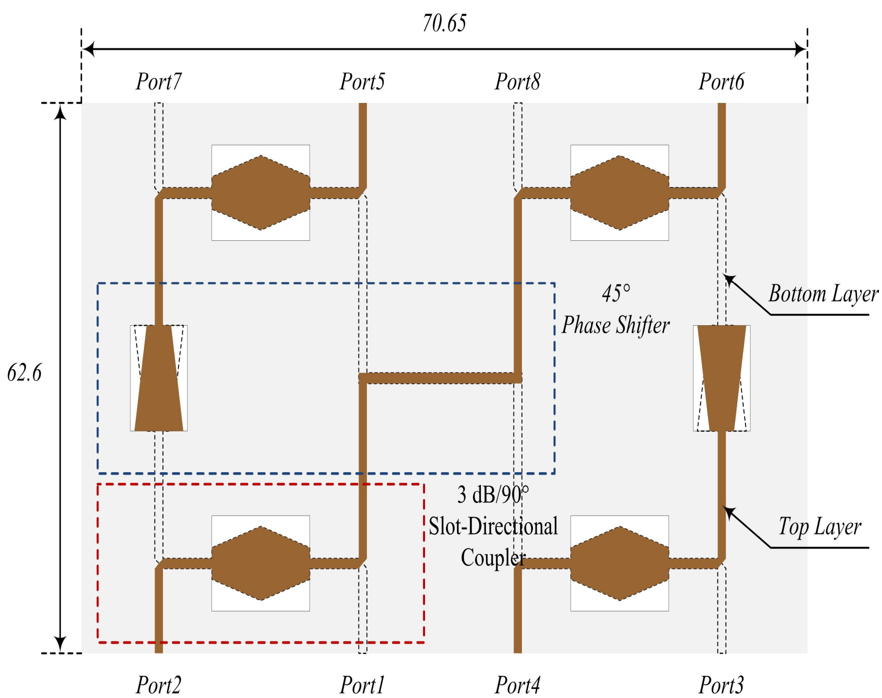

(a)

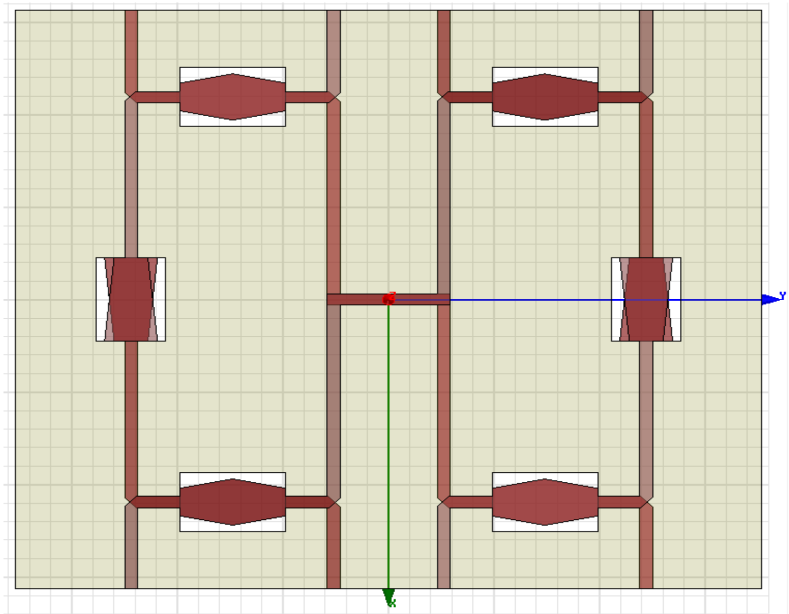

(b)

Fig. 3-14. Configuration of the proposed 4×4 Butler matrix, (a) Structure, (b) The designed structure using HFSS

As shown in Fig. 3-14, the proposed matrix has four input ports and four output ports, with each port generating a different phase. The top and bottom layers of the 4 × 4 Butler matrix consist of the 3 dB/90° slot-directional hybrid couplers and the 45° phase shifters, and the six coupling slots are inserted into the ground plane between the two substrates. Each port is connected to a connector.

a. Analysis of S-parameters

The S-parameter simulation of the proposed 4 × 4 Butler matrix analyzed the return loss, isolation, and insertion loss. The results of the S-parameter simulation analysis for input port 1 are shown in Fig. 3-15.

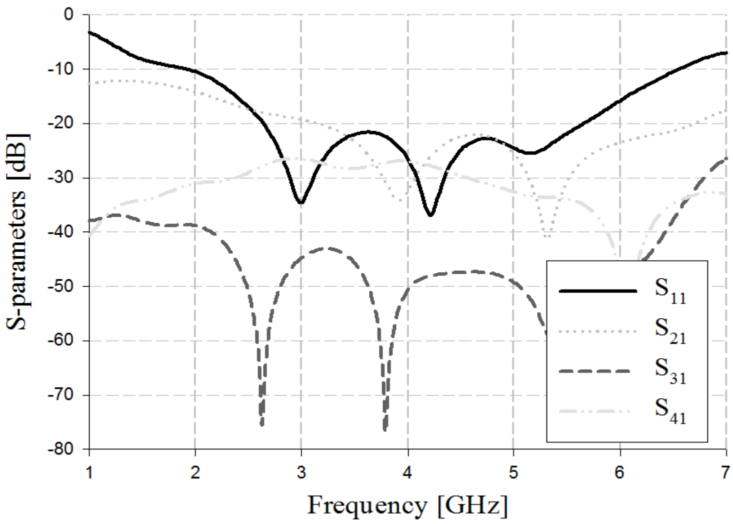

(a)

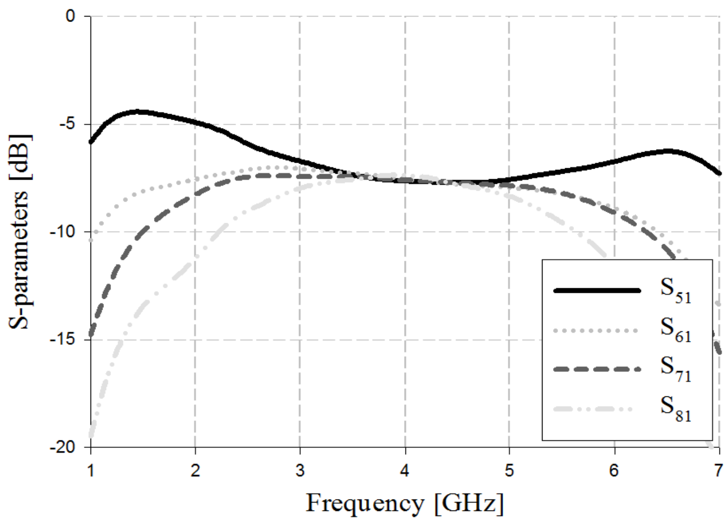

(b)

Fig. 3-15. Simulation analysis of S-parameters for input port 1,

(a) Return loss & isolation, (b) Insertion loss

The simulation results in Fig. 3-15 show that the return loss S_{11} and isolation S_{21}, S_{31}, and S_{41} are less than -20 dB within the proposed bandwidth. The insertion loss S_{51}, S_{61}, S_{71}, and S_{81} was low at approximately 6 ~ 6.7 dB within the proposed bandwidth.

The results of the S-parameter simulation analysis for input port 2 are shown in Fig. 3-16.

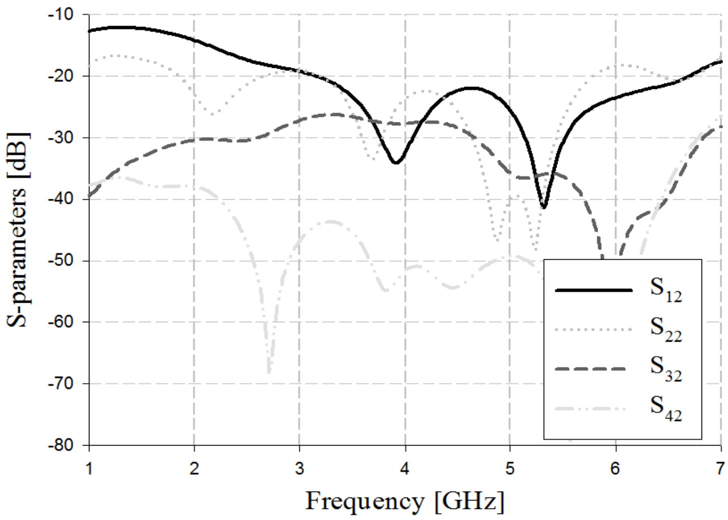

(a)

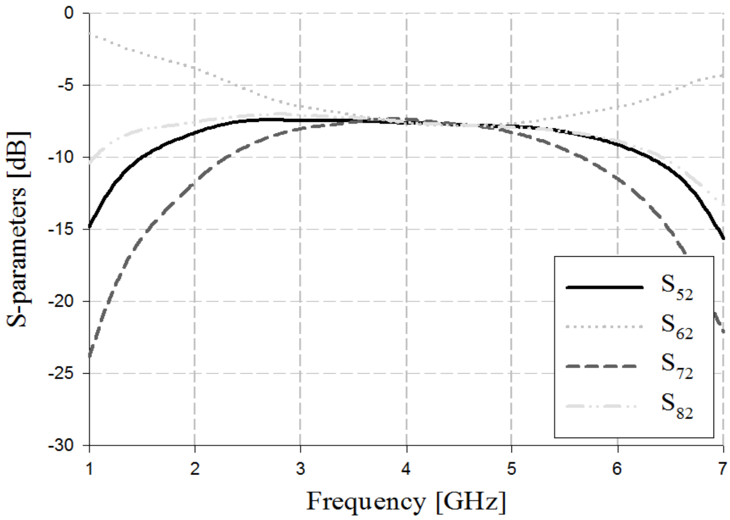

(b)

Fig. 3-16. Simulation analysis of S-parameters for input port 2, (a) Return loss & isolation, (b) Insertion loss

The simulation results in Fig. 3-16 show that the return loss S_{22} and isolation S_{12}, S_{32}, and S_{42} are less than -20 dB within the proposed bandwidth. The insertion loss S_{52}, S_{62}, S_{72}, and S_{82} was low at approximately 6 ~ 7.4 dB within the proposed bandwidth.

The results of the S-parameter simulation analysis for input port 3 are shown in Fig. 3-17.

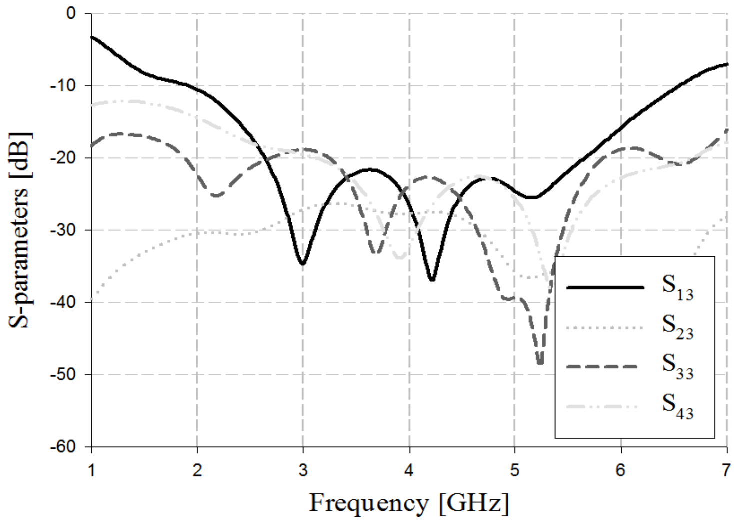

(a)

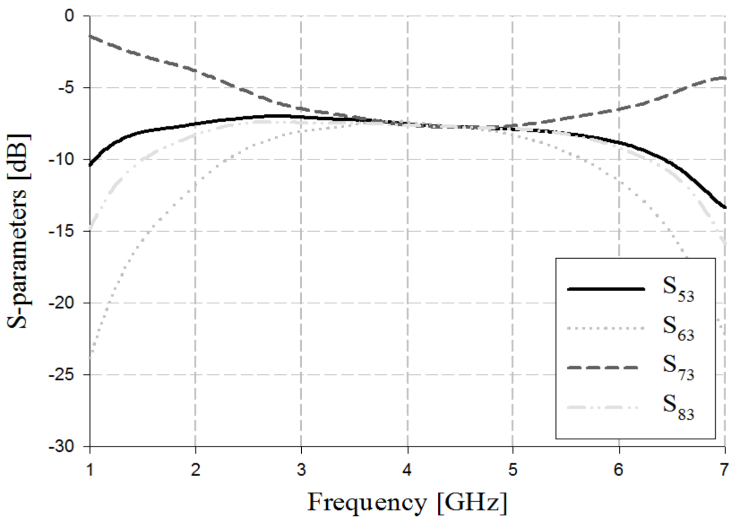

(b)

Fig. 3-17. Simulation analysis of S-parameters for input port 3,

(a) Return loss & isolation, (b) Insertion loss

The simulation results in Fig. 3-16 show that the return loss S_{33} and isolation S_{13}, S_{23}, and S_{43} are less than -20 dB within the proposed bandwidth. The insertion loss S_{53}, S_{63}, S_{73}, and S_{83} was low at approximately 6.5 ~ 7.5 dB within the proposed bandwidth.

The results of the S-parameter simulation analysis for input port 4 are shown in Fig. 3-18.

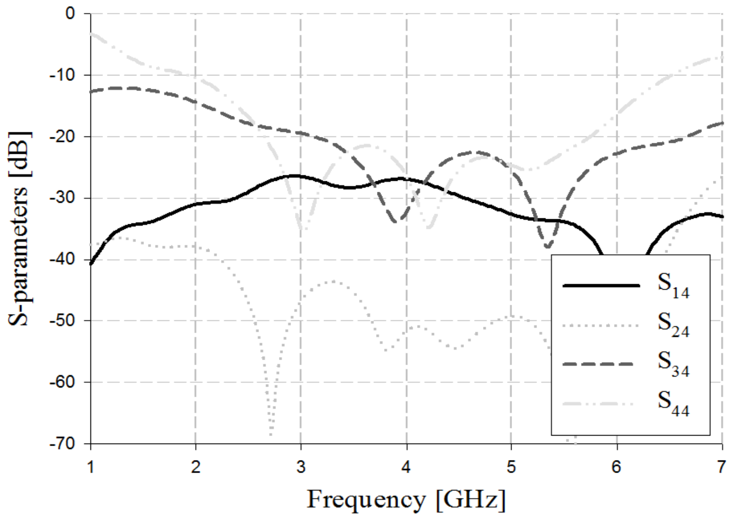

(a)

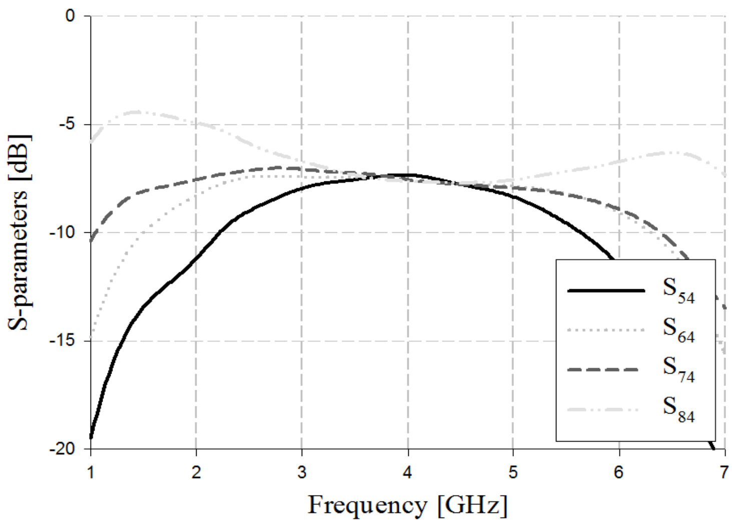

(b)

Fig. 3-18. Simulation analysis of S-parameters for input port 4,

(a) Return loss & isolation, (b) Insertion loss

The simulation results in Fig. 3-18 show that the return loss S_{44} and isolation S_{14}, S_{24}, and S_{34} are less than -20 dB within the proposed bandwidth. The insertion loss S_{54}, S_{64}, S_{74}, and S_{84} was low at approximately 6.5 ~ 7.8 dB within the proposed bandwidth.

b. Analysis of Phase and Phase Difference

The phase and phase difference of the proposed 4 × 4 Butler matrix were analyzed. The results of the analysis for input port 1 are shown in Fig. 3-18 and Fig. 3-19.

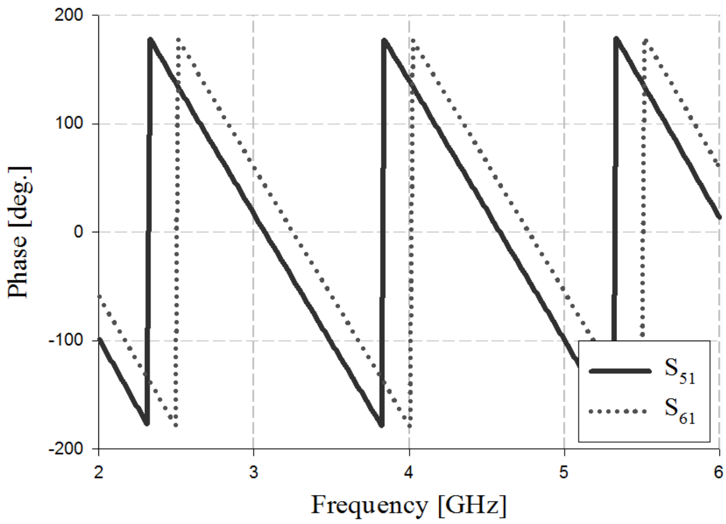

(a)

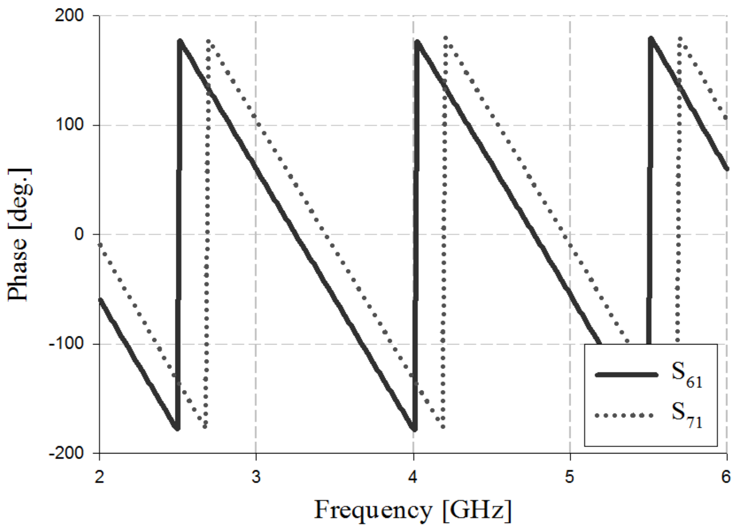

(b)

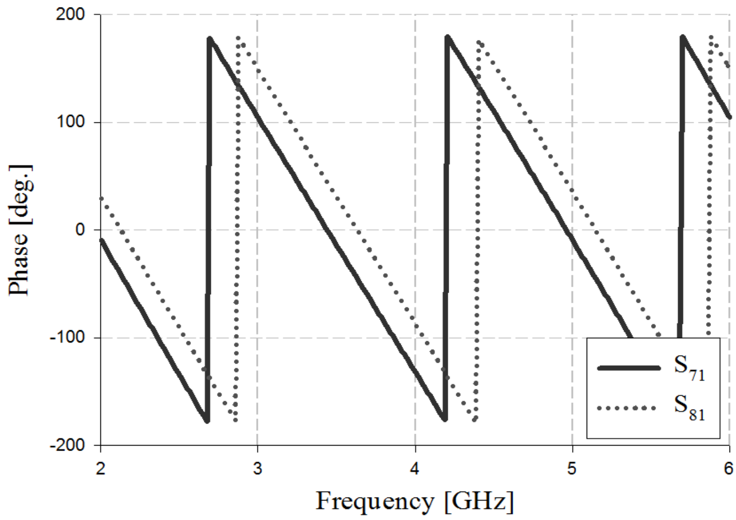

(c)

Fig. 3-19. Simulation analysis of phase for input port 1,

(a) Phase of S_{51} and S_{61}, (b) Phase of S_{61} and S_{71}, (c) Phase of S_{71} and S_{81}

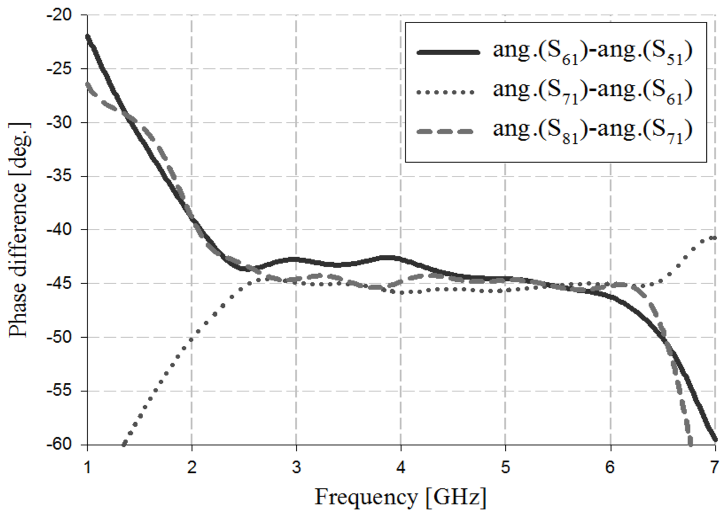

Fig. 3-20. Simulation analysis of phase difference for input port 1

The simulation results in Fig. 3-19 show that in the 3 ㎓ band, the phase is 17° and 59° in S_{51} and S_{61}; 59° and 103° in S_{61} and S_{71}; and 103° and 148° in S_{71} and S_{81}, respectively. In the 4 ㎓ band, the phase is 139° and -177° in S_{51} and S_{61}; -177° and -133° in S_{61} and S_{71}; and -133° and -88° in S_{71} and S_{81}, respectively. In the 5 ㎓ band, the phase is -100° and -56° in S_{51} and S_{61}; -56° and -10° in S_{61} and S_{71}; and -10° and -34° in S_{71} and S_{81}, respectively.

The simulation results in Fig. 3-20 show that the phase difference in the 3 ㎓, 4 ㎓, and 5 ㎓ band are -45° ± 3°, -45° ± 3°, and -45° ± 1°, respectively.

The results of the analysis for input port 2 are shown in Fig. 3-21 and Fig. 3-22.

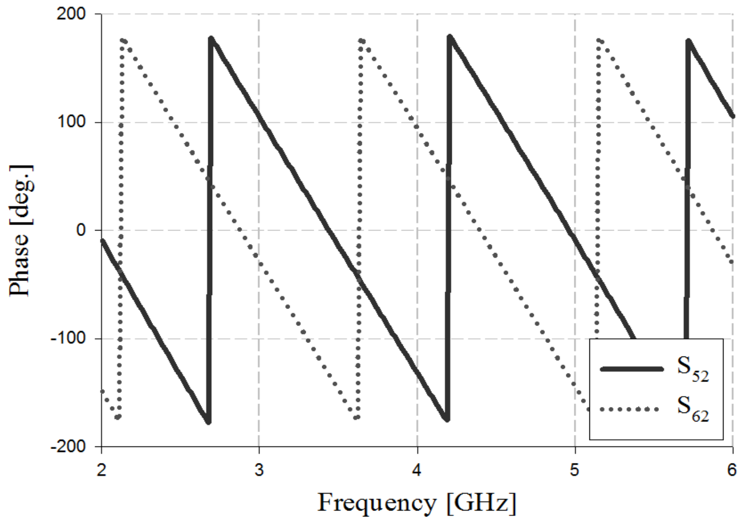

(a)

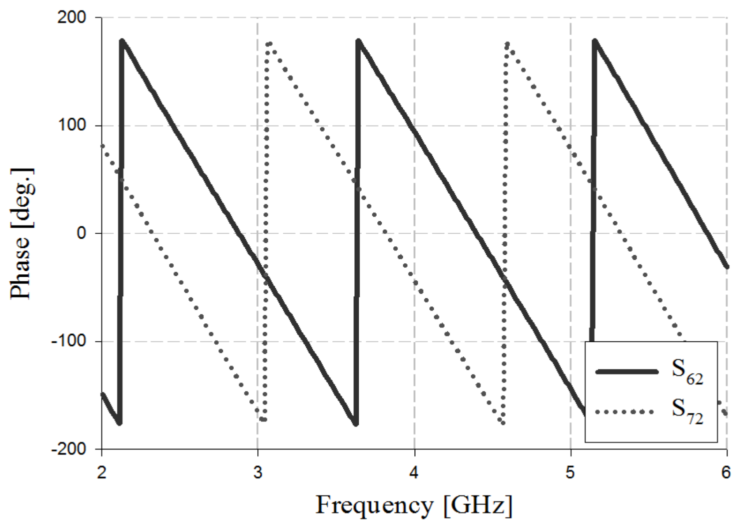

(b)

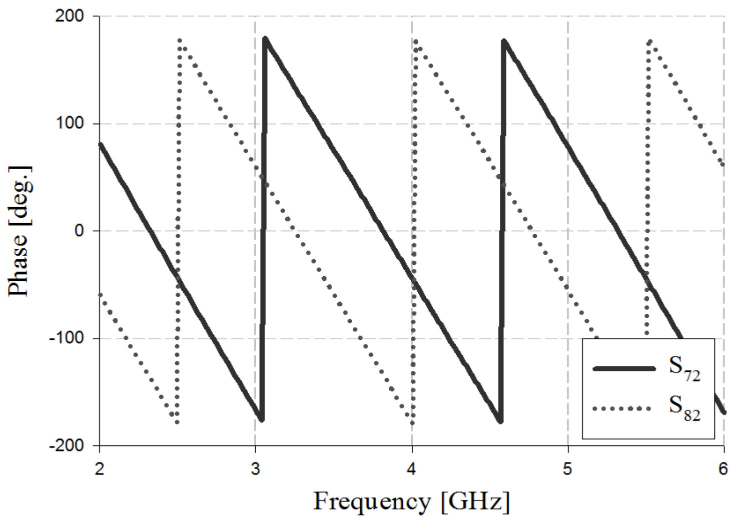

(c)

Fig. 3-21. Simulation analysis of phase for input port 2,

(a) Phase of S_{52} and S_{62}, (b) Phase of S_{62} and S_{72}, (c) Phase of S_{72} and S_{82}

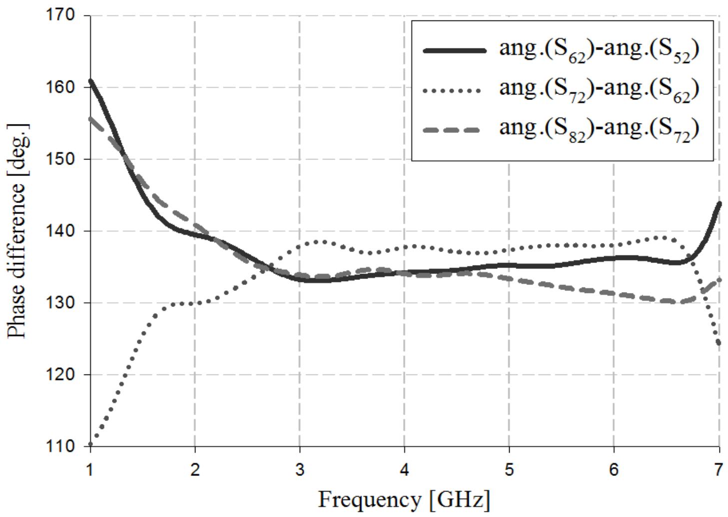

Fig. 3-22. Simulation analysis of phase difference for input port 2

The simulation results in Fig. 3-21 show that in the 3 ㎓ band, the phase is 103° and -29° in S_{52} and S_{62}; -29° and -167° in S_{62} and S_{72}; and -167° and 58° in S_{72} and S_{82}, respectively. In the 4 ㎓ band, the phase is -133° and 92° in S_{52} and S_{62}; 92° and -44° in S_{62} and S_{72}; and -44° and -178° in S_{72} and S_{82}, respectively. In the 5 ㎓ band, the phase is -10° and -145° in S_{52} and S_{62}; -145° and 76° in S_{62} and S_{72}; and 76° and -56° in S_{72} and S_{82}, respectively.

The simulation results in Fig. 3-22 show that the phase difference in the 3 ㎓, 4 ㎓, and 5 ㎓ band are 135° ± 2°, 135° ± 2°, and 135° ± 1°, respectively.

The results of the analysis for input port 3 are shown in Fig. 3-23 and Fig. 3-24.

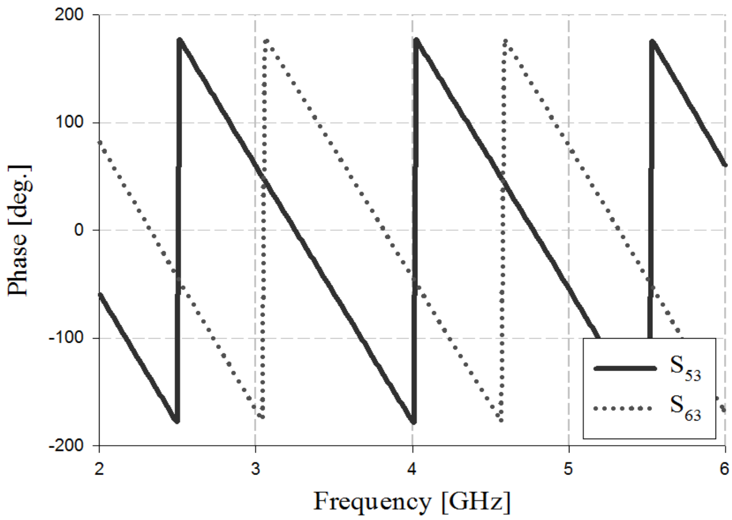

(a)

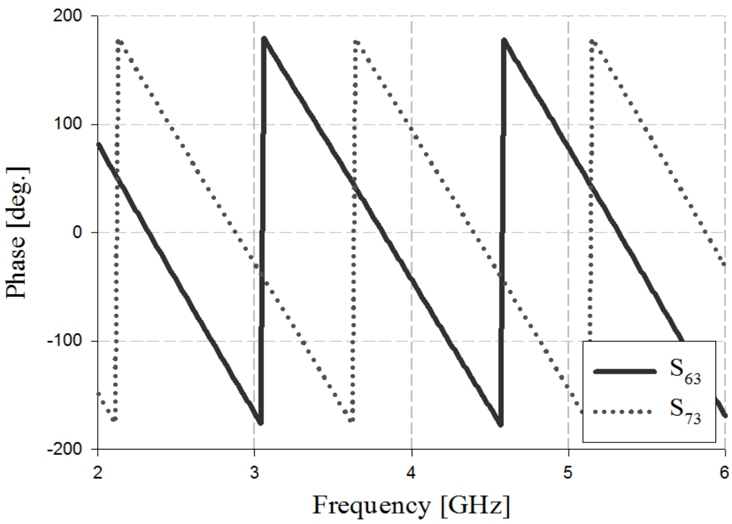

(b)

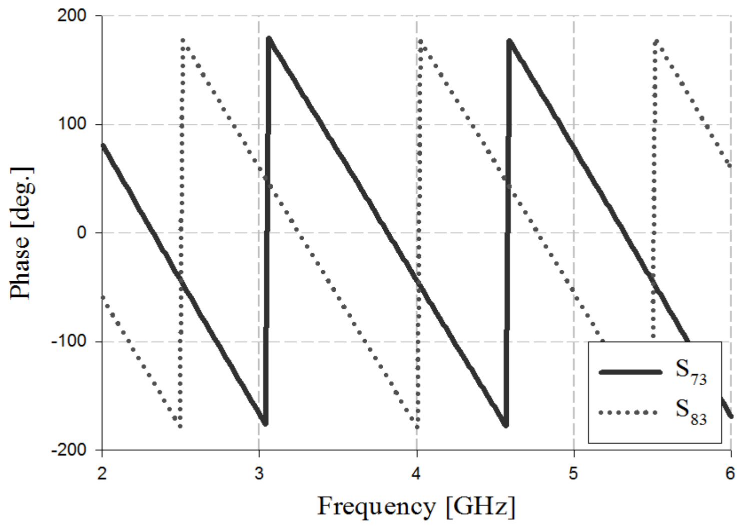

(c)

Fig. 3-23. Simulation analysis of phase for input port 3,

(a) Phase of S_{53} and S_{63}, (b) Phase of S_{63} and S_{73}, (c) Phase of S_{73} and S_{83}

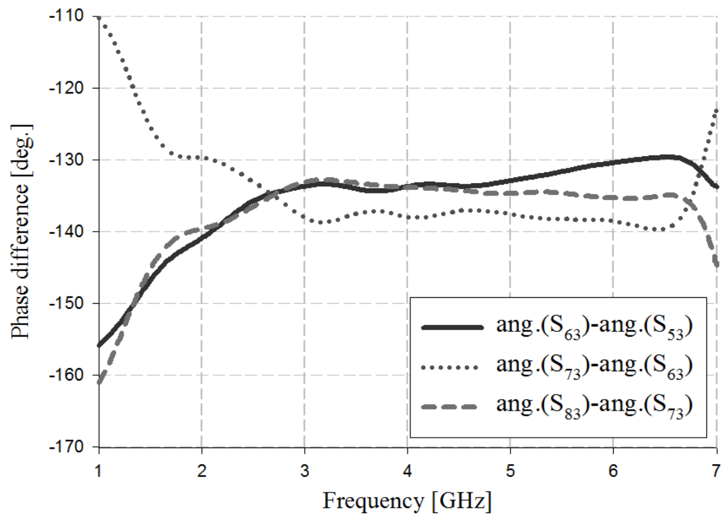

Fig. 3-24. Simulation analysis of phase difference for input port 3

The simulation results in Fig. 3-23 show that in the 3 ㎓ band, the phase is 58° and -167° in S_{53} and S_{63}; -167° and -29° in S_{63} and S_{73}; and -29° and 103° in S_{73} and S_{83}, respectively. In the 4 ㎓ band, the phase is -170° and -44° in S_{53} and S_{63}; -44° and 93° in S_{63} and S_{73}; and 93° and -132° in S_{73} and S_{83}, respectively. In the 5 ㎓ band, the phase is -54° and 78° in S_{53} and S_{63}; 78° and -143° in S_{63} and S_{73}; and -143° and -9° in S_{73} and S_{83}, respectively.

The simulation results in Fig. 3-24 show that the phase difference in the 3 ㎓, 4 ㎓, and 5 ㎓ band are -135° ± 3°, -135° ± 2°, and -135° ± 2°, respectively.

The results of the analysis for input port 4 are shown in Fig. 3-25 and Fig. 3-26.

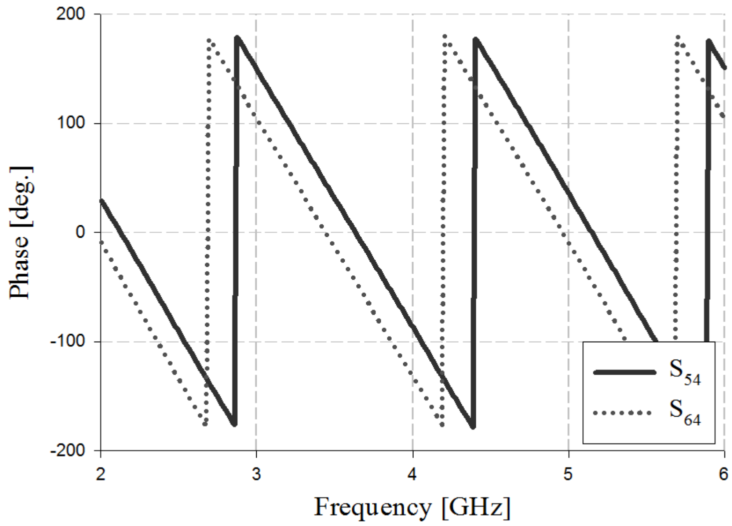

(a)

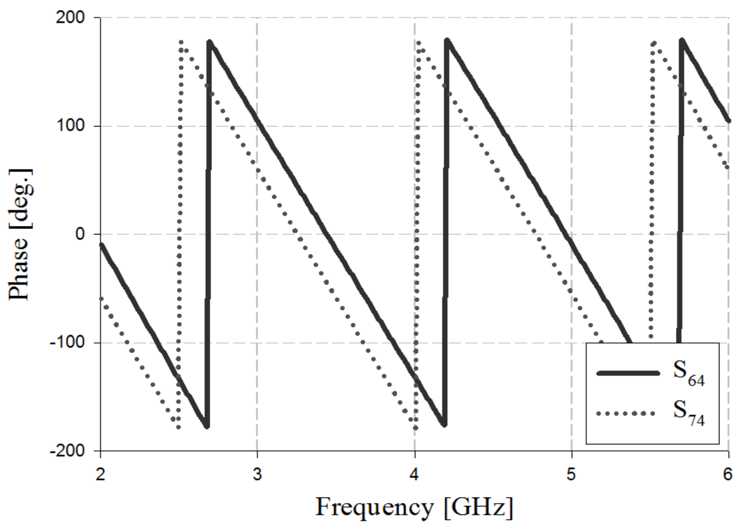

(b)

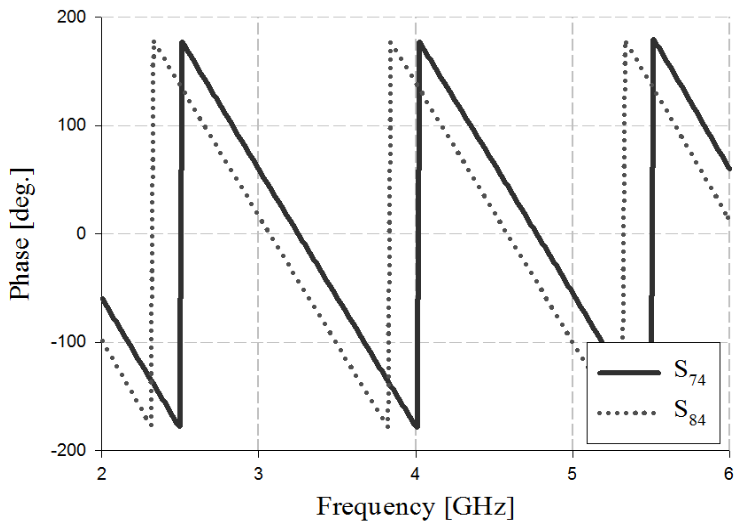

(c)

Fig. 3-25. Simulation analysis of phase for input port 4,

(a) Phase of S_{54} and S_{64}, (b) Phase of S_{64} and S_{74}, (c) Phase of S_{74} and S_{84}

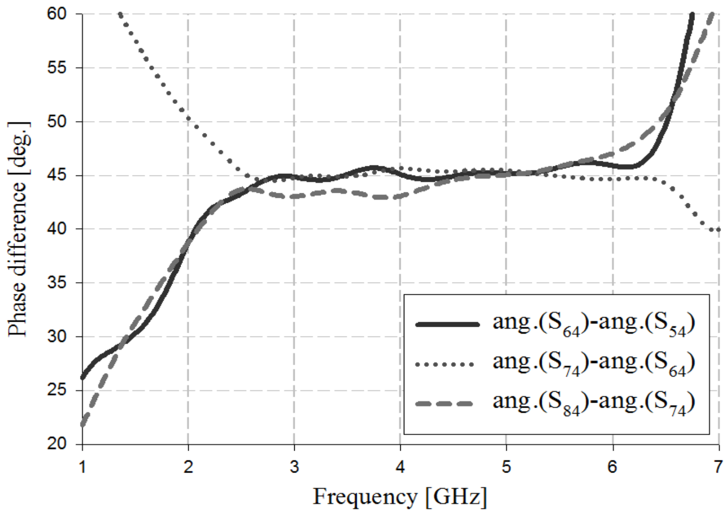

Fig. 3-26. Simulation analysis of phase difference for input port 4

The simulation results in Fig. 3-25 show that in the 3 ㎓ band, the phase is 148° and 103° in S_{54} and S_{64}; 103° and 58° in S_{64} and S_{74}; and 58° and 15° in S_{74} and S_{84}, respectively. In the 4 ㎓ band, the phase is -87° and -132° in S_{54} and S_{64}; -132° and -177° in S_{64} and S_{74}; and -177° and 139° in S_{74} and S_{84}, respectively. In the 5 ㎓ band, the phase is 36° and -9° in S_{54} and S_{64}; -9° and -54° in S_{64} and S_{74}; and -54° and -99° in S_{74} and S_{84}, respectively.

The simulation results in Fig. 3-26 show that the phase difference in the 3 ㎓, 4 ㎓, and 5 ㎓ band are 45° ± 2°, 45° ± 2°, and 45° ± 0°, respectively.

The simulation results for the overall analysis of the proposed 4 × 4 Butler matrix are listed in Table 3-7.

Table 3-7. Overall analysis of the proposed 4 × 4 Butler matrix

Input port \ Output port		Phase [deg.]				Phase difference [deg.]		
		P_5	P_6	P_7	P_8	S_{51}-S_{61}	S_{61}-S_{71}	S_{71}-S_{81}
Port 1	3 ㎓	17	59	103	148	-42	-44	-45
	4 ㎓	139	-177	-133	-88	-44	-44	-45
	5 ㎓	-100	-56	-10	34	-44	-46	-44
Port 2	3 ㎓	103	-29	-167	58	132	138	135
	4 ㎓	-133	92	-44	-178	135	136	134
	5 ㎓	-10	-147	76	-56	135	138	132
Port 3	3 ㎓	58	-167	-29	103	-135	-138	-132
	4 ㎓	-170	-44	93	-132	-126	-137	-135
	5 ㎓	-54	78	-143	-9	-132	-139	-134
Port 4	3 ㎓	148	103	58	15	45	45	43
	4 ㎓	-87	-132	-177	139	45	45	44
	5 ㎓	36	-9	-54	-99	45	45	45

The simulation results in Table 3-7 show that input ports 1～4 generate the phase difference at regular intervals in each output port, and the output phase is fed to the array antenna.

3.3 Implementation of Beamforming Antenna

The proposed beamforming antenna consists of the linear array, and a signal is fed into the input ports of each antenna. When configuring arrays, the distance between each antenna is a very important parameter that determines the direction and gain of the main beam. Grating lobes are generated when the distance between each antenna is larger than the wavelength. On the other hand, if the distance between each antenna is small, the side lobe level increases owing to the interference between antennas. Therefore, the distance d of the array antenna must satisfy the condition $\lambda/2 < d < \lambda$[58][59].

3.3.1 Analysis of 1 × 4 Linear Array Antenna

The distance of the array antenna was designed to be 30 ㎜ for ease of fabrication, and is shown in Fig. 3-27.

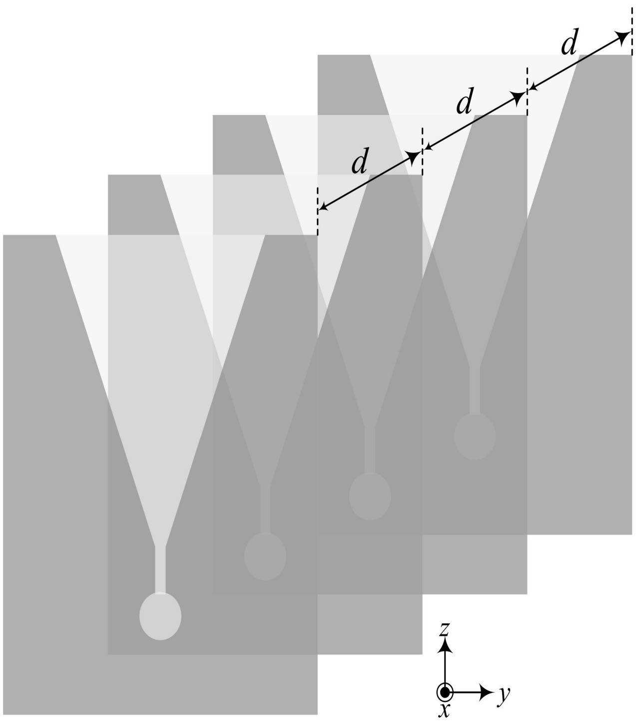

Fig. 3-27. Configuration of the proposed linear array antenna

Feed signals of the same size are fed to each antenna and analyzed using the HFSS simulation tool. The simulation results are listed in Table 3-8.

Table 3-8. Radiation patterns from simulation analysis of the proposed tapered-slot antenna

Frequency	**Simulation results**
3 GHz	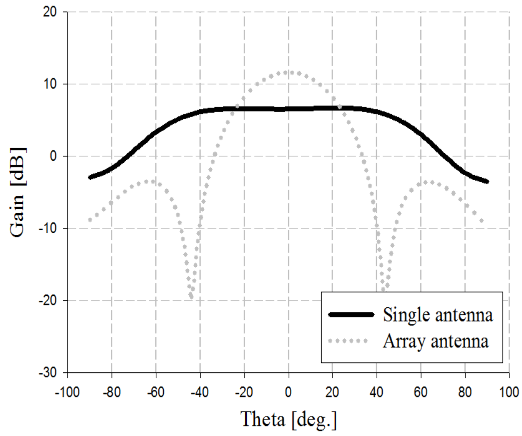
4 GHz	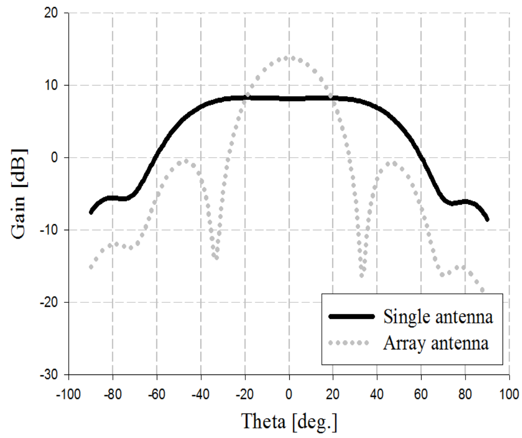
5 GHz	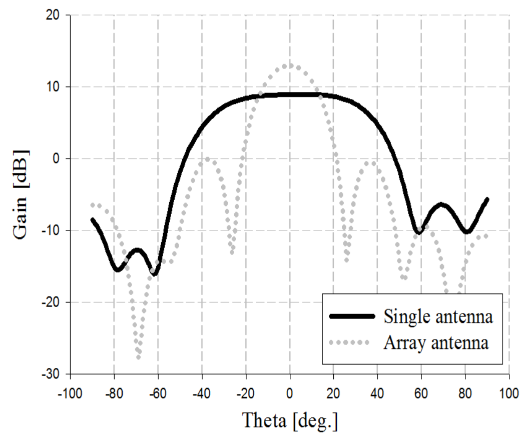

The simulation results in Table 3-8 show that the gain of the single antenna and 1 × 4 array antenna are 6.70 and 11.62 dBi in the 3 GHz band, 8.36 and 13.78 dBi in the 4 GHz band, and 8.97 and 12.98 dBi in the 5 GHz band, respectively. In other words, when the antennas are arranged, gain increases and beamwidth narrows.

3.3.2 Analysis of Beamforming Antenna

The proposed beamforming antenna was designed by connecting the 1 × 4 array antenna and 4 × 4 Butler matrix. As shown in Table 3-5, the proposed 4 × 4 butler matrix has constant phase difference, and the phase difference is fed into the input ports of the 1 × 4 array antenna to control the four beams. The simulated configuration of the beamforming antenna is shown in Fig. 3-28.

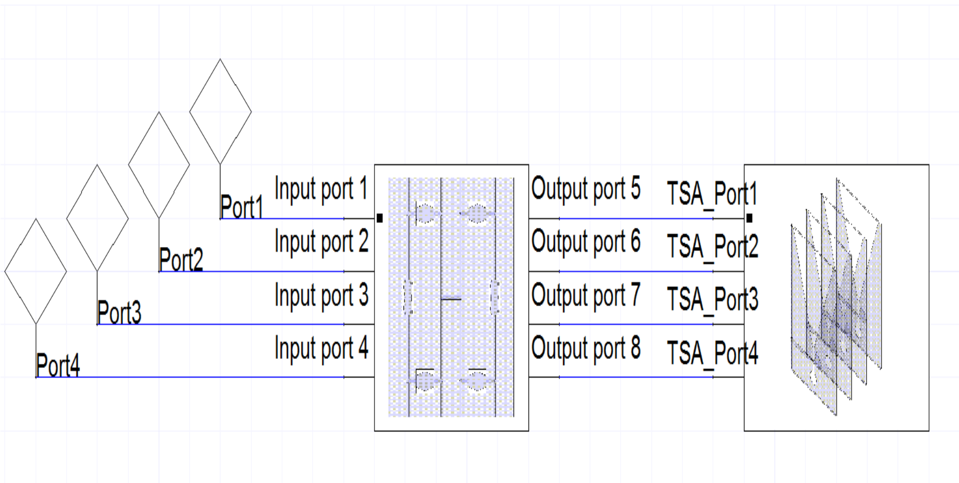

Fig. 3-28. Simulation configuration of the proposed beamforming antenna

As shown in Fig. 3-28, when the feed signal is fed into input port 1, the phase which has the phase difference of approximately -45° is generated and is fed into the input ports of each TSA. Furthermore, when the feed signal is fed into input port 2, the phase which has the phase difference of approximately 135° is generated and fed into the input ports of each TSA. Input ports 3 and 4 have the same operation because the symmetry structure. The results of the simulation analysis of the 3-D beam patterns of the proposed beamforming antenna are shown in Fig. 3-9.

Table 3-9. 3-D beam pattern of simulation analysis for the proposed tapered-slot antenna

Freq.	Simulation results		
	3 ㎓	4 ㎓	5 ㎓
3 Port	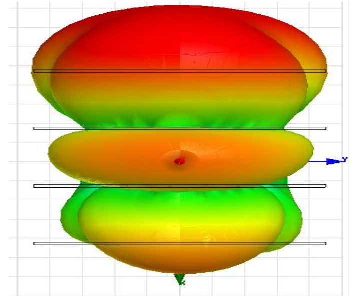	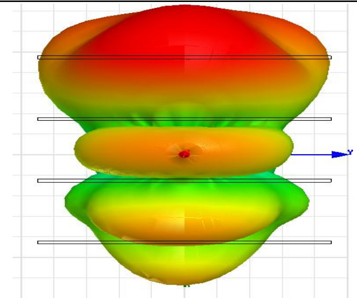	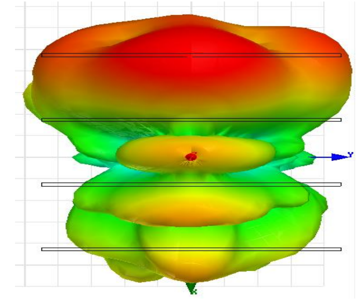
1 Port	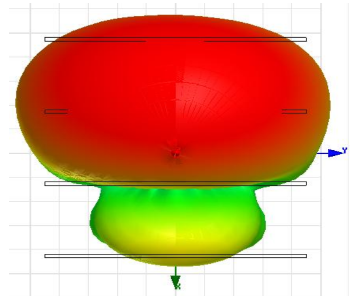	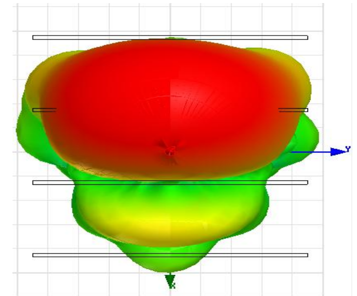	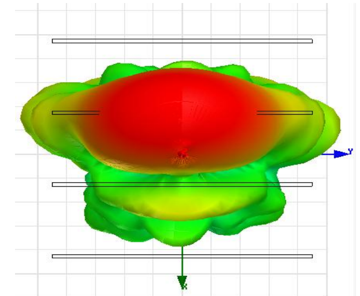
4 Port	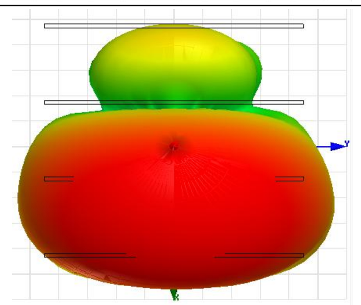	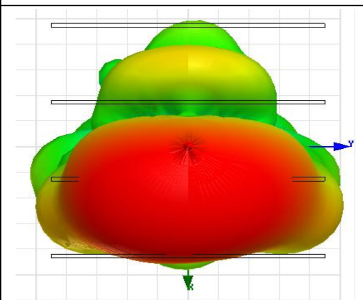	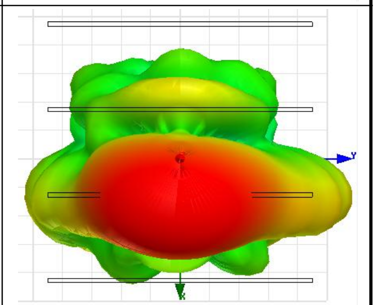
2 Port	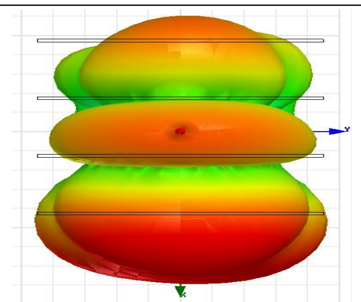	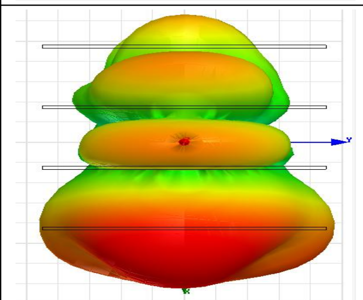	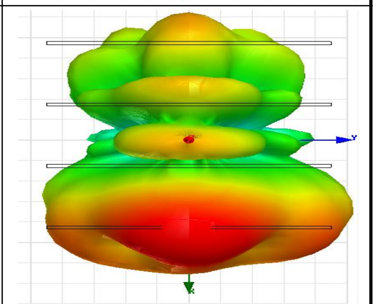

The simulation results in Table 3-9 show that the main beam of the antenna was formed in the four directions. Therefore, the proposed beamforming antenna can be scanned approximately +50° to −50° from the left side.

Ⅳ Fabrication and Measurement of Beamforming Antenna

4.1 Fabrication of UWB Antenna

4.1.1 Fabrication and Measurement of the Tapered-Slot Antenna

Based on the simulation results, the fabricated TSA is shown in Fig. 4-1.

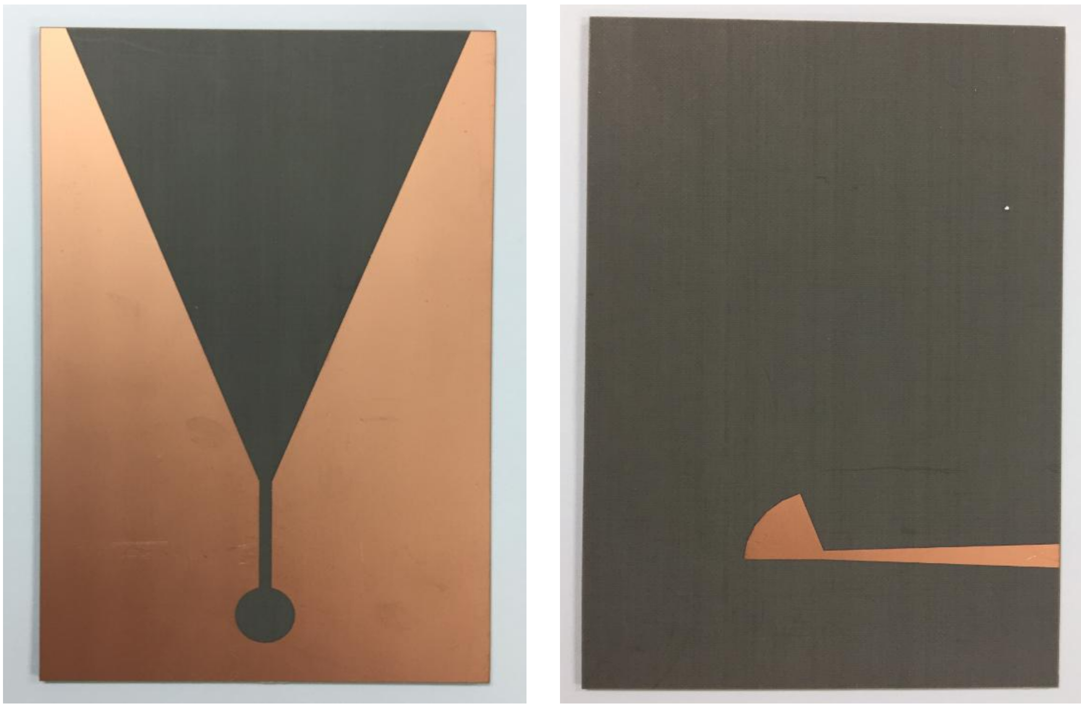

(a) (b)

Fig. 4-1. Photograph of the fabricated tapered-slot antenna, (a) Top layer, (b) Bottom layer

The proposed TSA was fabricated by etching process using the Taconic TLY substrate, which has a relative permittivity of 2.2, loss tangent of 0.0009, and thickness of 1.52 ㎜. The radiation element was placed on the top layer of the proposed TSA, and the transition feed was placed on the bottom layer.

4.1.2 Measurement Configuration of the Antenna

The fabricated TSA's return loss and VSWR were measured using a network analyzer (N5230A, Agilent Co.), and the measurement configuration is shown in Fig. 4-2.

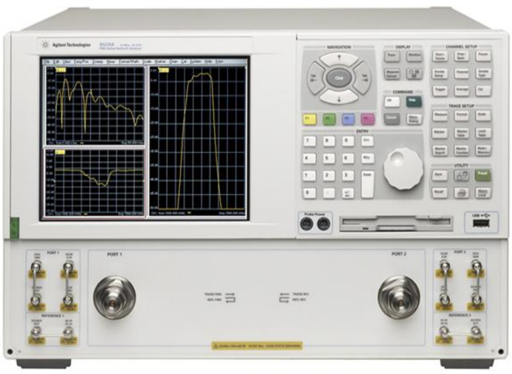

(a)

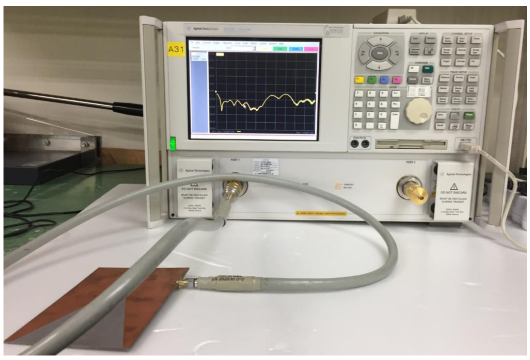

(b)

Fig. 4-2. Measurement configuration of the fabricated antenna using network analyzer, (a) Network analyzer (N5230A), (b) Measurement configuration

The radiation patterns of the fabricated TSA were measured using a far-field analysis system in an anechoic chamber room of Korea Daejon Techno Park Co.. The measurement configuration and equipment configuration are shown in Fig 4-3 and Table 4-1, respectively.

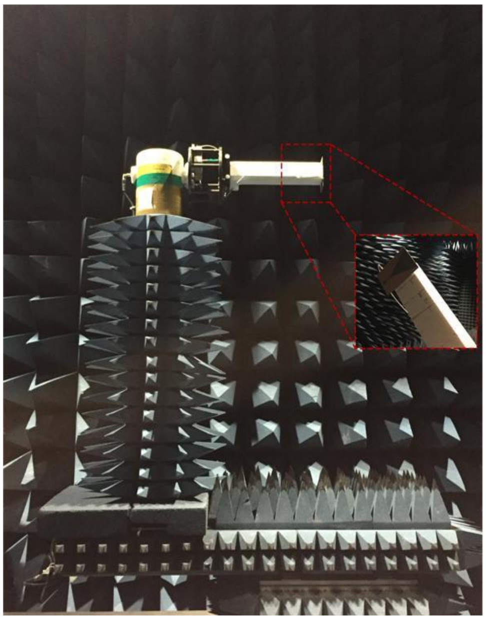

Fig. 4-3. Measurement configuration of the fabricated antenna

Table 4-1. Equipment configuration and performance

Chamber size	14 × 7 × 6.7 ㎥
Chamber type	Rectangular type
Measurement range	200 ㎒ ~ 20 ㎓
Measurement configuration	Far-field
Measurement parameter	Antenna pattern, Antenna gain
Major equipment	- Network analyzer E8362B(~20 ㎓) - L/O unit(Agilent) - RF control unit - E5515C(Communication set)

a. The Impedance Bandwidth and the Radiation Pattern Measurement of the Antenna

The impedance bandwidth measurement results of the fabricated TSA are shown in Fig. 4-4.

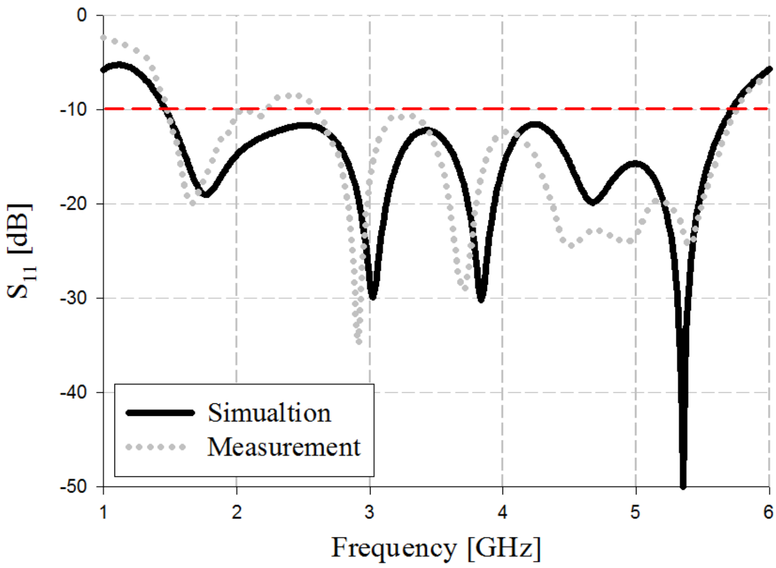

(a)

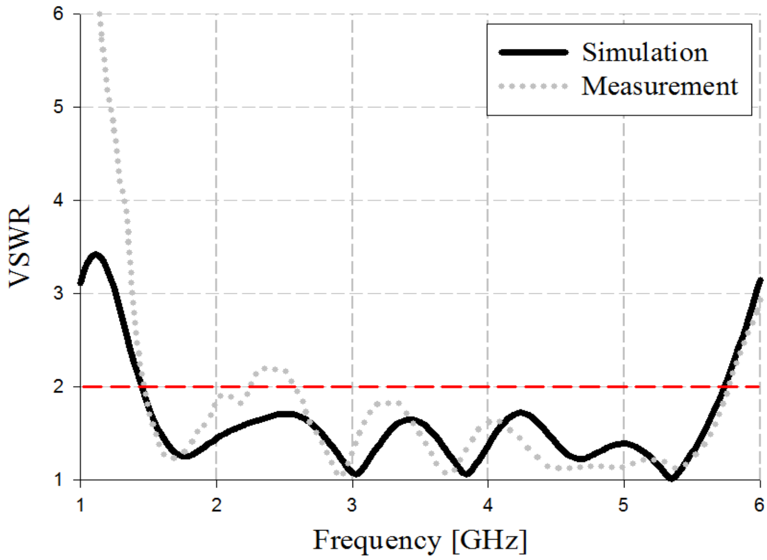

(b)

Fig. 4-4. Impedance bandwidth results using network analyzer for the fabricated antenna, (a) S_{11}, (b) VSWR

The results in Fig. 4-4 show that impedance bandwidth of the fabricated TSA achieved the wide bandwidth of 4.32 ㎓ by satisfying －10 ㏈ S_{11} and VSWR≤2 in the 1.46～5.78 ㎓ band.

The radiation patterns of the fabricated TSA were analyzed in the E-plane (y-z) and H-plane (x-z), as shown in Fig. 4-5.

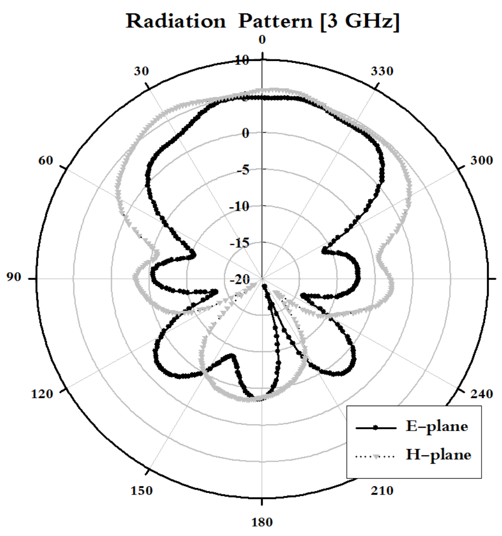

(a)

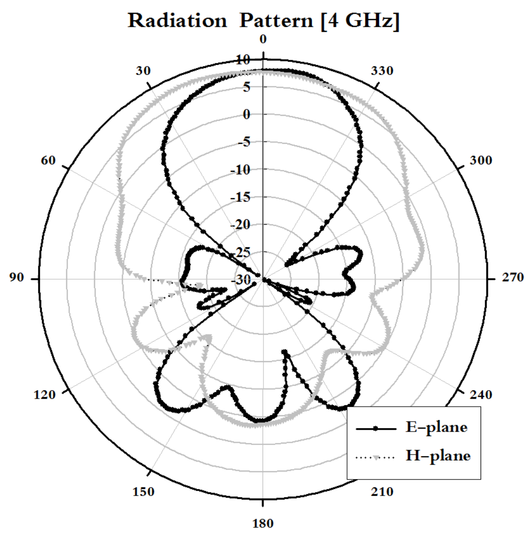

(b)

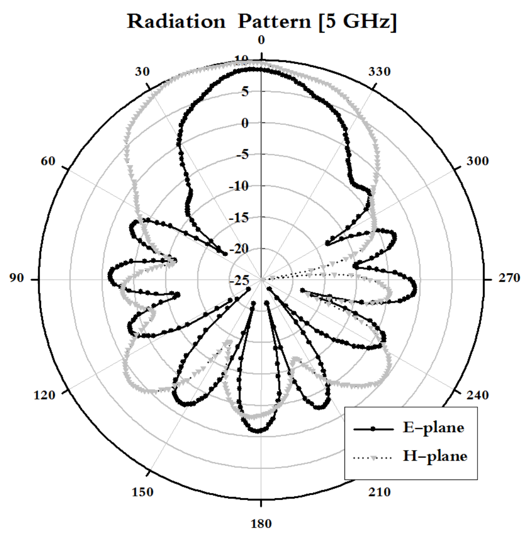

(c)

Fig. 4-5. Measurement analysis of the radiation patterns of the proposed antenna, (a) 3 ㎓ band, (b) 4 ㎓ band, (c) 5 ㎓ band

The results in Fig. 4-5 show that the E-plane and H-plane radiation patterns of the fabricated TSA had the directivity of an end-fire that increased the sensitivity for a certain direction. The results of the gain and 3 dB beamwidth measurements of the fabricated antenna are shown in Fig. 4-6 and Table 4-2, respectively.

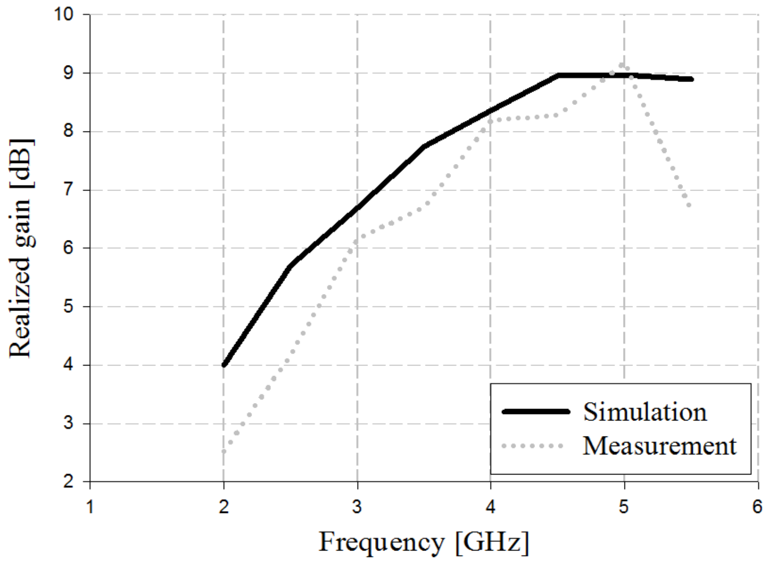

Fig. 4-6. Measurement analysis of the gain of the proposed antenna

Table 4-2. The measurement results of gain and 3 dB beamwidth of the proposed tapered-slot antenna

Frequency [GHz]	Gain [dBi]	3-dB beamwidth	
		E-plane	H-plane
3	6.17	72°	109°
4	8.19	40°	84°
5	9.18	29°	60°

The measurement results in Fig. 4-6 and Table 4-2 show that the gain of the fabricated TSA was 6.17, 8.19, and 9.18 dBi in the 3 ㎓, 4 ㎓, and 5 ㎓ band, respectively. Furthermore, the 3 dB beamwidth results for the E-plane and H-plane were 72° and 109° in the 3 ㎓ band, 40° and 84° in the 4 ㎓ band, and 29° and 60° in the 5 ㎓ band, respectively.

Comparisons of the simulation and measurement results of the fabricated TSA are shown in Table 4-3.

Table 4-3. Comparison of simulation and measurement results of the fabricated antenna

Parameters	Simulation result			Measurement result		
Impedance bandwidth	1.45 ~ 5.74 ㎓			1.46 ~ 5.78 ㎓		
Antenna gain	3 ㎓	6.70 dBi		3 ㎓	6.17 dBi	
	4 ㎓	8.36 dBi		4 ㎓	8.19 dBi	
	5 ㎓	8.97 dBi		5 ㎓	9.18 dBi	
Antenna beamwidth	3 ㎓	E-plane	70.45°	3 ㎓	E-plane	72°
		H-plane	117.00°		H-plane	109°
	4 ㎓	E-plane	58.03°	4 ㎓	E-plane	40°
		H-plane	96.38°		H-plane	84°
	5 ㎓	E-plane	36.48°	5 ㎓	E-plane	29°
		H-plane	72.25°		H-plane	60°

As shown in Table 4-3, the simulation and measurement results of the fabricated TSA showed good agreement.

4.2 Fabrication of Butler Matrix

4.2.1 Fabrication and Measurement of the 4 × 4 Butler Matrix

Based on the simulation results, the fabricated 4 × 4 Butler matrix is shown in Fig. 4-1.

Fig. 4-7. Photograph of fabricated 4 × 4 Butler matrix

The proposed 4 × 4 Butler matrix was fabricated by etching process using TRF-45 substrate, which has a relative permittivity of 4.5, loss tangent of 0.0035, and thickness of 0.61 ㎜. Furthermore, it was fabricated on the two laminated substrates, and has four input and output ports.

4.2.2 Measurement Configuration of the 4 × 4 Butler Matrix

The fabricated 4 × 4 Butler matrix was measured the return loss, isolation, and insertion loss using a network analyzer (N5230A, Agilent Co.), and the measurement configuration is shown in Fig. 4-8.

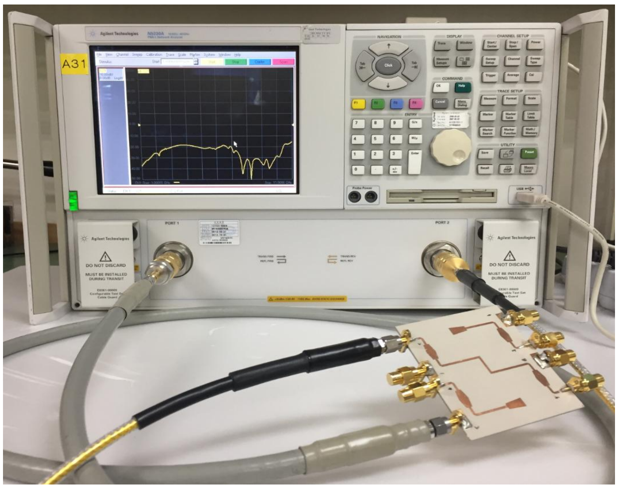

Fig. 4-8. Measurement of the characteristics of the fabricated 4 × 4 Butler matrix using network analyzer

a. Measurement of S-Parameters

The results of measurement of S-parameters for input port 1 of the fabricated 4 × 4 Butler matrix are shown in Fig. 4-9.

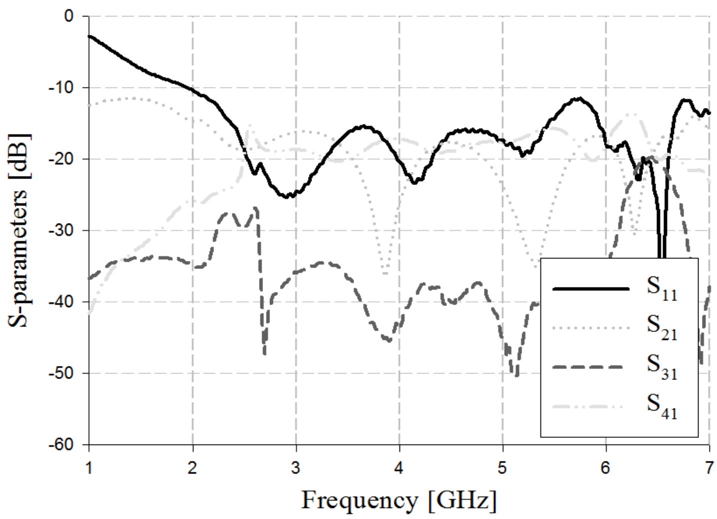

(a)

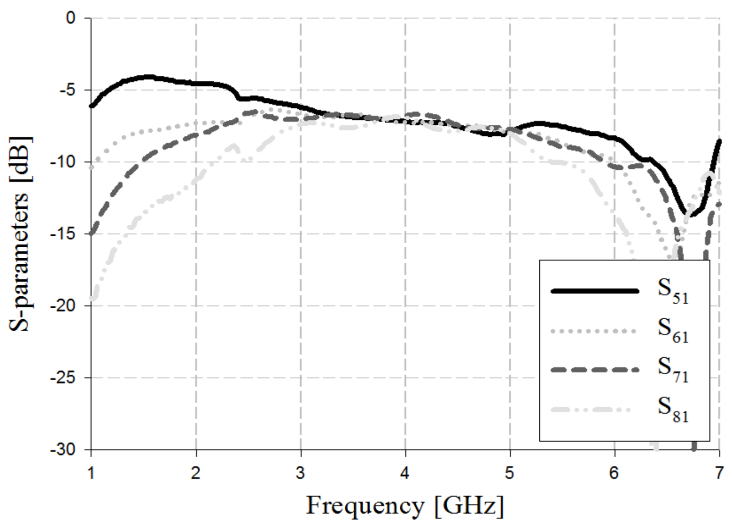

(b)

Fig. 4-9. Measurement analysis of S-parameters for input port 1,

(a) Return loss & isolation, (b) Insertion loss

The results in Fig. 4-9 show that the return loss S_{11} and isolation S_{21}, S_{31}, and S_{41} were less than -15 ㏈ in the 3 ~ 5 ㎓ band. The insertion loss S_{51}, S_{61}, S_{71}, and S_{81} had low insertion loss of approximately 6.2 ~ 6.8 ㏈ within the proposed bandwidth.

The results of measurement of S-parameters for input port 2 of the fabricated 4 × 4 Butler matrix are shown in Fig. 4-10.

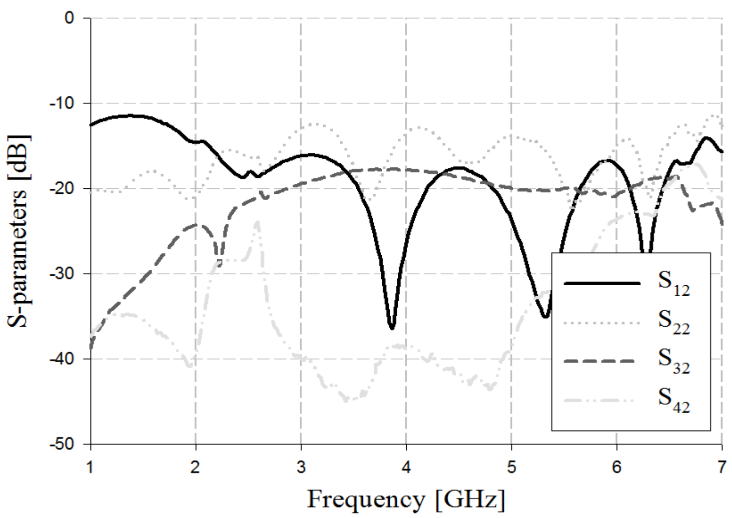

(a)

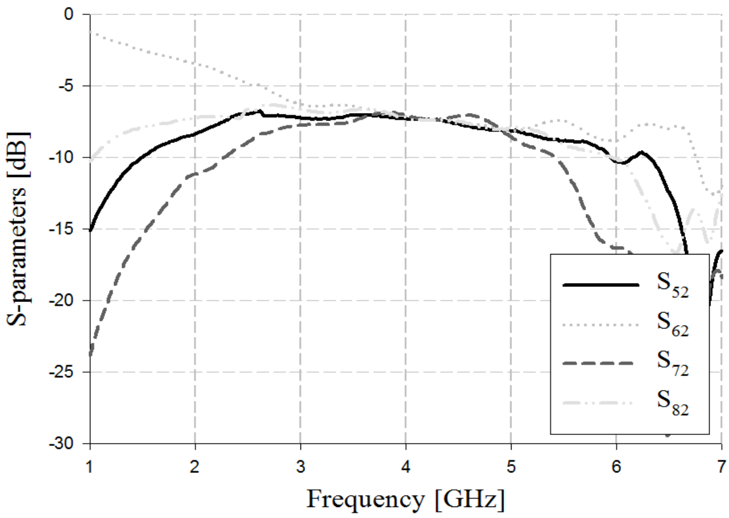

(b)

Fig. 4-10. Measurement analysis of S-parameters for input port 2,

(a) Return loss & isolation, (b) Insertion loss

The results in Fig. 4-10 show that the return loss S_{22} and isolation S_{12}, S_{32}, and S_{42} were less than -10 ㏈ in the 3 ~ 5 ㎓ band. The insertion loss S_{52}, S_{62}, S_{72}, and S_{82} had low insertion loss of approximately 6.1 ~ 6.7 ㏈ within the proposed bandwidth.

The results of measurement of S-parameters for input port 3 of the fabricated 4 × 4 Butler matrix are shown in Fig. 4-11.

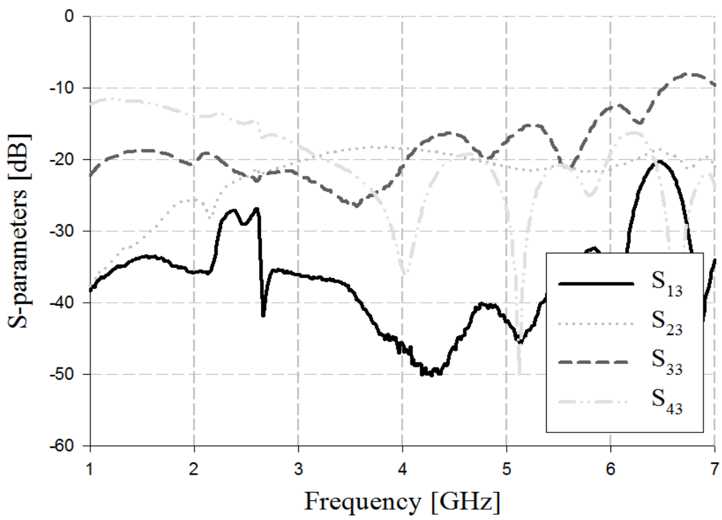

(a)

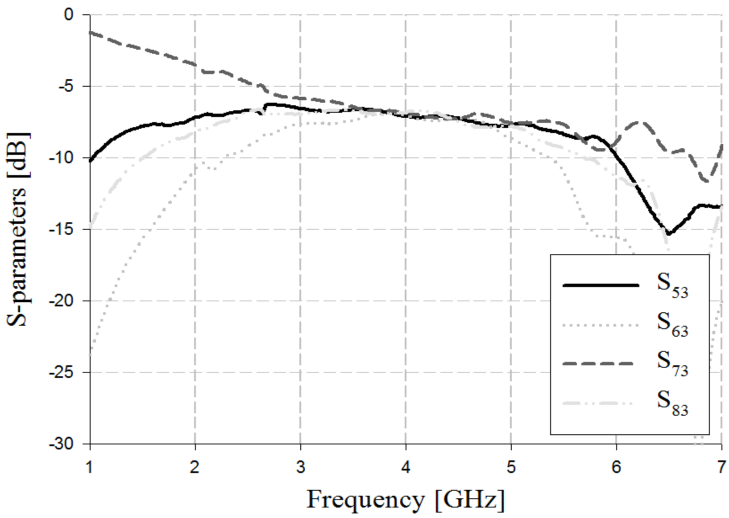

(b)

Fig. 4-11. Measurement analysis of S-parameters for input port 3,

(a) Return loss & isolation, (b) Insertion loss

The results in Fig. 4-11 show that the return loss S_{33} and isolation S_{13}, S_{23}, and S_{43} were less than -15 ㏈ in the 3 ~ 5 ㎓ band. The insertion loss S_{53}, S_{63}, S_{73}, and S_{83} had low insertion loss of approximately 5.8 ~ 8 ㏈ within the proposed bandwidth.

The results of measurement of S-parameters for input port 3 of the fabricated 4 × 4 Butler matrix are shown in Fig. 4-12.

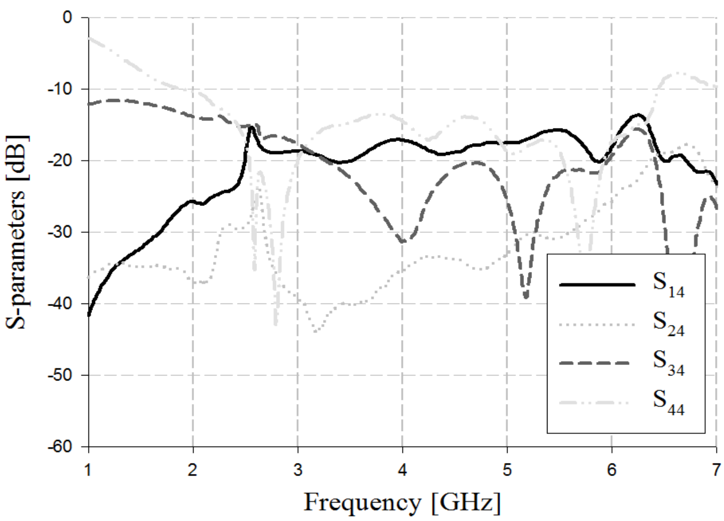

(a)

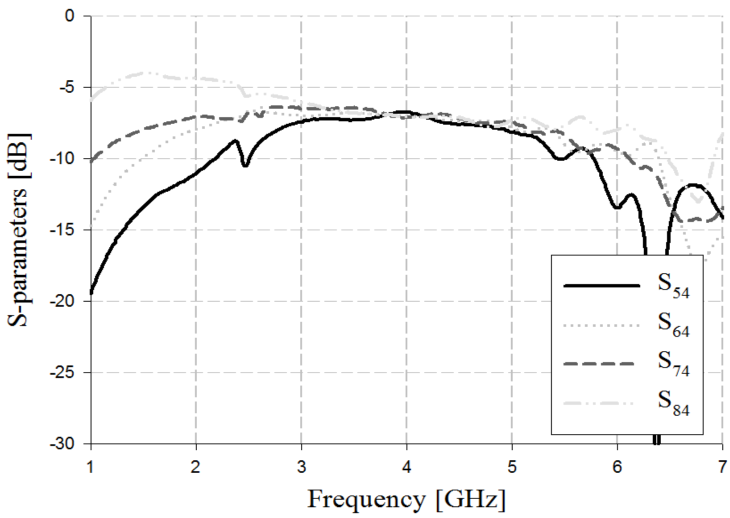

(b)

Fig. 4-12. Measurement analysis of S-parameters for input port 4, (a) Return loss & isolation, (b) Insertion loss

The results in Fig. 4-12 show that the return loss S_{44} and isolation S_{14}, S_{24}, and S_{34} were less than -13 ㏈ in the 3 ~ 5 ㎓ band. The insertion loss S_{54}, S_{64}, S_{74}, and S_{84} had low insertion loss of approximately 6.08 ~ 8.13 ㏈ within the proposed bandwidth.

b. Measurement of Phase and Phase Difference

The phase and phase difference of the fabricated 4 × 4 Butler matrix were measured. The measurement results of phase and phase difference for input port 1 are shown in Fig. 4-13 and Fig. 4-14.

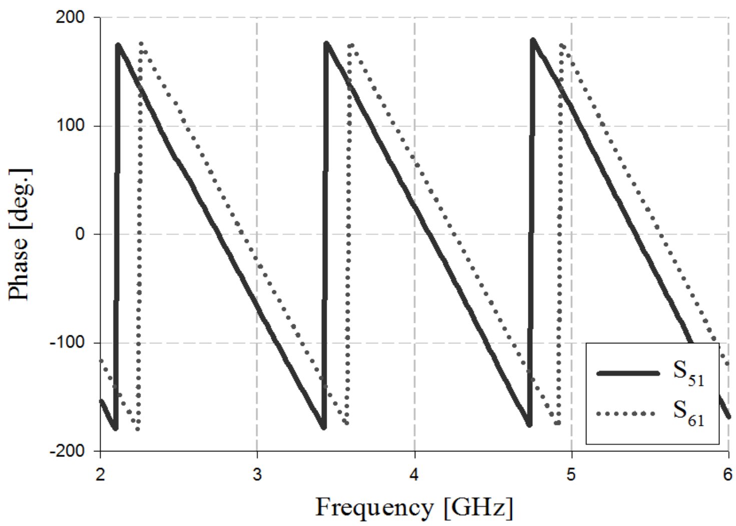

(a)

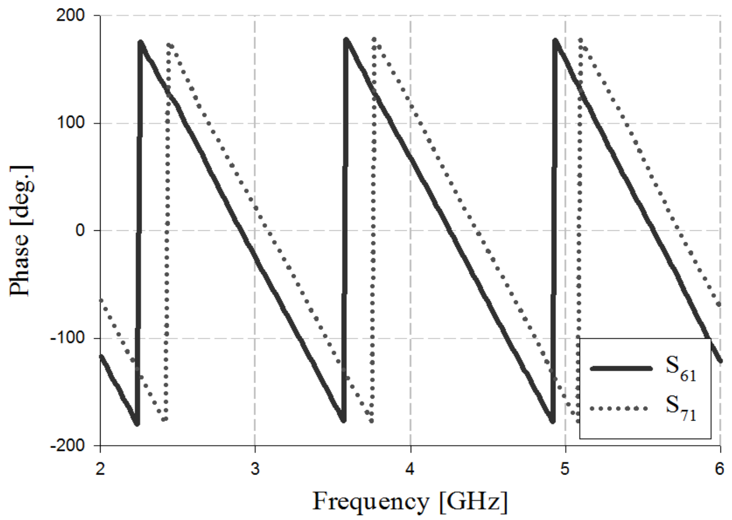

(b)

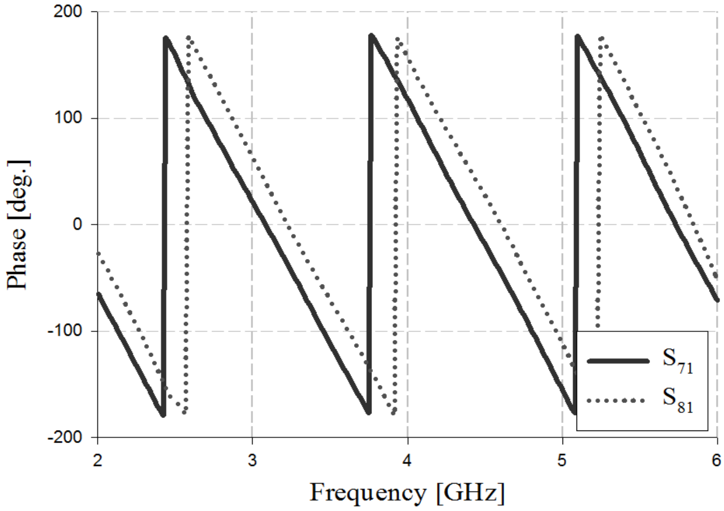

(c)

Fig. 4-13. Measurement analysis of phase for input port 1,

(a) Phase of S_{51} and S_{61}, (b) Phase of S_{61} and S_{71}, (c) Phase of S_{71} and S_{81}

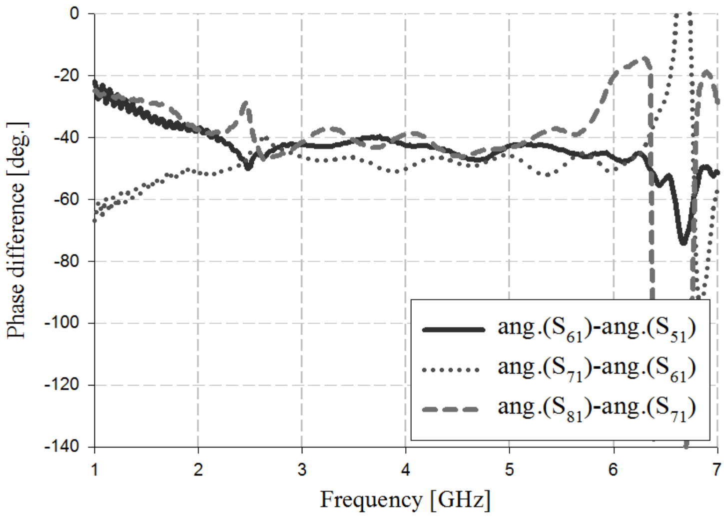

Fig. 4-14. Measurement analysis of phase difference for input port 1

The results in Fig. 4-13 show that in the 3 ㎓ band, the phase is -68° and -25° in S_{51} and S_{61}; -25° and 20° in S_{61} and S_{71}; and 20° and 62° in S_{71} and S_{81}, respectively. In the 4 ㎓ band, the phase is 23° and 66° in S_{51} and S_{61}; 66° and 116° in S_{61} and S_{71}; and 116° and 155° in S_{71} and S_{81}, respectively. In the 5 ㎓ band, that phase is 115° and 157° in S_{51} and S_{61}; 157° and -156° in S_{61} and S_{71}; and -156° and -113° in S_{71} and S_{81}, respectively.

The measurement results in Fig. 4-14 show that the phase difference in the 3 ㎓, 4 ㎓, and 5 ㎓ band are -45° ± 4°, -45° ± 7°, and -45° ± 3°, respectively.

The measurement results of phase and phase difference for input port 2 are shown in Fig. 4-15 and Fig. 4-16.

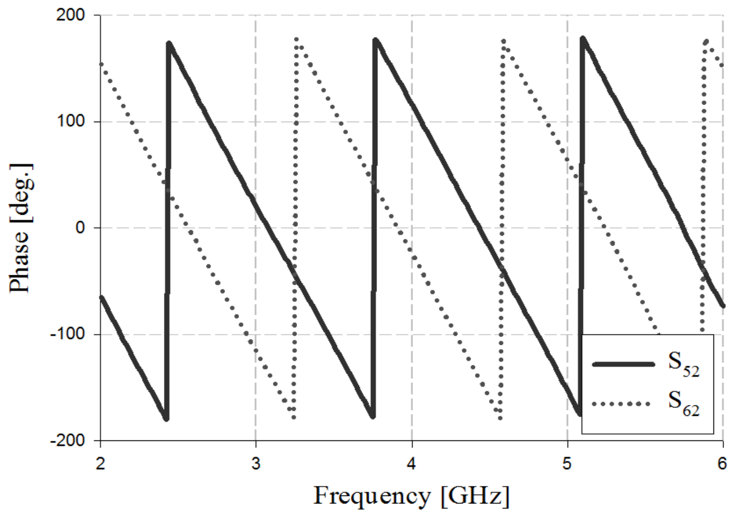

(a)

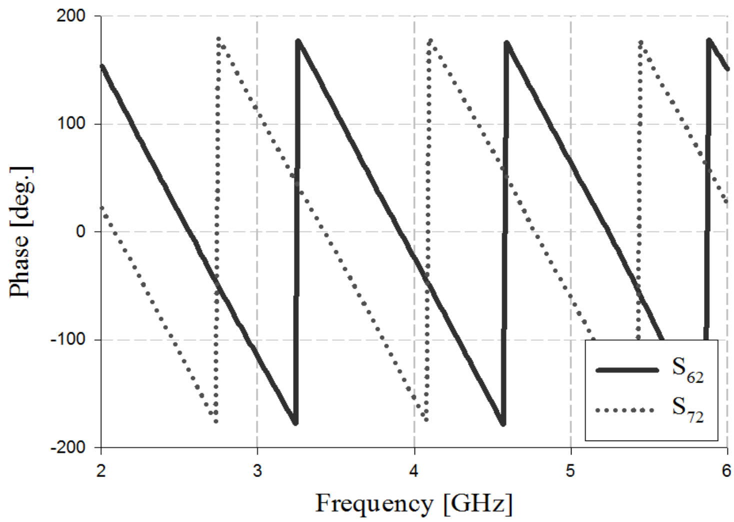

(b)

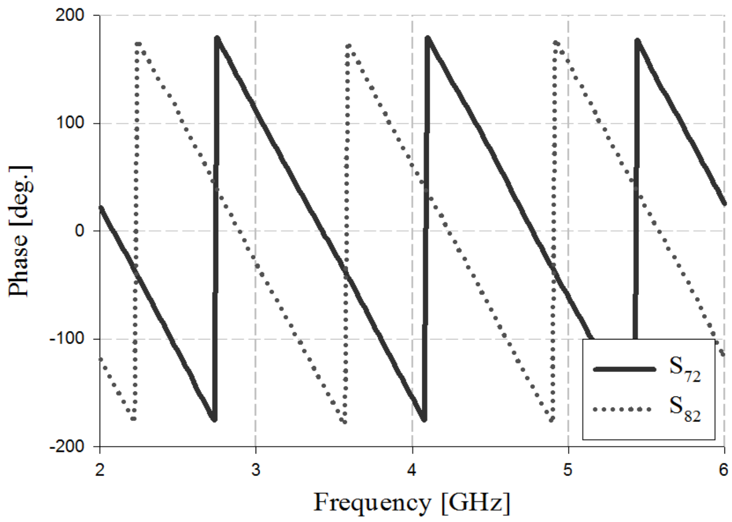

(c)

Fig. 4-15. Measurement analysis of phase for input port 2,

(a) Phase of S_{52} and S_{62}, (b) Phase of S_{62} and S_{72}, (c) Phase of S_{72} and S_{82}

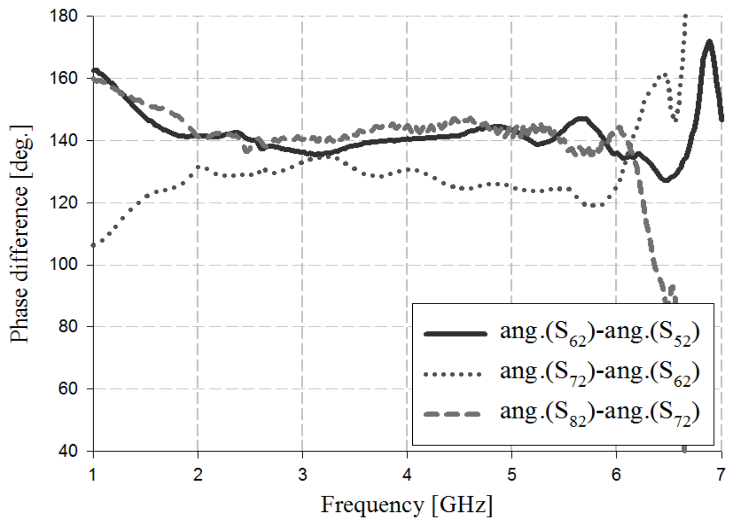

Fig. 4-16. Measurement analysis of phase difference for input port 2

The results in Fig. 4-15 show that in the 3 ㎓ band, the phase is 19° and -116° in S_{52} and S_{62}; -116° and 109° in S_{62} and S_{72}; and 109° and -30° in S_{72} and S_{82}, respectively. In the 4 ㎓ band, the phase is 115° and -25° in S_{52} and S_{62}; -25° and -156° in S_{62} and S_{72}; and -156° and 58° in S_{72} and S_{82}, respectively. In the 5 ㎓ band, that phase is -153° and 63° in S_{52} and S_{62}; 63° and -62° in S_{62} and S_{72}; and -62° and 156° in S_{72} and S_{82}, respectively.

The measurement results in Fig. 4-16 show that the phase difference in the 3 ㎓, 4 ㎓, and 5 ㎓ band are 135° ± 5°, 135° ± 9°, and 135° ± 10°, respectively.

The measurement results of phase and phase difference for input port 3 are shown in Fig. 4-17 and Fig. 4-18.

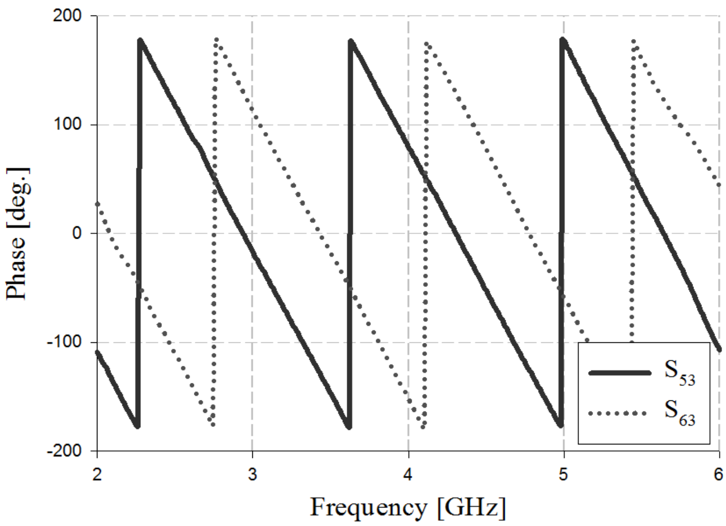

(a)

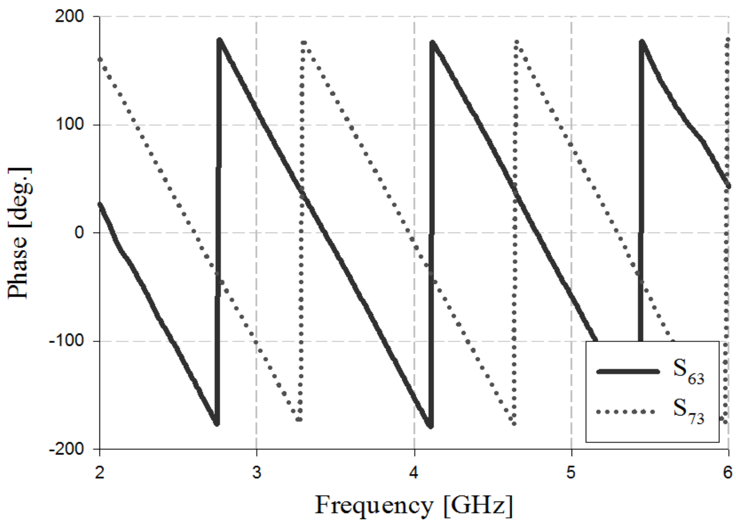

(b)

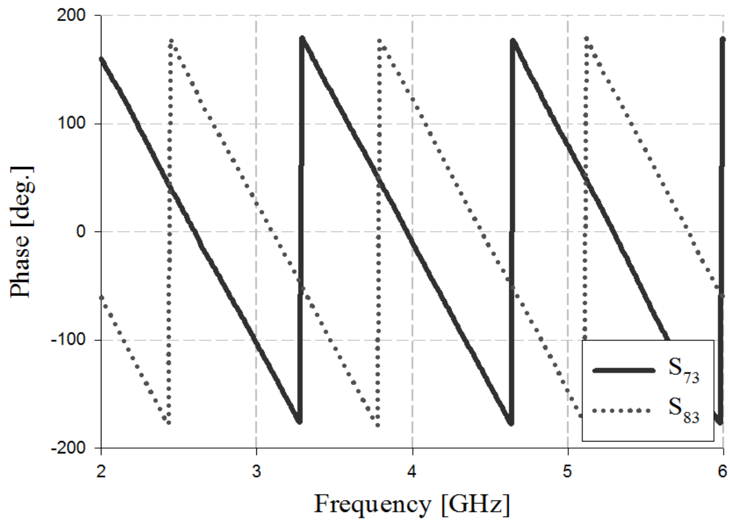

(c)

Fig. 4-17. Measurement analysis of phase for input port 3,

(a) Phase of S_{53} and S_{63}, (b) Phase of S_{63} and S_{73}, (c) Phase of S_{73} and S_{83}

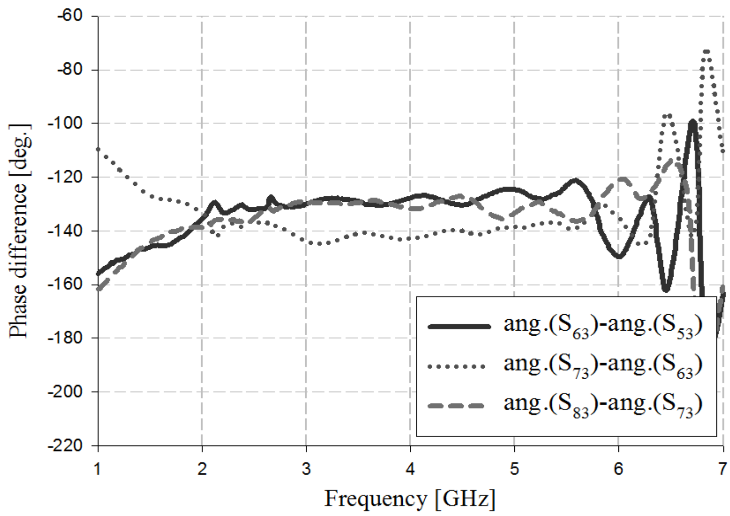

Fig. 4-18. Measurement analysis of phase difference for input port 3

The results in Fig. 4-17 show that in the 3 ㎓ band, the phase is -17° and 112° in S_{53} and S_{63}; 112° and -103° in S_{63} and S_{73}; and -103° and 25° in S_{73} and S_{83}, respectively. In the 4 ㎓ band, the phase is 79° and -152° in S_{53} and S_{63}; -152° and -9° in S_{63} and S_{73}; and -9° and 122° in S_{73} and S_{83}, respectively. In the 5 ㎓ band, that phase is 176° and -59° in S_{53} and S_{63}; -59° and 79° in S_{63} and S_{73}; and 79° and -147° in S_{73} and S_{83}, respectively.

The measurement results in Fig. 4-18 show that the phase difference in the 3 ㎓, 4 ㎓, and 5 ㎓ band are -135° ± 8°, -135° ± 8°, and -135° ± 10°, respectively.

The measurement results of phase and phase difference for input port 4 are shown in Fig. 4-19 and Fig. 4-20.

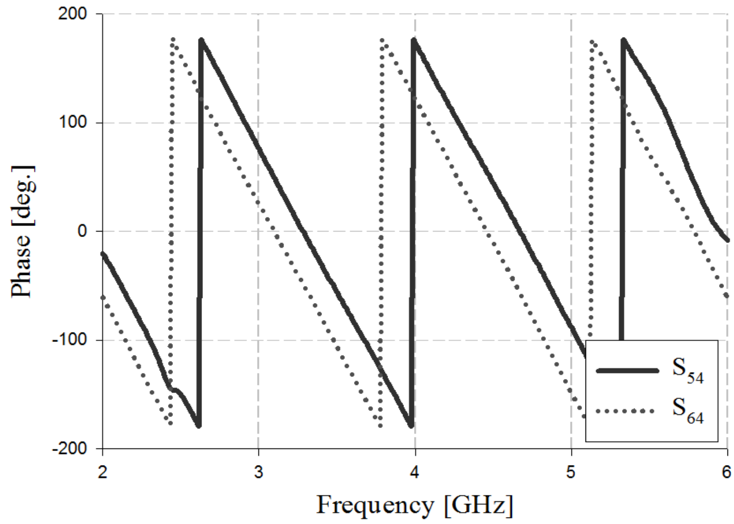

(a)

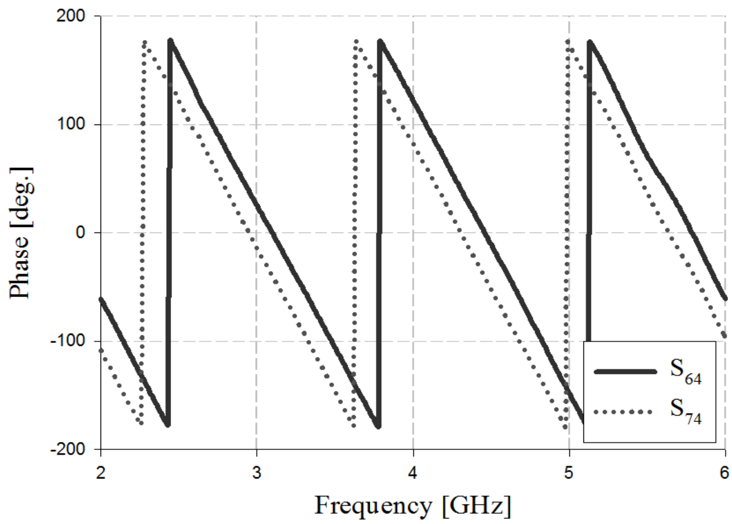

(b)

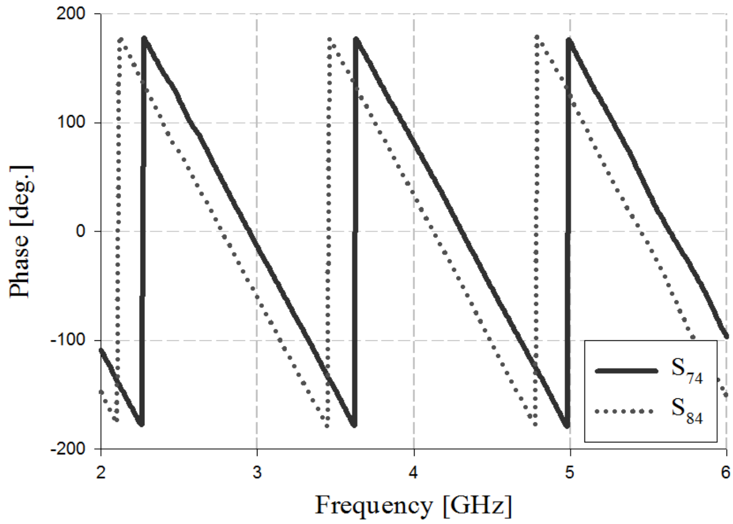

(c)

Fig. 4-19. Measurement analysis of phase for input port 4,

(a) Phase of S_{54} and S_{64}, (b) Phase of S_{64} and S_{74}, (c) Phase of S_{74} and S_{84}

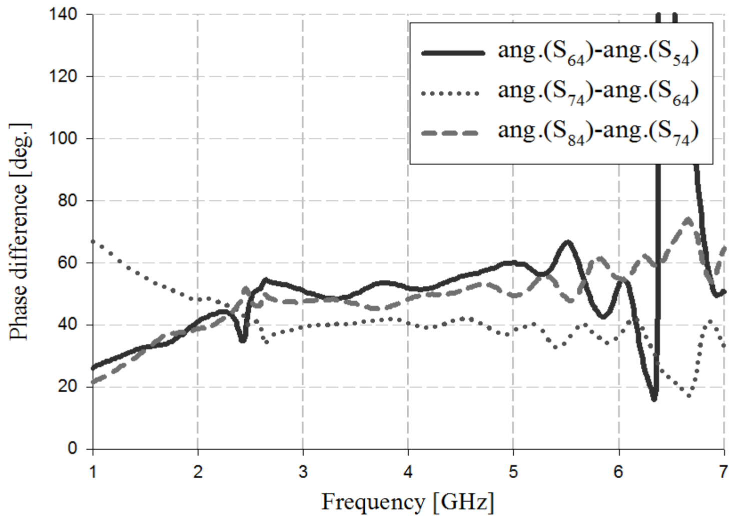

Fig. 4-20. Measurement analysis of phase difference for input port 4

The results in Fig. 4-19 show that in the 3 ㎓ band, the phase is 74° and 23° in S_{54} and S_{64}; 23° and -15° in S_{64} and S_{74}; and -15° and -63° in S_{74} and S_{84}, respectively. In the 4 ㎓ band, the phase is 171° and 119° in S_{54} and S_{64}; 119° and 79° in S_{64} and S_{74}; and 79° and 30° in S_{74} and S_{84}, respectively. In the 5 ㎓ band, that phase is -88° and -148° in S_{54} and S_{64}; -148° and 173° in S_{64} and S_{74}; and 173° and 124° in S_{74} and S_{84}, respectively.

The measurement results in Fig. 4-20 show that the phase difference in the 3 ㎓, 4 ㎓, and 5 ㎓ band are 45° ± 6°, 45° ± 6°, and 45° ± 12°, respectively.

The measurement results for the overall analysis of the proposed 4 × 4 Butler matrix are listed in Table 4-4.

Table 4-4. Overall analysis of the fabricated 4 × 4 Butler matrix

Input port \ Output port		Phase [deg.]				Phase difference [deg.]		
		P_5	P_6	P_7	P_8	S_{51}-S_{61}	S_{61}-S_{71}	S_{71}-S_{81}
Port 1	3 ㎓	-68	-25	20	62	-43	-45	-42
	4 ㎓	23	66	116	155	-43	-50	-39
	5 ㎓	115	157	-156	-113	-42	-47	-43
Port 2	3 ㎓	19	-116	109	-30	135	135	139
	4 ㎓	115	-25	-156	58	140	131	146
	5 ㎓	-153	63	-62	156	144	125	142
Port 3	3 ㎓	-17	112	-103	25	-129	-145	-128
	4 ㎓	79	-152	-9	122	-129	-143	-131
	5 ㎓	176	-59	79	-147	-125	-138	-134
Port 4	3 ㎓	74	23	-15	-63	51	38	48
	4 ㎓	171	119	79	30	52	40	49
	5 ㎓	-88	-148	173	124	60	39	49

The results in Table 4-4 show that input ports 1～4 generate the phase difference at regular intervals in each output port, and the output phase is fed into the array antenna.

4.3 Measurement Configuration of Beamforming Antenna

The structure of the fabricated beamforming antenna is shown in Fig. 4-21.

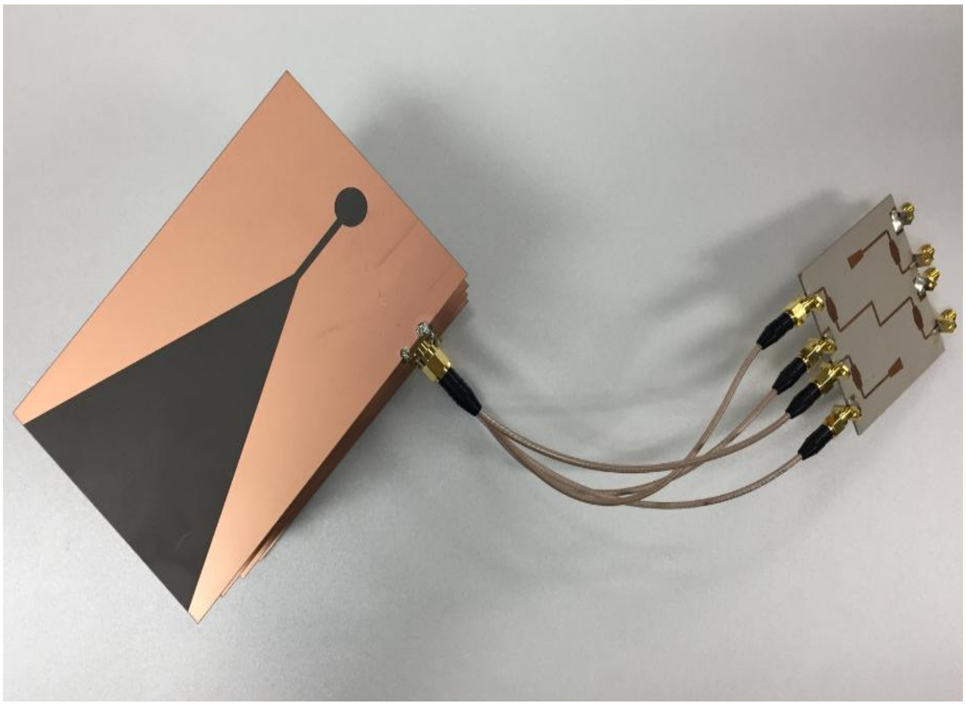

Fig. 4-21. Photograph of the fabricated beamforming antenna

The proposed beamforming antenna was fabricated by connecting the 1 × 4 array antenna and 4 × 4 Butler matrix.

The radiation patterns of the fabricated beamforming antenna were measured using a far-field analysis system in an anechoic chamber room of Korea EMTI Co..

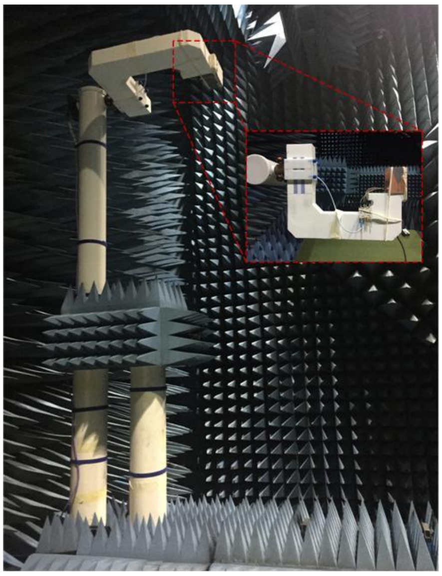

Fig. 4-22. Measurement configuration of the fabricated beamforming antenna

Table 4-5. Equipment configuration and performance

Chamber size	16 × 11 × 9.5 ㎥
Chamber type	Rectangular type
Measurement range	400 ㎒ ~ 60 ㎓
Measurement configuration	Far-field
Measurement parameter	Antenna pattern, Antenna gain
Major equipment	- Network analyzer E8361A - LO/IF distribution unit 85309A (Agilent) - Amplifier 83017A (Agilent) - Amplifier 20T4G18AM2 - Mixer 85320A, 85320B (Agilent)

In order to confirm the beam performance of the fabricated beamforming antenna, it was sequentially fed the feed wave of 3 ㎓, 4 ㎓, and 5 ㎓ into each input port. When the feed wave was fed to each input port, the terminating resistance was connected the remaining ports. The results of the radiation pattern analysis of the fabricated beamforming antenna are shown in Fig. 4-23, Fig. 4-24.

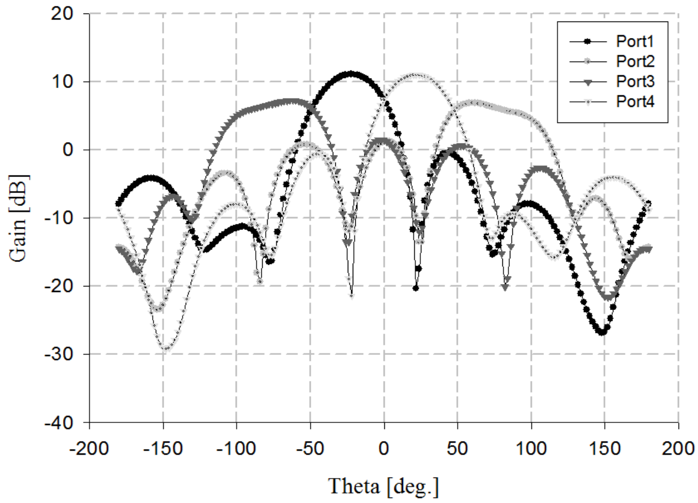

(a)

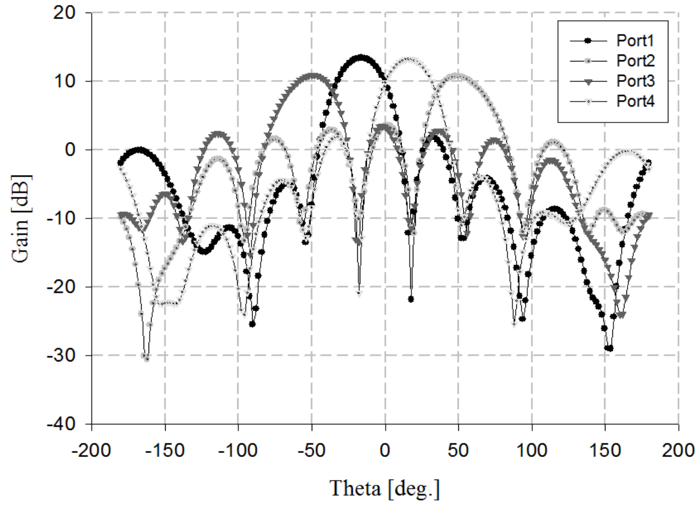

(b)

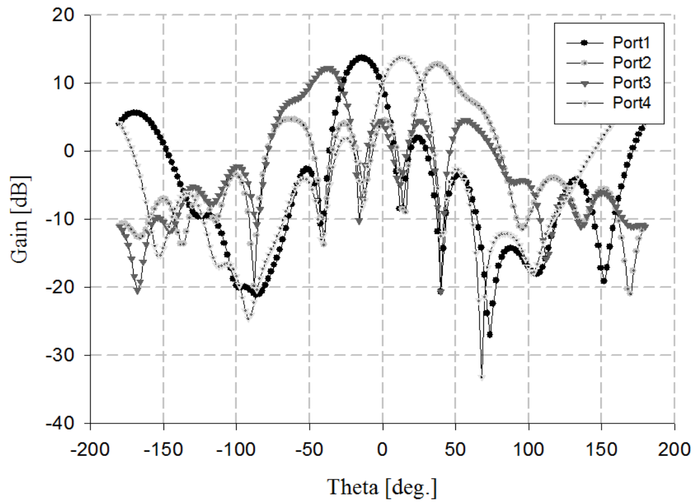

(c)

Fig. 4-23. Simulation results of the fabricated phased array antenna at each frequency, (a) 3 ㎓, (b) 4 ㎓, (c) 5 ㎓

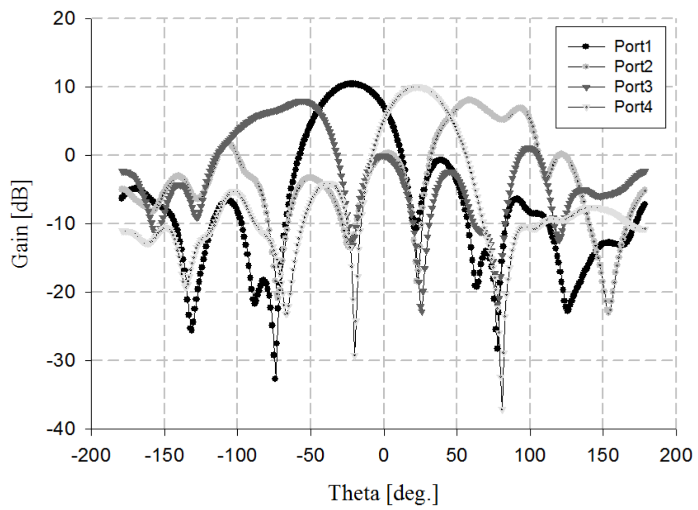

(a)

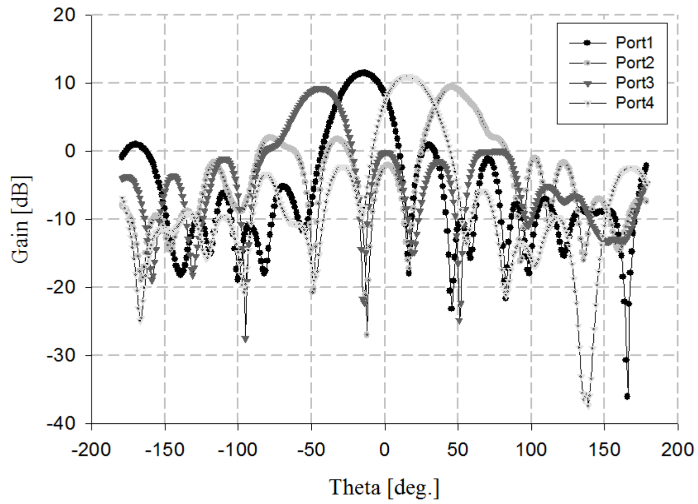

(b)

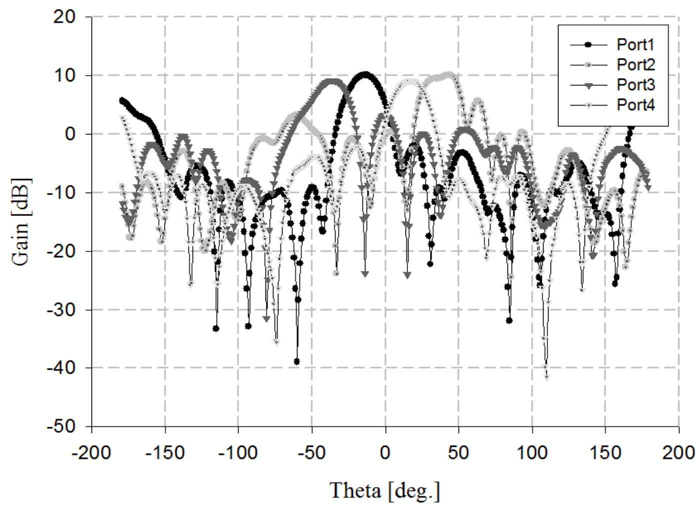

(c)

Fig. 4-24. Measured results of the fabricated phased array antenna at each frequency, (a) 3 ㎓, (b) 4 ㎓, (c) 5 ㎓

The results in Fig. 4-23, Fig. 4-24 show that the simulated and measured beamforming angles in the 3 ㎓ band are −22°, +60°, −62°, +22°; and −21°, +59°, −56°, and +23°, respectively. In the 4 ㎓ band, the simulation and measurement results are −16°, +45°, −50°, +16°; and −14°, +46°, -44°, +16°, respectively. In the 5 ㎓ band, the simulation and measurement results are −14°, +38°, −38°, +14°; and −13°, +44°, −36°, +17°, respectively.

Therefore, the maximum beamforming range of the fabricated antenna are 115° (+59° to −56°) in the 3 ㎓ band, 90° (+46° to −44°) in the 4 ㎓ band, and 80° (+44 to −36°) in the 5 ㎓ band.

The proposed antenna is compared to conventional antennas with wide bandwidth in Table 4-6.

Table 4-6. Comparison of the proposed antenna and conventional antennas

Antenna	**Reference [60]**		**Reference [61]**		**Reference [62]**		**Proposed single antenna**		**Proposed beamforming antenna**	
Antenna type	LTSA		Vivaldi		Vivaldi		LTSA		Phased array	
3 dB beamwidth	6 ㎓	38°	2.5 ㎓	72°	1 ㎓	76°	3 ㎓	72°	-	-
	7 ㎓	40°	6 ㎓	35°	2 ㎓	50°	4 ㎓	40°	-	-
	-	-	10 ㎓	21°	3 ㎓	35°	5 ㎓	29°	-	-
Beamforming range	-	-	-	-	-	-	-	-	3 ㎓	115°
	-	-	-	-	-	-	-	-	4 ㎓	90°
	-	-	-	-	-	-	-	-	5 ㎓	80°

As shown in Table 4-6, the proposed single antenna has a similar 3 dB beamwidth such as conventional antennas. However, by fabricating with a beamforming antenna, it becomes wider in detection range.

4.4 Object Tracking Test of Fabricated Beamforming Antenna

This chapter describes the simple experiment to verify the practicability of fabricated antenna. The configuration of proposed radar system is shown in Fig. 4-25.

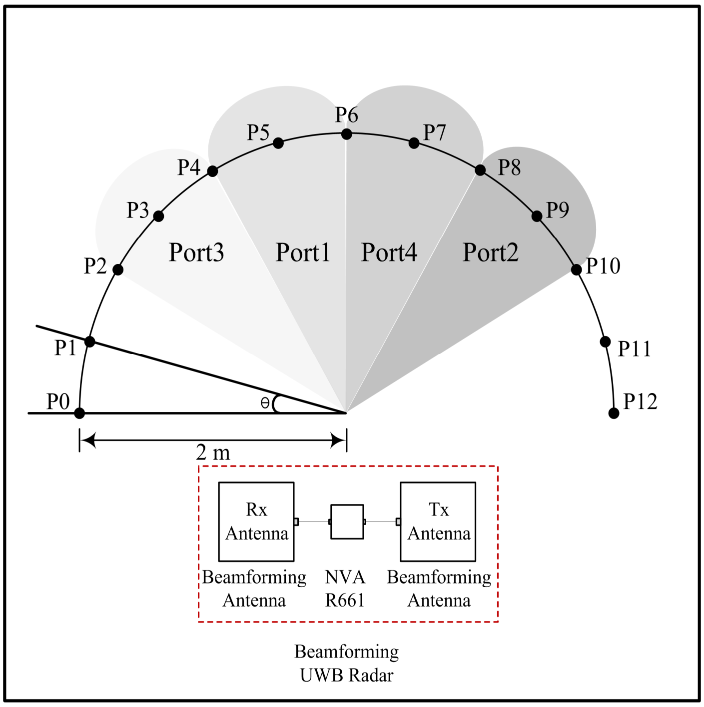

Fig. 4-25. Configuration of the proposed system

As shown in Fig. 4-25, the proposed radar system is consisted by connecting the fabricated beamforming antenna and NVA-R661 UWB radar module (Xethru co.). The proposed radar system has four measurement regions according to four input ports, and the angle Θ between each point is 15°.

4.4.1 Configuration of Object Tracking

The signal processing procedure of the proposed radar system is shown in Fig. 4-26.

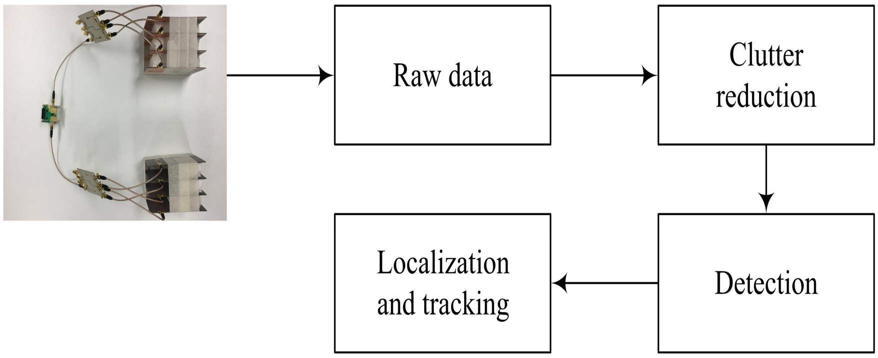

Fig. 4-26. Signal processing procedure of the proposed radar system

As shown in Fig. 4-26, the processing procedure of the proposed system consist of clutter reduction, detection, localization and tracking steps. In the clutter reduction step, the primary goal is to remove clutter in the raw data captured by the UWB radar. Because clutter, which is, unwanted signals reflected from static objects in indoor positioning applications, is present, so the received signal (which includes clutter) should be carefully handled[63]. This thesis applied the clutter reduction method using singular value decomposition (SVD)[64]. In the detection step, the location of object is determined. In localization and tracking step, the distance to the target is determined by using the TOA (Time-of-Arrival) of the detected target signal[65].

The experiment environment of the proposed radar system is shown in Fig. 4-27.

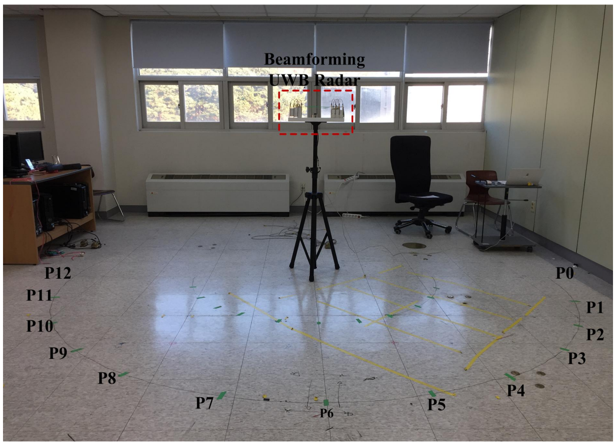

(a)

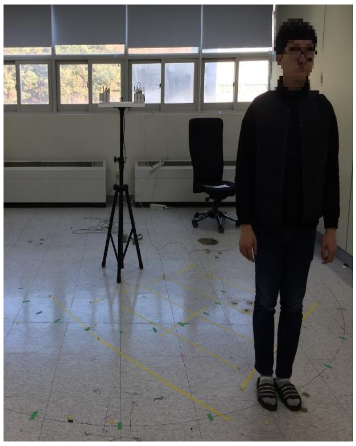

(b)

Fig. 4-27. Experiment environment of the proposed radar system, (a) Experiment environment #1, (b) Experiment environment #2

As shown in Fig. 4-27, the distance between the radar and a target is 2 m, a target was measured in a staked sequential order of P0 to P12.

4.4.2 Object Tracking Measurement

In order to verify the performance of the proposed beamforming antenna, it is compared by measuring the proposed antenna and commercial UWB antenna. The antenna and module of the commercial products are shown in Fig. 4-28[66][67].

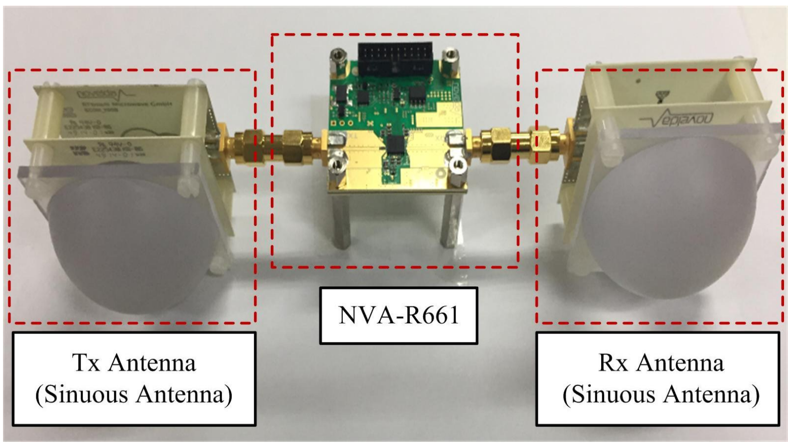

Fig. 4-28. Configuration of commercial UWB radar module[66][67]

Single target analysis using commercial UWB antenna is shown in Fig. 4-29.

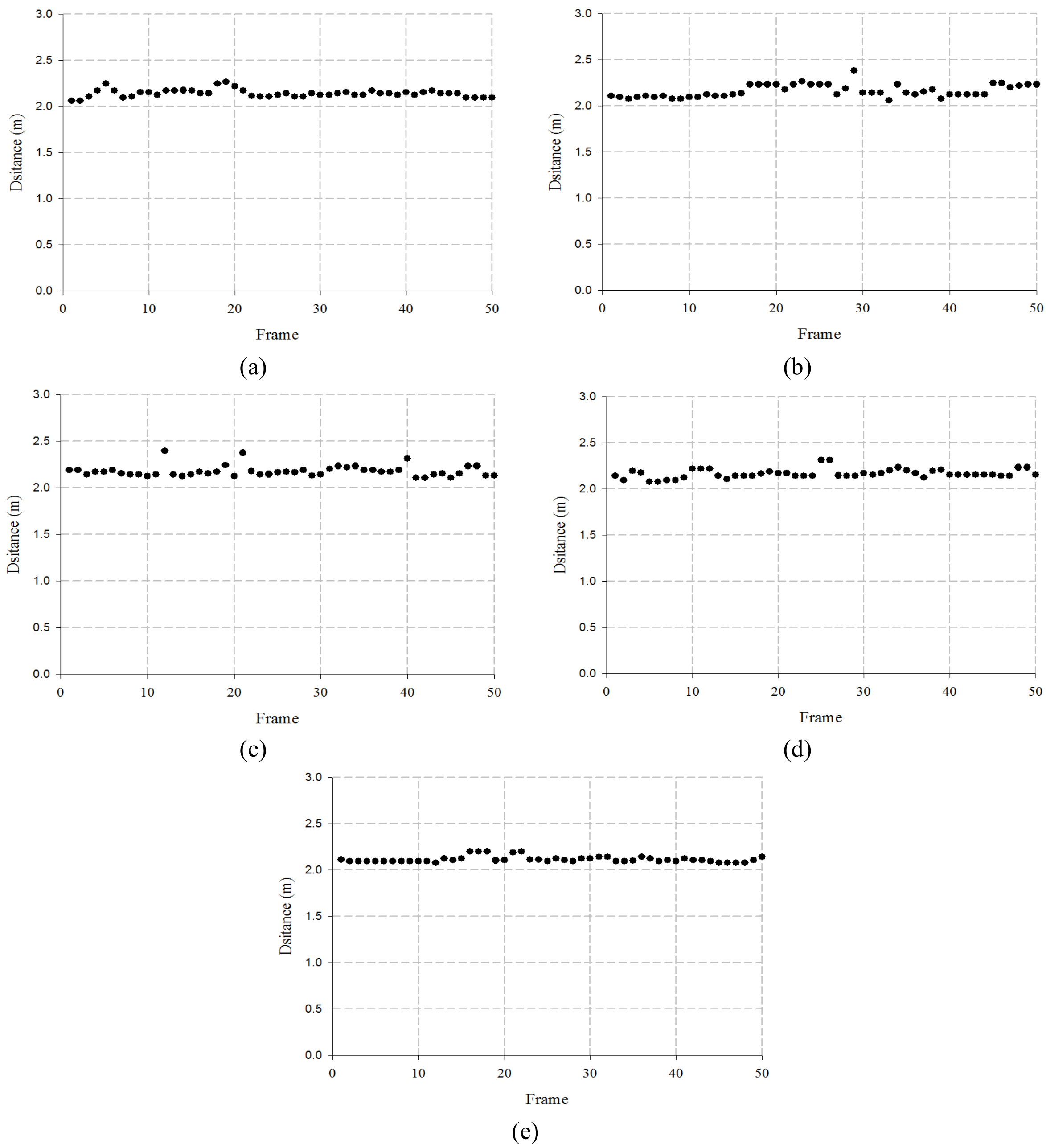

Fig. 4-29. Measured results of single target using commercial UWB antenna, (a) P4, (b) P5, (c) P6, (d) P7, (e) P8

The results in Fig. 4-29 shows that a target is detected at 2 m in the region of P4, P5, P6, P7, and P8.

Single target analysis using proposed beamforming antenna is shown in Fig. 4-30.

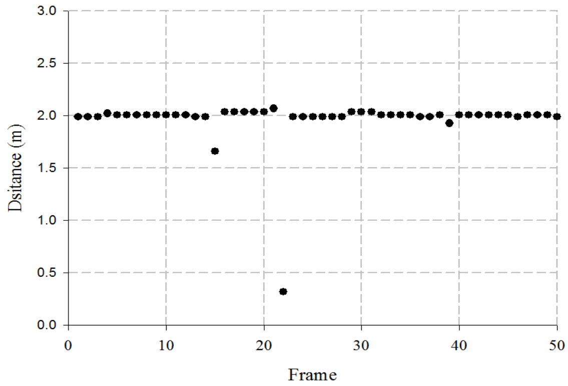
Dsitance (m)
Frame

(a)

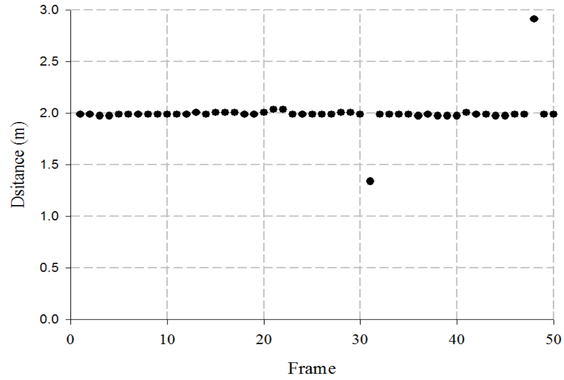
Dsitance (m)
Frame

(b)

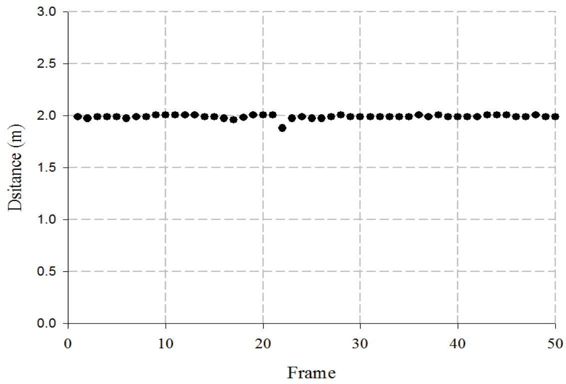
Dsitance (m)
Frame

(c)

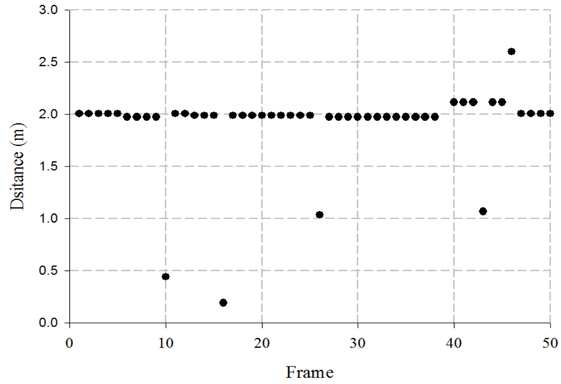
Dsitance (m)
Frame

(d)

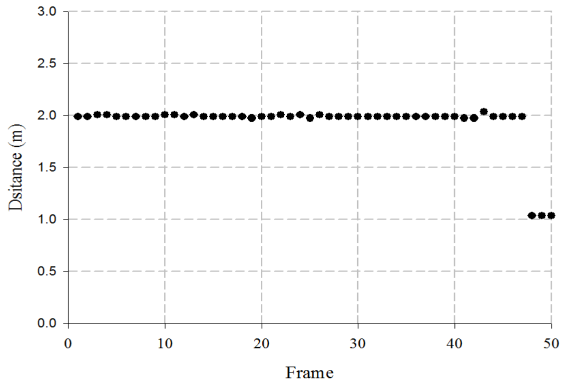
Dsitance (m)
Frame

(e)

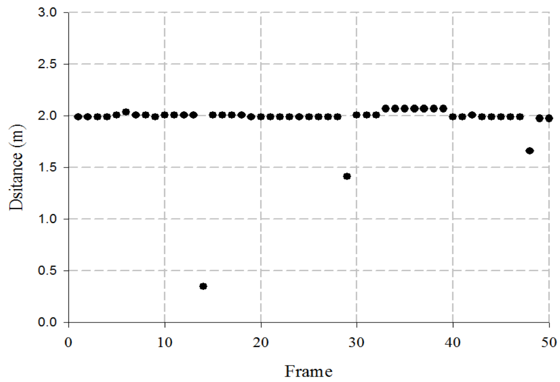
Dsitance (m)
Frame

(f)

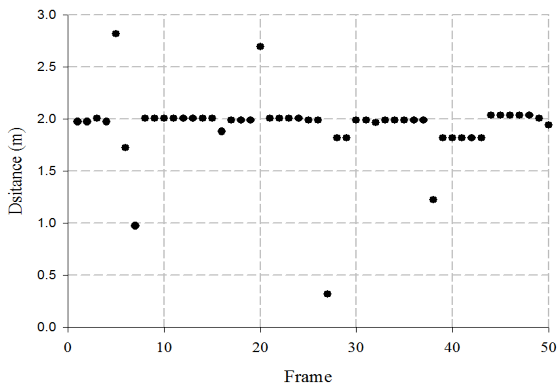
Dsitance (m)
Frame

(g)

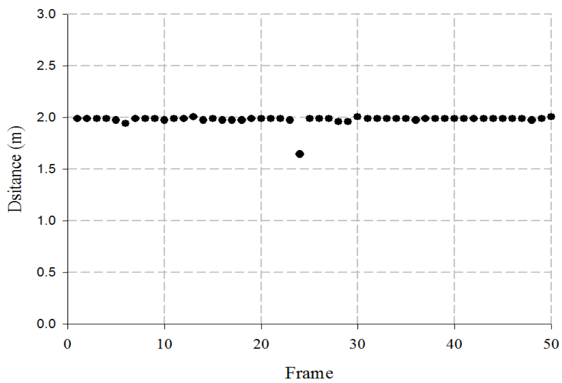
Dsitance (m)
Frame

(h)

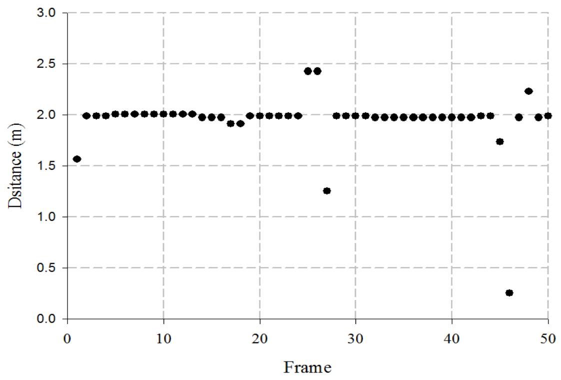

(i)

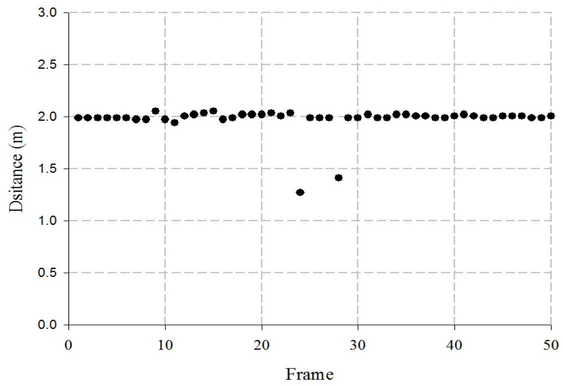

(j)

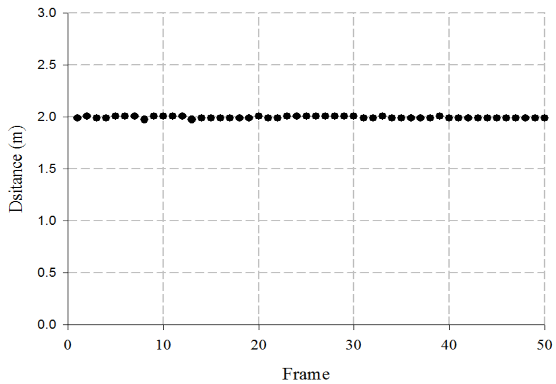

(k)

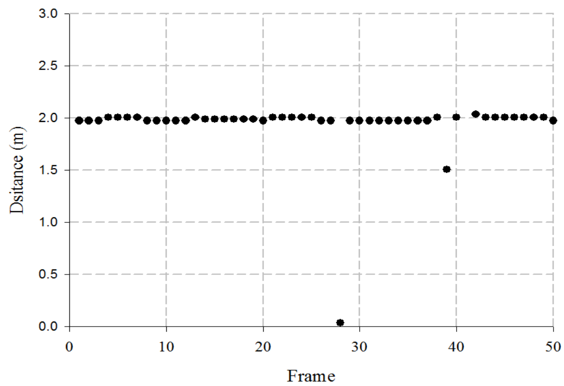

(l)

Fig. 4-30. Measured results of single target using proposed beamforming antenna, (a) P2, (b) P3, (c) P4, (d) P4, (e) P5, (f) P6, (g) P6, (h) P7, (i) P8, (j) P8, (k) P9, (l) P10

The results in Fig. 4-29 shows that in port 3, target is detected at 2 m in the regions of P2, P3 and P4. In port 1, target is detected at 2 m in the regions of P4, P5 and P6. In port 4, target is detected at 2 m in the regions of P6, P7 and P8. In port 2, target is detected at 2 m in the regions of P8, P9 and P10.

Hence, the proposed beamforming antenna has a wide range of approximately 60° which compared with the commercial UWB antenna.

V Conclusion

Thesis gives the overview of a beamforming antenna that can track the location of objects over a wide range. Conventional UWB antennas have difficultly tracking objects over a wide range because of the relatively narrow beamwidth. In order to solve this problem, it proposed a beamforming antenna to track objects over a wide range by electronically controlling the beam of the antenna.

The Butler matrix for forming multibeams has N input and N output ports where the value of N are 4, 8, and 16. However, the increase of N result in the increase of beam direction, which is a complicated design with larger circuit pattern. The fabrication of 4 × 4 Butler matrix, which has four input and four output ports is studied.

The fabricated matrix consists of the four 3 dB/90° slot-directional hybrid couplers and the two 45° phase shifters, and the overall size is 70.65 × 62.6 × 1.22 ㎣. The frequency band has a wide bandwidth of approximately 2 ㎓ in 3 ~ 5 ㎓. The insertion loss within the proposed bandwidth was approximately 6 ~ 8 dB, while the return loss and isolation characteristics were less than -13 dB. Furthermore, the phase measurement results between output ports within proposed band were approximately ± 10° in -45°, 135°, -135°, 45°.

The beamforming antenna was fabricated by connecting the 4 × 4 Butler matrix and 1 × 4 array antenna. The feed generated in the 4 × 4 Butler matrix was fed into the 1 × 4 array antenna, which controlled the four beams. The overall size of the fabricated TSA is 140 × 90 × 1.52 ㎣, and the impedance bandwidth has a wide bandwidth of 4.32 ㎓ in 1.46 – 5.78 ㎓. The fabricated beamforming antenna has beamforming angles of –21°, +59°, –56°, and +23° in the 3 ㎓ band; –14°, +46°, -44°, and +16° in the 4 ㎓ band; and –13°, +44°, –36°, and +17° in the 5 ㎓ band.

The beamforming angles of the fabricated beamforming antenna have maximum values of 115°, 90°, and 80° in the 3 ㎓, 4 ㎓, and 5 ㎓ band, respectively. The results of object tracking shows that a target is detected at 2 m in the regions in P2 to P10. Hence, the proposed beamforming antenna provide a solution to enable the tracking of objects over a wide range compared with conventional UWB antennas.

References

[1] 이종훈, 김상동, 정우영, 김선미, 박용완, “실시간 실내외 측위 기술 개발 동향 분석,” 대한전자공학회텔레콤, Vol. 22, No. 02, pp. 85~95, 2006. 12.

[2] D. Y. Yoon, “A design of the impulse radar digital signal processing for the precise location positioning in IR-UWB,” M.S. thesis, Hanyang Univ., pp. 01~02, Feb. 2012.

[3] I. J. Immoreev, “Ultra-wideband systems features and ways of development,” 2004 Second International Workshop, Ultrawideband and Ultrashort Impulse Signals, pp. 19~22, Sept. 2004.

[4] Federal Communications Commission, ‘FCC Part15-radio frequency devices, code federal regulation 47 CFR Ch. 1 (10-1-09 Edition),” Section 15.521, Washington, D.C., 2009.

[5] M. Welborn, and J. McCorkle, ‘The importance of fractional bandwidth in ultra wideband pulse design,” Proc. IEEE Int. Conf. Commun., Vol. 02, pp. 753~757, Apr. 2002.

[6] D. Cassioli, M. Z. Win, and A. F. Molisch, ‘The ultra-wide bandwidth indoor channel: From statistical model to simulations,” *IEEE J. Sel. Areas Commun.*, Vol. 20, pp. 1247~1257, Aug. 2002.

[7] K. Y. Kim, “Design of UWB Beam Scanning Antenna Systems based on Time Domain Analysis,” Ph. D. thesis, Kwangwoon Univ., pp. 01~02, Feb. 2014.

[8] Zedong Wang, Yingzeng Yin, Jianjun Wu, and Ruina Lian, “A Miniaturized CPW-Fed Antipodal Vivaldi Antenna With Enhanced Radiation Performance for Wideband Applications,” *IEEE Antennas AND Wireless Propagation Letters*, Vol. 15, pp. 16~19, Feb. 2016.

[9] Zhou Yang, Huang Jingjian, Wu weiwei, and Yuan Naichang, “An antipodal

Vivaldi antenna with band-notched characteristics for ultra-wideband applications," *Int. J. Electron. Commun.*, Vol. 76. pp. 152-157, Jun. 2017.

[10] Muhammad Saqib Rabbani, and Hooshang Ghafouri-Shiraz "Accurate remote vital sign monitoring with 10 GHz ultra-wide patch antenna array," *Int. J. Electron. Commun.*, Vol. 77. pp. 36~42, Jul. 2017.

[11] Jiangniu Wu, Zhiqin Zhao, Zaiping Nie, and Qing-Huo Liu, "Bandwidth Enhancement of a Planar Printed Quasi-Yagi Antenna With Size Reduction," *IEEE Transactions on Antennas and Propagation*, Vol. 62, Iss. 01, pp. 463~467, Jan. 2014.

[12] Deqiang Yang, Jiafeng Qu, Zhiqin Zhao, Sihao Liu, and Zaiping Nie, "Planar quasi-Yagi antenna with band rejection based on dual dipole structure for UWB," *IET Microwaves, Antennas & Propagation*, Vol. 10, Iss. 15, pp. 1708~1714, Dec. 2016.

[13] F. Zhu, S. Gao, A.T.S. Ho, C.H. See, R.A. Abd-Alhameed, J. Li, and J. Xu, "Dual band-notched tapered slot antenna using λ/4 band-stop filters," *IET Microwaves, Antennas & Propagation*, Vol. 06, Iss. 15, pp. 1665~1673, Dec. 2012.

[14] Sahar Chagharvand, Mohamad R. Hamid, Muhammad R. Kamarudin, and Farid Ghanem, "Reconfigurable Multiband Tapered Slot Antenna," Microwave and Optical Technology Letters, Vol. 57, No. 09, pp. 2182~2186, Sep. 2015.

[15] Krzysztof Wincza, Kamil Staszek, Izabela Slomian, and Slawomir Gruszczynski, "Scalable Multibeam Antenna Arrays Fed by Dual-Band Modified Butler Matrices," *IEEE Transactions on Antennas and Propagation*, Vol. 64, No. 04, pp. 1287~1297. Apr. 2016.

[16] J. Blass, "Multidirectional antenna - A new approach to stacked beams,"

IRE International Convention Record, pp. 48~50, Mar. 1966.

[17] Tarek Djerafi, Nelson J. G. Fonseca, and Ke Wu, "Planar Ku-Band 4 × 4 Nolen Matrix in SIW Technology," *IEEE Transactions on Microwave Theory and Techniques*, Vol. 58. No. 02, pp. 259~266, Feb. 2010.

[18] I. R. Kim, C. H. Ahn, and S. S. Oh, "Design and Implementation of Beam Steering System Based on Rotman lens and its Real-Time Display Device of Beam Receiving," *Journal of the Institute of Electronics and Information Engineers*, Vol. 53, No. 04, pp. 37~46, May 2016.

[19] 이홍민, 이동통신용 안테나 설계 실무, 상학당, pp. 109~110, 2010.

[20] D. Y. Yoon, "A design of the impulse radar digital signal processing for the precise location positioning in IR-UWB," M.S. thesis, Hanyang Univ., pp. 9 ~10, Feb. 2012.

[21] N. Paulino, A. S. Garcao, and J. Goes, Low Power UWB CMOS Radar Sensors, First Edition, Springer, 2008.

[22] E. C. Lee, "A Research on Performance Enhancement of Multi-human Detection Algorithm Using IR-UWB Radar Sensor," M.S. thesis, Hanyang Univ., pp. 09~10, Feb. 2017.

[23] C. T. P. Song, P. S. Hall, H. Ghafouri, and I. Henning, "Fractal Antenna Research at University of Birmingham," 11th Int, Conf. on Antennas and Propagation, pp. 724~727, Apr. 2001.

[24] J. P. Gianvittorio, and Y. Rahmat-Samii, "Fractal Antennas; A Novel Antenna Miniaturization Technique, and Applications," IEEE Antennas and Propag. Mag., Vol. 44, Iss. 01, pp. 20~36, Feb. 2002.

[25] Kurt L. Shlager, Glenn S. Smith, and James G. Maloney, "Optimization of Bow-Tie Antennas for Pulse Radiation," *IEEE Trans. Antennas Propag.*, Vol. 42, No. 07, pp. 975~982, Jul. 1994.

[26] Alberto Reyna, Marco A. Panduro, Aldo L. Mendez, and Gerardo Romero, “Timed arrays of spiral antennas for circularly polarised UWB scanned patterns with low side lobes,” *IET Microwaves, Antennas & Propagation*, Vol. 10, Iss. 04, pp. 587~593, Apr. 2016.

[27] Homayoon Oraizi, Amrollah Amini, and Mehdi Karimi Mehr, “Design of miniaturised UWB log-periodic Design of miniaturised UWB log-periodic WLAN band-rejection,” *IET Microwaves, Antennas & Propagation*, Vol. 11, Iss. 02, pp. 193~202, Feb. 2017.

[28] Amrollah Amini, Homayoon Oraizi, Mohammad Amin Chaychi zadeh, “Miniaturized UWB Log-Periodic Square Fractal Antenna,” *IEEE Antennas and Wireless Propagation Letters*, Vol. 24, pp. 1322~1325, Mar. 2015.

[29] Y. Mushiake, “Self-Complementary Antennas,” *IEEE Antennas and Propag. Mag.*, Vol. 34, No. 06, pp. 23~29, Dec. 1992.

[30] Jin Au Kong, Yan Zhang, Robert T. Shin, Fernando L. Teixerira, and Y. Eric Yang, Wideband Antenna Element in Electromagnetic Wave Theory and Applications, RLE Progress Report 143.

[31] 김종규, 허유강, 조영기, “UWB 안테나 기술동향,” 전자파기술, Vol. 13, No. 03, pp. 24~32, 2002. 07.

[32] Compliance Engineering “Log Periodic Antenna”, http://www.compeng.com.au/document-library/ce1000e-log-periodic-antenna/,(2017.10.10.)

[33] J. J. Park, “ Design and fabrication of a high conversion efficiency 2.45㎓ rectenna using fractal geometry,” Ph. D. thesis, Chosun Univ., pp. 48~49, Feb. 2013.

[34] UMAIN “Bow-tie Antenna”, http://www.umain.co.kr/uwb-directional-antenna/, (2017.10.10.)

[35] Indiamart “Horn Antenna”, https://dir.indiamart.com/impcat/horn-antenna.htm

l, (2017.10.11.)

[36] Toptech microwave “Horn antenna”, http://www.toptech-mw.com/index.html, (2017.10.11.)

[37] Boris Lembrikov, Ultra Wideband, INTECH, pp. 374~377, 2010.

[38] K. S. Yngvesson, D. H. Schaubert, T. L. Korzeniowski, E. L. Kollberg, T. Thungren, and J. F. Johansson, “Endfire tapered slot antennas on dielectric substrates,” *IEEE Trans. Antenna Propagation*, Vol. AP-33, No. 12, pp. 1392~1400, Dec. 1985

[39] J. M. Kim, “Time-domain design of IR-UWB antenna for optimum impulse radio radiation,” Ph. D. thesis, Kwangwoon Univ., pp. 40~43, Feb. 2013.

[40] S. W. Kim, and D. Y. Choi, “Implementation of Rectangular Slit-Inserted Ultra-Wideband Tapered Slot Antenna,” *SpringerPlus*, Vol. 2016, pp.1~11, Aug. 2016.

[41] Chang K, RF and Microwave Wireless Systems, Wiley, New York, pp. 74~77, 2000.

[42] J. A. Navarro and K. Chang, Integrated Active Antennas and Spatial Power Combining, John Wiley & Sons, New York, 1996.

[43] D. H. Lee, “Implementation of broadband 4×4 butler beamforming network based on multilayer microstrip technology,” M.S. thesis, Jeju Univ., pp. 04~21, Feb. 2017.

[44] Chang K, RF and Microwave Wireless Systems, Wiley, New York, pp. 98~100, 2000.

[45] S. C. Park, S. H. Kim, J. H. Sohn, and H. C. Shin, “Design of a 28 GHz Switched Beamforming Antenna System Based on 4×4 Butler Matrix,” *JKIEES*, Vol. 26, No. 10, pp. 876~884, Sep. 2015.

[46] S. C. Park, “Design of a 28GHz Switched Beamforming Antenna System

Based on Butler Matrix," M.S. thesis, Kwangwoon Univ., pp. 343~346, Feb. 2016.

[47] Chang K, RF and Microwave Wireless Systems, Wiley, New York, pp. 114~118, 2000.

[48] David M. Pozar, Microwave Engineering, John Wiley & Sons, pp. 343~347, 2012.

[49] T. Tanaka, K. Tsunoda, and M. Aikawa "New slot-coupled directional couplers between doublesided substrate microstrip lines, and their applications," IEEE MTT-S International, Microwave Symposium Digest, pp. 579~582, May 1988.

[50] W. Hilberg, "From approximations to exact relations for characteristic impedances," *IEEE Transactions on Microwave Theory and Techniques*, Vol. 17, Iss. 05, pp. 259~265, May 1969.

[51] Osama Mohamed Haraz, Abdel-Razik Sebak, and Saleh A. Alshebeili, "Ultra-Wideband 4 × 4 Butler Matrix Employing Trapezoidal-Shaped Microstrip-Slot Technique," *Wireless Personal Communications*, Vol. 82, Iss. 02, pp. 709~721, May 2015.

[52] David M. Pozar, Microwave Engineering, John Wiley & Sons, pp. 147~149, 2012.

[53] S. W. Kim, and D. Y. Choi, "Design of Tapered Slot Antenna for UWB Communications," *KISM Smart Media Journal*, Vol. 04, No. 04, pp. 64~69, Dec. 2015.

[54] S. W. Kim, G. S. Kim, S. K. Noh, D. Y. Choi, "Design and Implementation of an IR-Ultra Wide Band Tapered Slot Antenna with a Rectangular Slot Structure," International Conference on Green and Human Information Technology 2015, pp. 321~324, 2015.

[55] S. W. Kim, D. Y. Choi, "Analysis of Tapered Slot Antenna for UWB with Directivity Characteristic," *JKIICE*, Vol. 20, No. 04, pp. 691~697, Apr. 2016.

[56] D. H. Lee, "Tapered Slot Antennas with Band-Notched Characteristics for UWB Applications," Ph. D. thesis, Kyungpook Univ., Aug. pp. 35~37, 2013.

[57] K. Y. Kim, "Design of UWB Beam Scanning Antenna Systems based on Time Domain Analysis," Ph. D. thesis, Kwangwoon Univ., pp. 25~28, Feb. 2014.

[58] H. C. Kim, J. W. Jing, H. J. Lee, and Y. S. Lim, "Design of Circularly Polarization Patch Array Antenna for DSRC," JKIEES, Vol. 23, No. 02, pp. 144~150, Feb. 2012.

[59] H. C. Kim, "Circularly Polarized Patch Array Antenna Design for DSRC Road-side Equipment of ITS," M.S. thesis, Chonnam Univ., Aug. 2011.

[60] D. M. In, M. J. Lee. D. H. Kim, C. Y. Ohm and Y. S. Kim, "Antipodal Linearly Tapered Slot Antenna using Unequal Half-Circular Defected Sides for Gain Improvements," *Microwave and Optical Technology Letters*, Vol. 54, No. 08, pp. 1963~1965, Aug. 2012.

[61] Ya-Wei Wang, Guang-Ming Wang, and Bin-Feng Zong, "Directivity Improvement of Vivaldi Antenna Using Double-Slot Structure," *IEEE Antennas AND Wireless Propagation Letters*, Vol. 12, pp. 1380~1383, Oct. 2013.

[62] JSC "Vivaldi Antenna," http://uwbs.ru/, (2017.11.28.)

[63] N. V. Han, D. M. Kim, G. R. Kwon, and J. Y. Pyun, "Clutter reduction on impulse radio ultra wideband radar signal," in Proceedings of the International Technical Conference on Circuits/Systems, Computers and Communications (ITC-CSCC '13), no. 01, Sapporo, Japan, pp. 1091~1094, June 2013.

[64] I. S. Baek, J. H. Kim, and S. H. Cho, “Clutter signal subtraction algorithm for detecting target in IR-UWB Radar system,” Proceedings of Symposium of the Korean Institute of communications and Information Sciences, pp. 338∼339, Feb. 2012.

[65] B. H. Kim, S. J. Han, G. R. Kwon, and J. Y. Pyun, “Signal Processing for Tracking of Moving Object in Multi-Impulse Radar Network System,” International Journal of Distributed Sensor Networks, Vol. 2015, pp. 01∼12, Oct. 2015.

[66] LAONURI “IR-UWB module,” http://www.laonuri.com/, (2017.12.30.)

[67] XETHRU “IR-UWB module,” https://www.xethru.com/, (2017.12.30.)

List of Publications

International Journals

[1] S. W. Kim, G. S. Kim, and D. Y. Choi, "CPW-Fed Wideband Circular Polarized Antenna for UHF RFID Applications," *International Journal of Antenna and Propagation*, Vol. 2017, pp. 1~7, Jul. 2017.

[2] S. W. Kim, and D. Y. Choi, "Compact filtering monopole patch antenna with dual band rejection," *SpringerPlus*, Vol. 2016, pp. 1~12, Jun. 2016.

[3] S. W. Kim, and D. Y. Choi, "Implementation of rectangular slit inserted ultra wideband tapered slot antenna," *SpringerPlus*, Vol. 2016, pp. 1~11, Aug. 2016.

[4] S. Shrestha, J. J. Lee, S. W. Kim, and D. Y. Choi, "Rain Attenuation over Terrestrial Microwave Links at 18 ㎓ as Compared with Prediction by ITU-R Model," *J. Inf. Commun. Converg. Eng.*, Vol. 15, No. 03, pp. 143~150, Sep. 2017.

Domestic Journals

[1] 김선웅, 최동유, "지향성 특성을 갖는 UWB 용 테이퍼드 슬롯 안테나 분석," 한국정보통신학회논문지, Vol. 20, No. 04, pp. 691~697, 2016. 04.

[2] 김선웅, 최동유, "UWB 통신을 위한 테이퍼드 슬롯 안테나 설계," 스마트미디어 저널, Vol. 04, No. 04, pp. 64~69, 2015. 12.

[3] 김진주, 김선웅, 박정진, 정민아, 박경우, 최동유, "마이크로스트립 라인을 이용한 UWB 원형 패치 안테나 설계 및 분석," 한국통신학회논문지, Vol. 40, No. 05, pp. 938~943, 2015. 05.

[4] 김선웅, 박정진, 최동유, "MIMO 구조의 마이크로스트립 패치 안테나 분석," 한국통신학회논문지, Vol. 40, No. 05, pp. 944~949, 2015. 05.

[5] 최동유, 김선웅, 박정진, 정민아, 이성로, "선박 실내 위치 인식을 위한 테이퍼드

슬롯 안테나 설계 및 구현," 한국통신학회논문지, Vol. 39C, No. 12, pp. 1307~1313, 2014. 12.

[6] 김선웅, 김걸범, 윤중현, 최동유, "소형화 구조를 위한 koch curve 마이크로스트립 패치 안테나 설계," 한국정보통신학회논문지, Vol. 18, No. 12, pp. 2823~2830, 2014. 12.

[7] 김선웅, 최동유, "2×2 배열 패치 안테나 구조를 갖는 렉테나 설계 및 구현," 한국IT서비스학회지, Vol. 13, No. 01, pp. 135~146, 2014. 03.